RICE UNIVERSITY

Synthesis mechanism, phase transfer and optical tracking of iron oxide nanoparticles

By

Arjun Prakash

A THESIS SUBMITTED
IN PARTIAL FULFILLMENT OF THE
REQUIREMENTS FOR THE DEGREE

Doctor of Philosophy

APPROVED, THESIS COMMITTEE:

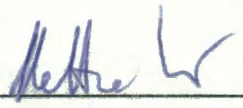

Matteo Pasquali, Professor
Chemical & Biomolecular Engineering, Chemistry

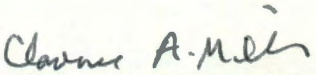

Clarence A. Miller,
Louis Calder Professor Emertius
Chemical & Biomolecular Engineering, Chair

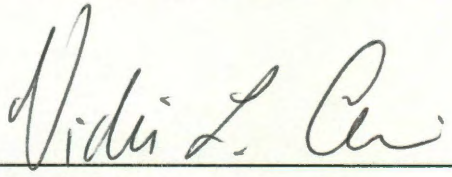

Vicki L. Colvin,
Kenneth S.Pitzer Schlumberger Professor,
Chemistry, Chemical & Biomolecular Engineering
Director, Center for Biological & Environmental Nanotechnology, Thesis Director

HOUSTON, TEXAS
DECEMBER 2010

ACKNOWLEDGEMENTS

This thesis is dedicated to my mother.

I owe a great deal of my journey as a graduate student to my advisor, Dr.Vicki L. Colvin for being the backbone of my research during my time here at Rice. Her inspiration coupled with encouragement and freedom to develop new ideas gave me a unique opportunity to explore the beauty of doing science. She is someone I will always look up to as a symbol of academic excellence.

I thank Dr.Matteo Pasquali for his kindness and guidance. He helped me discover the field of optical microscopy which has become one of my passions. His strong personality and scientific acumen is something I will always try to emulate. I learnt a lot owing to the collaboration with his lab.

I am grateful to Dr.Clarence A. Miller for his constant support throughout the various discussions we had on different topics in interfacial phenomena and surfactants. His guidance served as a basis for one of my projects on phase transfer of nanoparticles.

My deepest gratitude and thanks go to my group members. Dr.Huiguang Zhu deserves my special thanks for all the advice and guidance he has given me over years. Also I owe a lot to Dr.William Yu for his focused guidance, especially during the last few crucial months and for being instrumental in shaping the synthesis mechanism project. Dr. Cafer Yavuz, J.T. Mayo, Christopher Jones, Denise Benoit and Seung Soo Lee have provided invaluable support in all my endeavors. Of special mention is Dr.Michail

Stamatakis for being an inspiring friend and collaborator. I learnt a great deal from him about stochasticity that helped me to build the platform for my microscopy project. I am honored to have worked with and have the support of Dr. John Fortner, Zuzanna Lewicka, Dr. Carolina Avendano, Hema Puppala, Erika Bryant, Elizabeth Quevedo, Adina Boyd, Dr. Joshua Faulkner, Minjung Cho, Aniway Lomeda and Teresa Champion. Alexei Tcherniak and Nikta Fakhri are the other two collaborators who helped in extending my research beyond my group.

My family – my mom Swarnalatha, my brother Chetan Prakash, my sister-in-law Shruthi B.C and my dad Prakash B.S deserve my utmost appreciation for their love, patience and support throughout my studies. My love for mathematics, engineering, science and research is due to inspiration from my brother Chetan.

I thank Dr.Michael S. Wong, Dr. Stefan Link, Richard Crouse and Dr.Douglas Natelson for their support and encouragement.

Last but not least, my friends – Dr.Varun Gauba, Dr.Zannatul Ferdous, Dr.Najmuddin Gunja, Chinmay Hegde, Harini Aruri, Prabha Ramakrishnan, Deepti Ballal, Avani Verma and Reshmy Mohanan have formed the social support that is so vital in the life of a graduate student. I thank them for their constant support.

Again, I would like to thank Dr.Vicki L. Colvin, Dr. Matteo Pasquali and Dr. Clarence A. Miller for taking out the time to serve on my committee.

TABLE OF CONTENTS

LIST OF FIGURES

LIST OF TABLES

CHAPTER 1

Synthesis mechanism of iron oxide nanoparticles – role of oleic acid decomposition in preserving the monodispersity

1.1 ABSTRACT

High temperature synthesis of nanocrystals in non-polar solvents typically produces materials with narrow size distribution and high yields. However, the mechanism leading to the preservation of monodispersity on depletion of monomers is not understood, for example, in the case of iron oxide nanoparticles. In our study, it was found that oleic acid, a surfactant added to the mixture of iron precursor and solvent, gradually decomposed to release carbon monoxide at 320°C. This strong reducing gaseous product had a substantial impact on the size distribution of nanocrystals produced. The reduced forms of iron oxide catalyzed the disproportionation of carbon monoxide resulting in a graphitic carbon deposit on the surface of nanoparticles. The graphite coating inhibited further growth of particles and prevented Ostwald ripening. Graphite presence was demonstrated by Raman spectroscopy and Fourier transform infrared spectroscopy. It was found that the amount of graphite deposited on the surface of nanocrystals increased with time at 320°C. Quantitative data regarding the carbon content was obtained by thermo gravimetric analysis and energy dispersive spectrometry. The surface activity of the nanocrystals was shown to be affected by the carbon coating in applications such as arsenic removal.

1.2 INTRODUCTION

1.2.1 Applications of iron oxide nanocrystals

Synthesis of different nanocrystals such as iron oxide, cadmium selenide, gold and silver has gained a lot of attention in the recent past owing to their tunable properties that could be tailored for various applications.[1-3] Particularly iron oxide nanoparticles , with their unique magnetic properties, have widespread applications in areas like environmental remediation, magnetic resonance imaging, magnetic recording, bioseparations and drug targeting.[2,4-10] Large scale uses of iron oxide nanoparticles in industry range from ore refinement to ferrofluids based oscillation damping and position sensing.[2,11,12]

Nanoparticles are highly effective agents in the aforementioned applications due to their high surface areas, uniform size and size distribution, and possess size dependent physico-chemical properties.[13] Synthetic routes that produce such monodisperse colloidal systems with high crystallinity are hence of crucial importance. In this regard, the understanding of factors leading to monodispersity in nanoparticle systems remains an outstanding challenge for material scientists.

1.2.2 High temperature synthesis

It has been well established that best quality nanocrystals (high crystallinity, uniform shape and narrow size distribution) are generally obtained at high temperatures in organic solvents *via* thermolysis.[1,9,10,14-21] Typically, organic synthesis of iron oxide nanoparticles involves reaction of a mixture containing iron precursor and a surfactant

in a high boiling temperature solvent. This process generally produces nanocrystals whose surfaces are stabilized by organic, non-polar moieties.[1]

1.2.3 Nanoparticle formation

The mechanism of forming such nanocrystals involves two main processes – nucleation and growth, as explained by LaMer model.[13,22-24] Prior to nucleation, precursors or monomers form (for e.g iron oleate complex from the reaction between iron-oxy hydrate FeO(OH) and oleic acid). When the concentration of monomers rises above a threshold termed as supersaturation, nucleation occurs. The concentration of monomers eventually drops below supersaturation on account of their consumption by the nuclei. This ends the nucleation process and growth stage begins, wherein already formed nuclei grow due the addition of further monomers. The growth stage continues until the monomer concentration is reduced to its solubility value.[23] Hence, separation of nucleation and growth to ensure inhibition of further nucleation during growth is imperative for the successful synthesis of nanoparticles. This condition is accomplished in the case of iron oxide nanocrystals due to the different temperature dependence of nucleation and growth kinetics.[9,10,13,25]

Ideal condition for nanoparticle synthesis is therefore rapid nucleation followed with a slow growth rate. In detail, iron oleate complex has three oleate ligands, one of which has been found to dissociate at 200-240°C.[9] The other two ligands dissociate at around 300°C. Nucleation completely ends resulting in growth stage only when all the ligands

dissociate from the iron oleate complex. Hence, allowing time for nucleation below 300°C followed by aging above this temperature is crucial.

Taking the reaction directly to 310°C, researchers reported polydisperse particles. Also, aging at temperatures below 300°C resulted in polydisperse materials. For example, Yin and coworkers obtained cubic shaped wustite nanoparticles at 250°C and also observed polydisperse particles at lower molar ratio of iron source $Fe(acac)_3$ to oleic acid.[26] They used trioctyl amine as the solvent. In the work published by Sun *et al.*, $Fe(acac)_3$ was used with hexadecanediol to form precursors with a mixture of oleic acid and oleylamine as surfactants at a final reflux temperature of 300°C in benzyl ether as the solvent.[12] They were also able to synthesize Co and Mn doped iron oxide particles by adding corresponding metal precursors. Xie and coworkers varied this method by using hexadecanediol to form precursors while keeping other parameters the same.[20] In another report by Huang *et al.*, tetradcanediol was used to obtain a similar result.[8] In all these variations that utilize a temperature of 300°C or more, researchers were able to achieve monodisperse particles.

Hyeons' method utilizes $Fe(CO)_5$ with oleic acid and lauric acid in presence of trimethyl amine oxide as an oxidant at 300°C.[16] They were able to obtain monodisperse particles of Fe_2O_3 using octyl ether as the solvent. Peng and coworkers prepared monodisperse CdSe/InAs nanoparticles by using trioctylphosphine oxide as surfactant at temperatures as high as 350°C.[27] They achieved size focusing by injecting precursors at high temperature (350°C) and lowering the value to 300°C for growth.

As an extreme measure to separate nucleation and growth, seed particles can be used to replace nucleation.[8,9,13,28-31] In seeded growth experiments, pre-synthesized seeds (usually about 3-5 nm) - added to a solution containing precursors below the supersaturation value, are allowed to grow to form bigger nanoparticles. In summary, only a clear separation between nucleation and growth (aging) of at least 20°C results in narrow size distribution of the particles.[25]

The growth stage of nanoparticles is in turn size dependent, and is governed by two competing processes; namely, the diffusion of monomers to the particle surface followed by incorporation of the monomers into the particle and the Gibbs-Thomson effect.[13,23,32-34] In diffusion controlled growth, small particles grow faster than bigger ones owing to their difference in the surface areas. This results in narrowing of the size distribution. In rate controlled growth, where incorporation of new material (proportional to the area of nuclei) is the limiting step, all particles grow at the same rate, thereby, causing no difference to the once established size distribution.[23]

Gibbs-Thomson effect (also called as crystal surface curvature effect) addresses the change of solubility with crystal size.[34] Smaller particles – have high surface curvature leading to a higher surface energy, and hence possess higher dissolution rates than the bigger particles. This interfacial-energy driven dissolution becomes significant in the case of nanoparticles.[33]

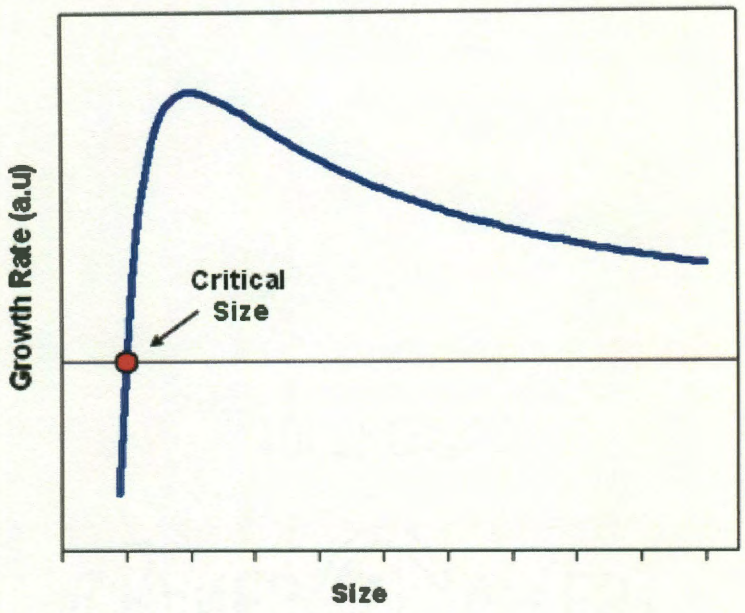

Figure 1.1: Variation of growth rate with size (according to the model of Sugimoto).[13]

In metal and inorganic nanoparticle systems, diffusion controlled growth and Gibbs-Thomson effect have been found to be the determining factors for the resulting size distribution.[33,35,36] At the equilibrium of these two processes, there exists a critical size at which particles neither grow nor diminish in size, and is dependent on the monomer concentration. Higher monomer concentration implies a lower critical size and vice versa.[21] Nanocrystals that are smaller than the critical size have negative growth rates and hence dissolve, and those larger than the critical size grow at rates governed by their size.[27]

Keeping these concepts in mind, one can generalize the size distribution of nanoparticles as follows. The size distribution narrows (or focusing occurs) only if it falls above the critical size, while the monomer concentration is high (or in other words, monomer concentration is maintained at a value higher the solubility of the mean size

of the population). The size distribution broadens if the critical size falls within the size distribution when the monomer concentration is low (Figure 1.1). During this special case of Gibbs-Thomson effect, small particles diminish and form a monomer pool that in-turn leads to the growth of bigger particles. This process is known as Ostwald-ripening (also as defocusing).[13,23,27,32,37] The driving force for Ostwald ripening is the overall reduction of the interfacial surface energy. Hence, broadening of size distribution in any scenario where monomer pool eventually gets depleted is inevitable.[13] Therefore, to obtain monodisperse nanoparticles one has to maintain high monomer concentration or should arrest the reaction before the depletion of monomers.

Surprisingly in our studies monodisperse iron oxide nanoparticles (*via* thermal decomposition of iron carboxylate salts at 320°C) were obtained even after monomer depletion. Hence, our goal was to understand the phenomenon responsible for preserving this narrow size distribution.

Let us begin with an explanation of parameters involved in the synthesis of iron oxide nanoparticles – namely molar ratio of iron source to the surfactant (decides the fate of the precursor), nucleation and growth temperature, and the reaction time. Some of the iron sources that could be used for precursor formation are iron oxy-hydrate (FeO(OH), iron penta-carbonyl ($Fe(CO)_5$) and iron acetylacetonate ($Fe(acac)_3$). Typical surfactants used are oleic acid and oleylamine in high temperature solvents such as octadecene, docosane or eicosene.[10,16,19] Surfactants – not only form an integral part of iron

precursors (such as iron oleate complex), but also provide surface stabilization for nanoparticles.

Size control is highly sensitive to the temperature at which these monomers nucleate and grow. For example, in the case of iron oleate complex and oleic acid in octadecene, nucleation occurs around 240-270°C and growth happens between 270-320°C.[9,10,25] Interestingly, in this system researchers found that in order to obtain monodisperse particles it was imperative to raise the temperature up to 320°C for growth and annealing, while operating with a molar ratio of surfactant to iron source in the range 2-10, whereas using lower temperatures led to polydisperse samples.[9,10] This synthesis procedure is used widely and forms the focus of our study.

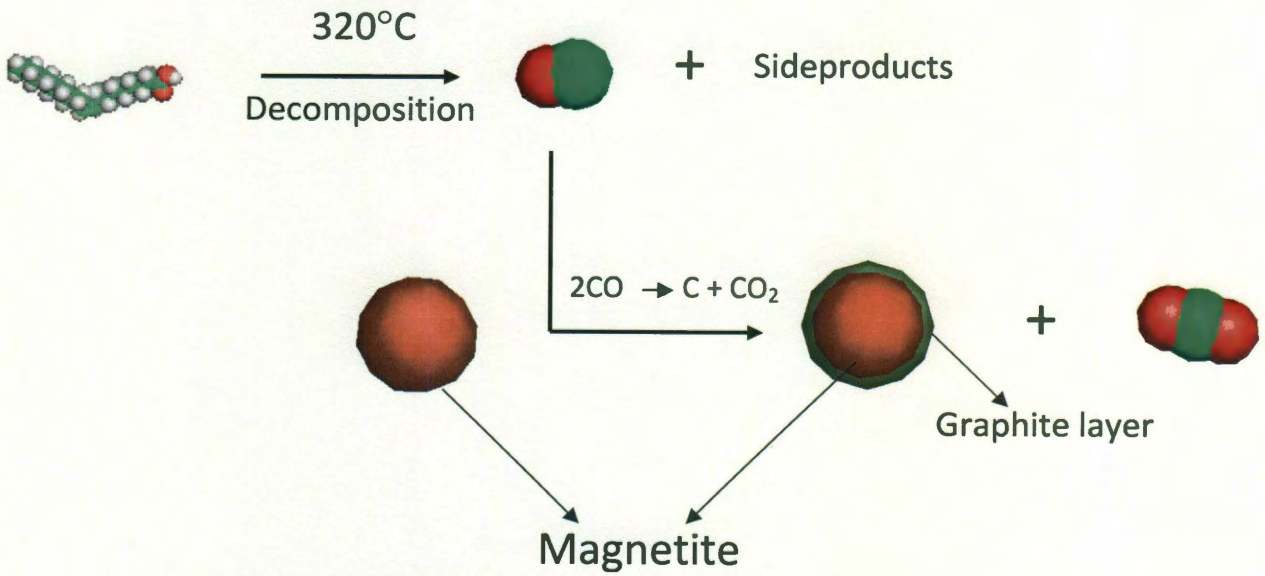

Figure 1.2: Proposed mechanism for oleic acid decomposition during iron oxide nanoparticle synthesis.

1.2.4 Proposed synthesis mechanism

In order to explain the striking monodispersity obtained even after monomer depletion, we propose the following mechanism. At higher temperatures (above 300°C) oleic acid decomposes at a faster rate, using iron oxide particle surface as a catalyst. This catalytic activity is believed to occur on the defect sites of nanocrystals and is enhanced due to their extreme surface curvatures.[38] Oleic acid decomposes mainly into carbon monoxide, carbon dioxide, water and hydrocarbons.[39]

In turn, the CO evolved acts as a strong reducing agent on the surface of nanoparticles. The resulting reduced forms of iron oxide (such as wustite and zero valent iron – shown in reactions a-d below) catalyze the disproportionation of carbon monoxide.[39-41] CO gets converted into graphitic carbon, which deposits on the surface of nanoparticle and evolves CO_2 (Figure 1.2).

During annealing from high temperatures, carbonaceous coating has been observed to form on nanoparticle surfaces.[42-44] Researchers have found iron oxide nanoparticles to be much more effective in the catalytic oxidation of carbon monoxide than bigger micron sized particles.[40] In a study by Li and coworkers, 50mg of iron oxide nanocatalyst was found to oxidize almost 100% of CO at 350°C. Particularly, they found that CO conversion into CO_2 peaks above 300°C (Figure 1.3).[40]

$$2Fe_3O_4 + 2CO \rightarrow 6FeO + 2CO_2 \quad \text{(a)}$$

$$6FeO + 6CO \rightarrow 6Fe + 6CO_2 \quad \text{(b)}$$

$$2Fe_3O_4 + 8CO \rightarrow 6Fe + 8CO_2 \quad \text{(c)}$$

$$2CO \xrightarrow{Fe} C + CO_2 \quad \text{(d)}$$

Reaction Scheme 1.1: Magnetite gets reduced to wustite (a)- which being unstable below 560°C gets converted to zero valent iron (b). This freshly formed iron catalyzes (d) $CO \rightarrow C + CO_2$.[39-41]

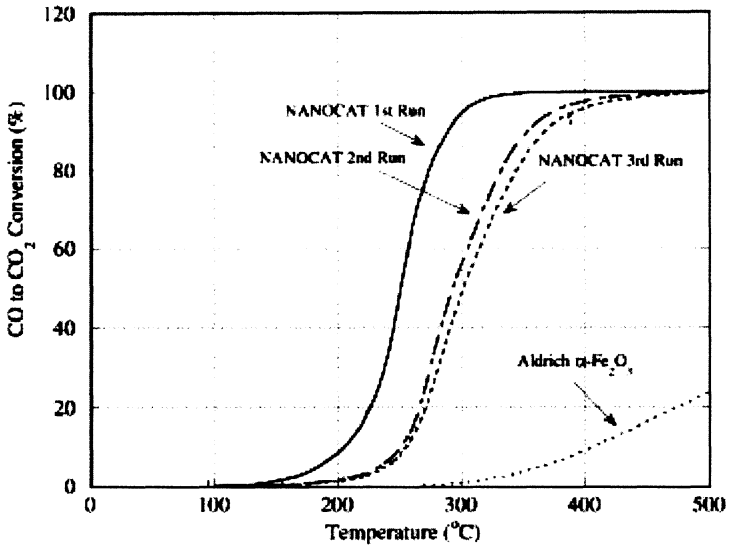

Figure 1.3: Comparison of carbon monoxide conversion efficiencies between Nanocat® iron oxide catalyst and micron sized Fe_2O_3 powder.(Taken from Li 2003)[40]

Various characterization methods were employed to prove that the carbon layer on iron oxide nanoparticles preserves monodispersity. Graphitic carbon was found to be present on the surface of iron oxide nanoparticles, and its amount was seen to increase with longer annealing times when oleic acid decomposition was allowed to reach completion.

1.3 RESULTS AND DISCUSSION

1.3.1 Iron oxide nanoparticle formation

In a typical synthesis, reaction mixture (FeO(OH) - 0.176g, oleic acid – 2.24 g in 1:4 molar ratio) was maintained at 270°C in 1-octadecene for ½ hr followed by raising and holding the temperature at 320°C for 1hr under an inert gas such as nitrogen or argon.[10] This procedure yields monodisperse iron oxide nanocrystals.

As discussed above nanoparticle formation involves two stages – nucleation and growth.[21] Prior to nucleation, iron oleate precursors form between 240-270°C using FeO(OH) as the iron source and oleic acid as the surfactant. The majority of iron oleate complex formed has three oleate groups attached to iron in a bidentate configuration as shown below (Figure 1.4).[25] One oleate group dissociates from the complex in the range 200-240°C and the other two dissociate around 300°C.[9,25] Hence, the choice of synthesis temperature is dictated by the thermal characteristics of the iron oleate complex.

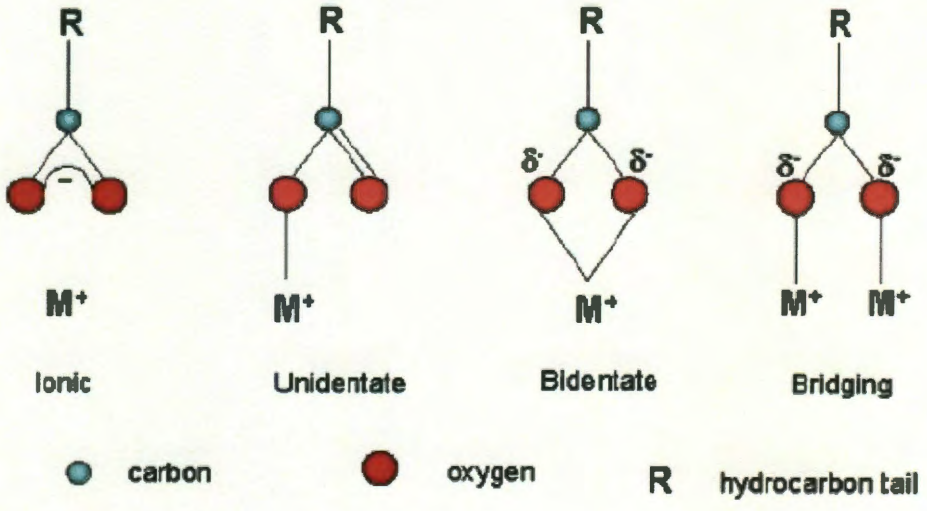

Figure 1.4: Different possible configurations of iron-oleate complex. (From Bronstein 2006)[25]

Nucleation takes place around 270°C, followed by growth of particles at 320°C. The monomer pool depletes at around 30min at 320°C which, should result in nanocrystals with broad size distribution. Instead monodisperse particles are formed that indicates the occurrence of a simultaneous process. So we proposed the hypothesis of carbon coating due to oleic acid decomposition at high temperatures. In order to demonstrate our hypothesis two synthesis scenarios were designed - one with half the amount of oleic acid than the other.

When the molar ratio of FeO(OH) to oleic acid is 1:2, iron precursors that form the monomer pool nucleate at around 270°C followed by particle growth and annealing between 270-320°C (Figure 1.5A). Size focusing starts to occur during the growth stage when the monomer concentration is still relatively high, as the critical size falls below the distribution of particles.[21,24,27,45,46] However, monomer pool gets depleted at 320°C with time; at this stage, critical size falls within the size distribution and leads to Ostwald ripening or size broadening. Bigger particles start growing at the expense of the dissolution of smaller particles and this gives rise to polydisperse population.[21]

The second scenario under consideration uses a molar ratio of 1:4 (Figure 1.5B). All the oleic acid is not used up for monomer formation and hence some of it is present in excess. Nucleation, particle growth and size focusing proceeds exactly as the previous case, but the oleic acid decomposition accompanies this process and peaks at 320°C. Oleic acid decomposes to give CO which then disproportionates on the iron oxide nanoparticle surface to form a graphitic carbon coating. This step occurs in conjugation

with monomer depletion; the propensity towards inter-particle exchange of material is now blocked or inhibited by the presence of carbon coating. This phenomenon prevents size broadening or Ostwald ripening, thereby preserving the already achieved monodispersity.

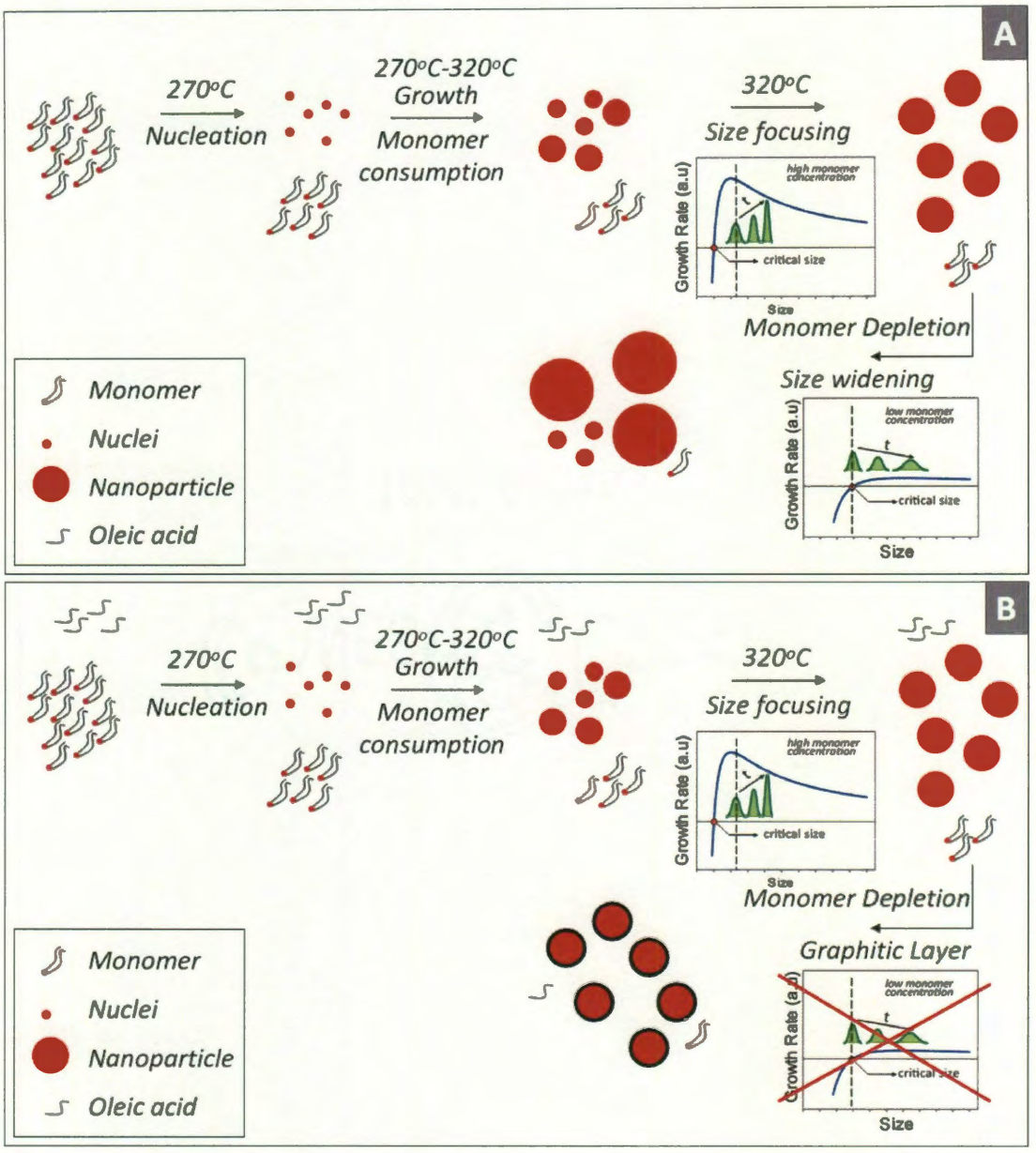

Figure 1.5: Iron oxide nanoparticle growth model without excess fatty acid (A) and with excess fatty acid (B).

1.3.2 Hypothesis and background

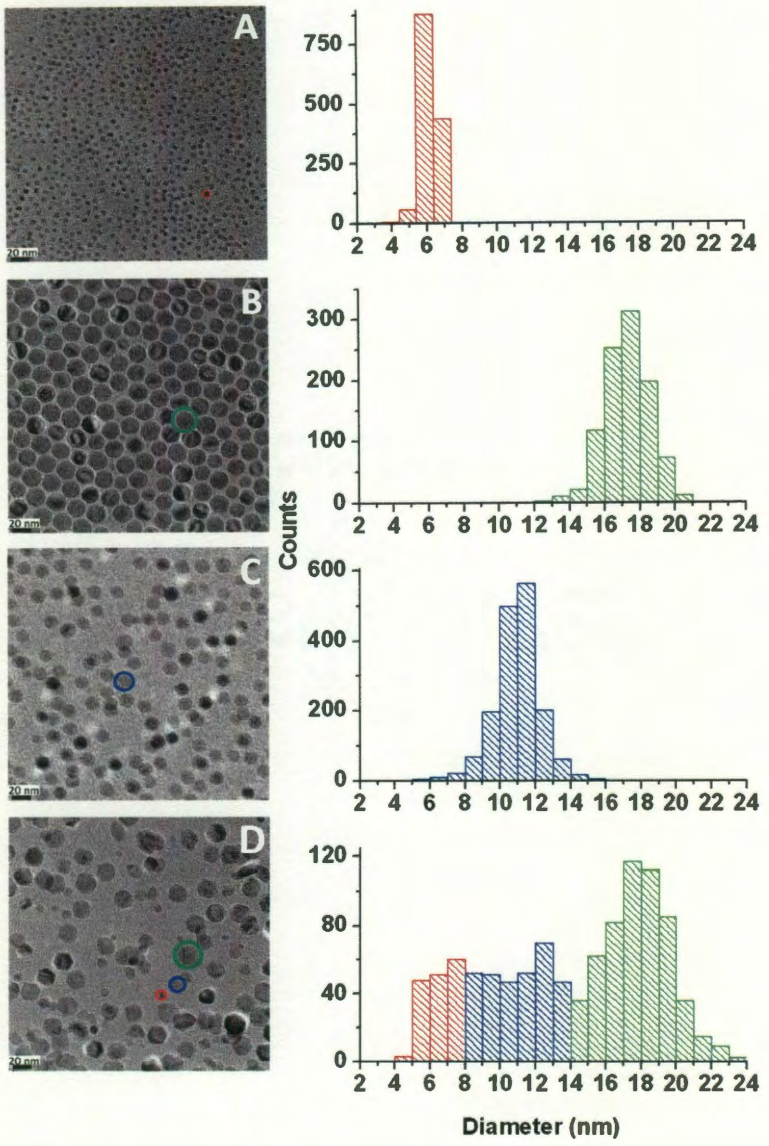

Figure 1.6: TEM results depicting the absence of competitive growth. A (5 nm - red) and B (18 nm - green) pre-synthesized nanoparticles were mixed with iron oxide precursors to obtain tri-modal distribution of particles shown in D. New population of 11 nm size particles was formed (shown in blue). Also, pre-synthesized 11 nm particles (C) is shown for comparison.

Iron oxide particles, once synthesized *via* thermal decomposition route at 320°C do not grow further on precursor addition. Seeded growth of nanoparticles below 300°C using oleic acid as the surfactant has been observed to occur in several systems.[9,19,47] An experiment was performed to check if the seeds (pre-synthesized particles) prepared at 320°C undergo seeded growth, and hence their susceptibility towards further increase or reduction in size.

A reaction mixture of FeO(OH):OA in 1:4 molar ratio, in general, produces 11 nm iron oxide particles when held at 320°C for 1hr (Figure 1.6C). Two pre-synthesized particle sizes of 5 (Figure 1.6A) and 18 nm (Figure 1.6B) were added to such a starting mixture and synthesis was carried out under identical conditions of time and temperatures. Surprisingly, three different populations of particle sizes were seen (Figure 1.6D); the pre-synthesized particles neither grew nor diminished in size in presence of new monomer pool, that in-turn independently led to a new population of 11 nm particles. This implied that particles once formed by annealing at 320°C are not susceptible for further change in size. In perspective of the proposed hypothesis, this indicates the inhibition of particle surface for further addition of monomers.

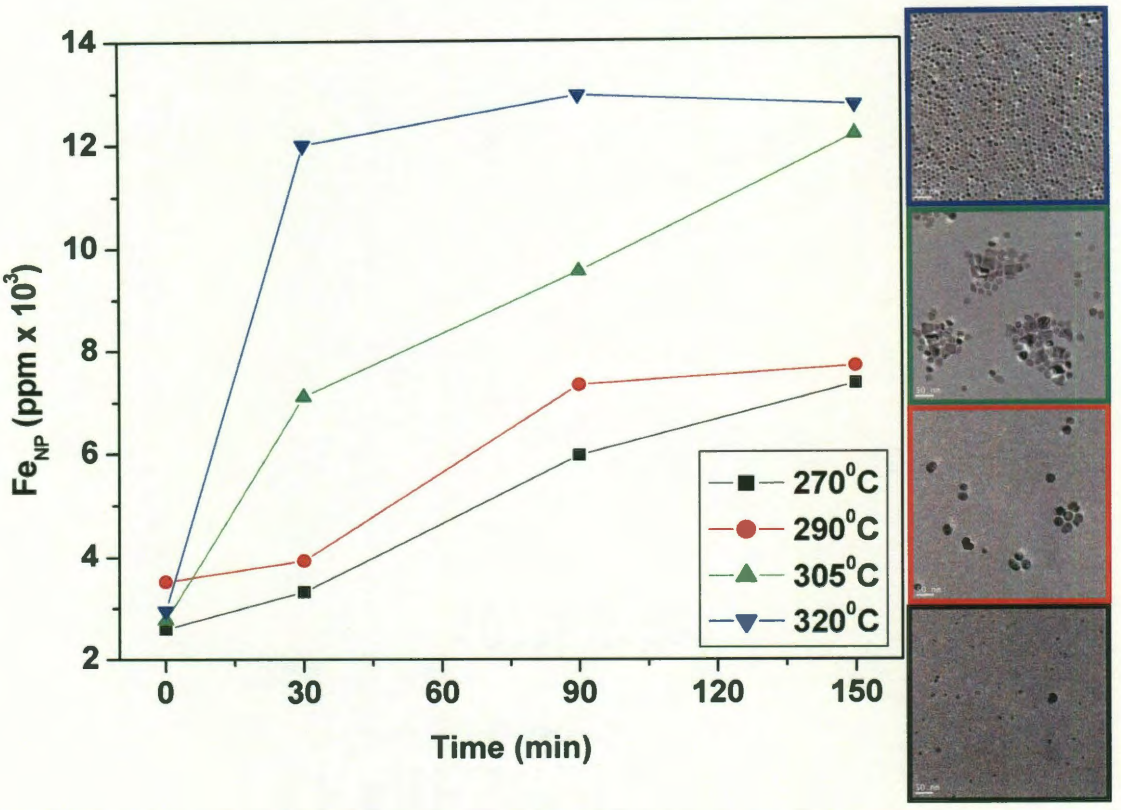

Figure 1.7: Fe concentration of iron oxide nanoparticles vs. time. The plot depicts the higher yield obtained at 320°C as opposed to other lower synthesis temperatures.

Monomer depletion occurs faster at higher temperatures (30min/320°C). In general, higher monomer utilization implies a higher synthesis yield. The amount of monomers consumed in the formation of nanoparticles was analyzed by computing the iron concentration in the nanoparticles using inductively coupled plasma analysis (ICP). Iron oxide nanoparticles were synthesized at different maximum temperature values (T_{max}) ranging from 270-320°C. Samples were taken at different intervals and analyzed for concentration (Figure 1.7). In all these syntheses, temperature was first maintained at 270°C for nucleation (corresponding to first set of points in Figure 1.7) followed by raising and holding the temperature at different T_{max} values for about 3hrs. It was seen

that the amount of monomers (iron oxide precursors) consumed to form nanoparticles peaked at 320°C.

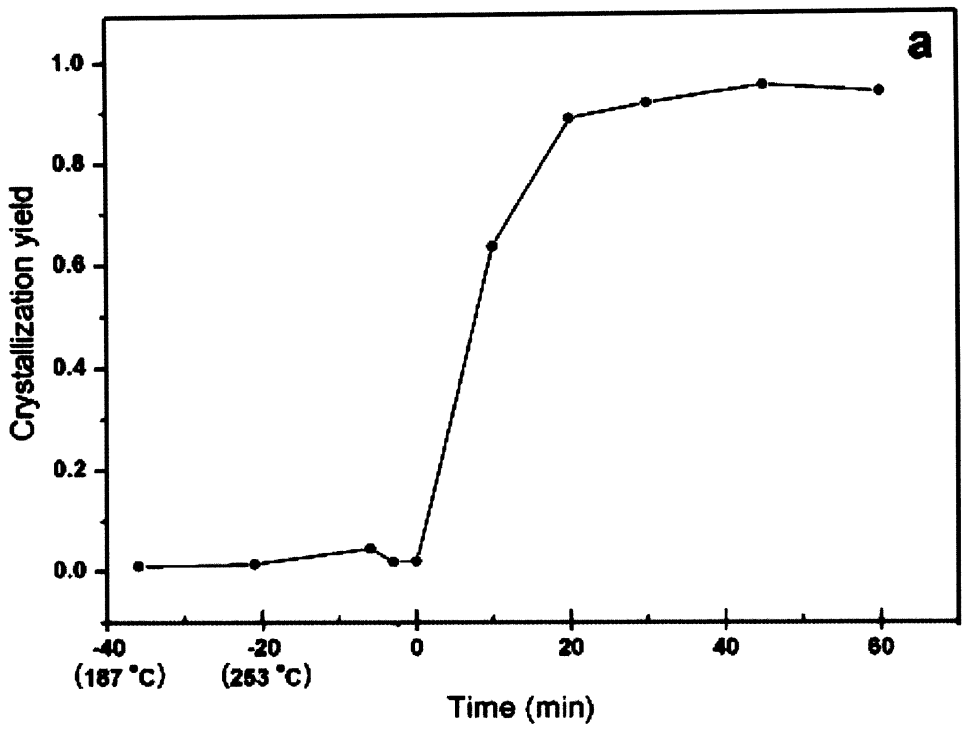

Figure 1.8: Change in crystallization yield as a function of temperature. (From Kwon 2007)[48] From time t=0 at 320°C the yield can be seen to increase with time and maximize after 20min.

In general, Fe conversion increased with both time and temperature. Also, monomers were observed to be used up at 305°C when held for three hours. Rate of monomer incorporation increased at higher temperatures as expected due to faster diffusion of monomers.[21] Hence, after this stage of monomer depletion, one would expect Ostwald ripening to occur due to the dissolution of smaller particles. Kwon and coworkers observed a similar result with respect to monomer depletion, as shown in the figure above (Figure 1.8). Their crystallization yield maximized with monomer depletion after 20min of aging at 320°C. Interestingly, they did not use any surfactant, but just pre-

formed precursors in a solvent, and observed that the size distribution broadened at 320°C when held for longer periods of time.[48] On the contrary, when excess oleic acid was used as a surfactant in our method, particle size distribution focused at 320°C. At synthesis temperatures below 320°C the particles obtained were polydisperse in nature (Figure 1.7).

Size focusing of the particles was observed at 320°C, below which particles were polydisperse. To get a visual depiction of the process TEM images were obtained at different temperatures and time during a typical synthesis. As shown in the Figure 1.9 nucleation occurs between 240-270°C. With the increase in temperature upto 310°C, particles grow into a polydisperse population; but the particle morphology gets well defined. At 320°C, size focusing starts to occur progressively with time. Narrow size distribution is achieved after about an hour at this temperature. Similar observation was made by Zhang and coworkers where annealing at a higher temperature resulted in a better size distribution (Figure 1.10).[47] Hence this implies that at 320°C where monomer depletion occurs, a simultaneous process has to occur that would prevent size broadening.

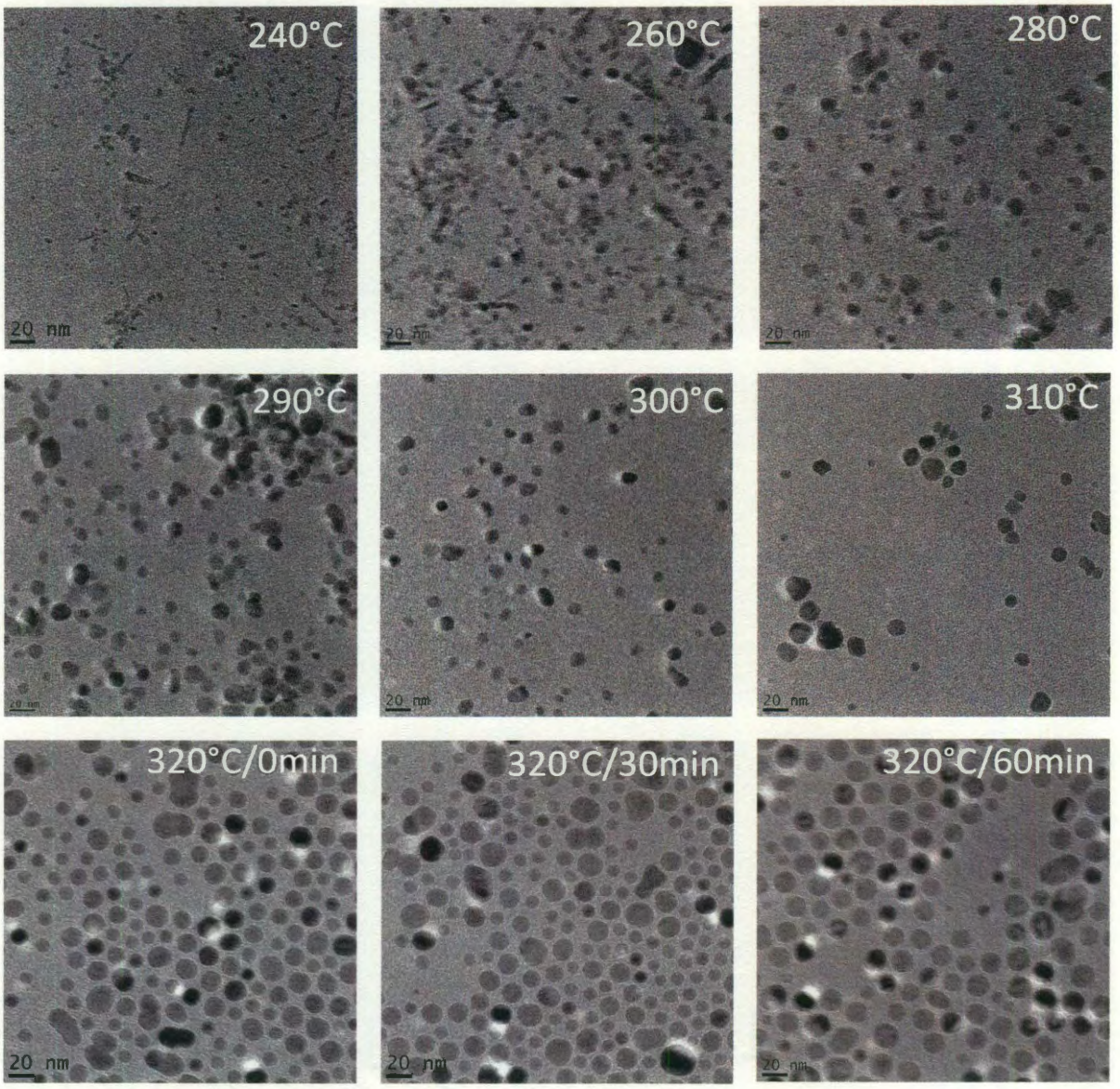

Figure 1.9: Temperature/time evolution of iron oxide nanoparticles from 240-320°C.

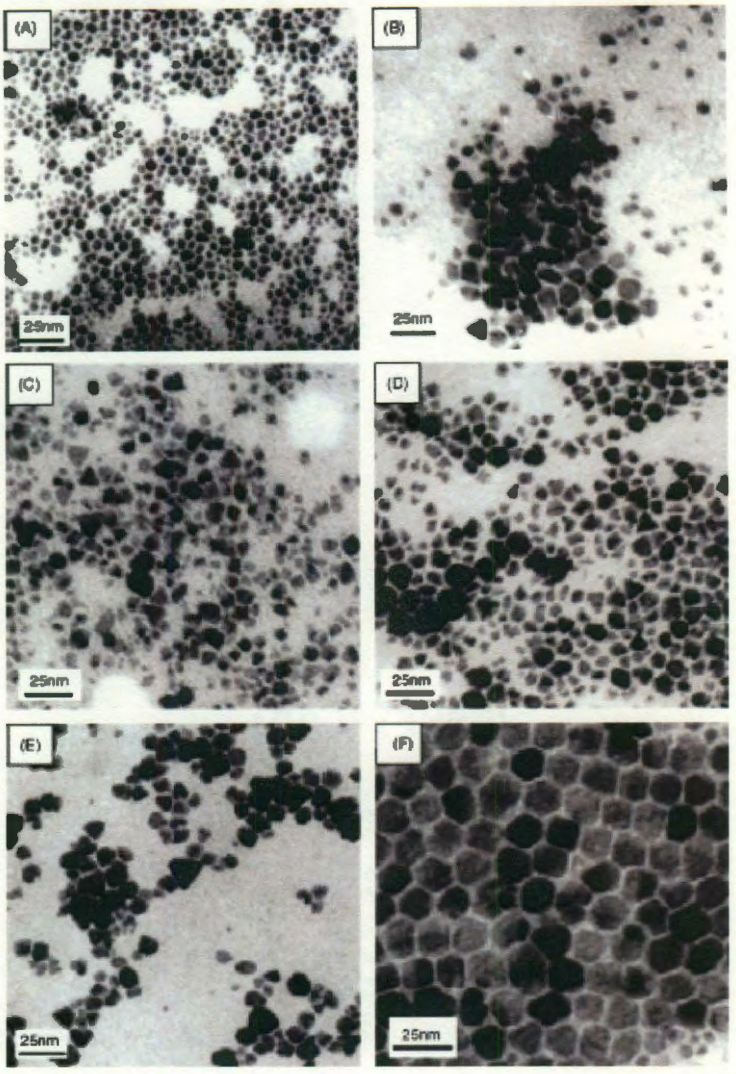

Figure 1.10: TEM images of magnetite nanoparticles with different reaction stages: (A) seeds of 6 nm magnetite nanoparticles, (B) 15 min, (C) 30 min, (D) 45 min, (E) 60 min, after the seed-mediated growth reaction (200°C), (F) 30 min after anneal treatment (300°C). (From Zhang 2006)[47]

1.3.3 Graphite Presence

Raman spectroscopy confirms the presence of graphite on the surface of iron oxide nanoparticles. Raman spectroscopy is one of the most widely used characterization tools for the presence of graphite, as conjugated C=C bonds lead to high Raman

intensities; also, it can give information about the number and quality of graphitic layers.[49-51]

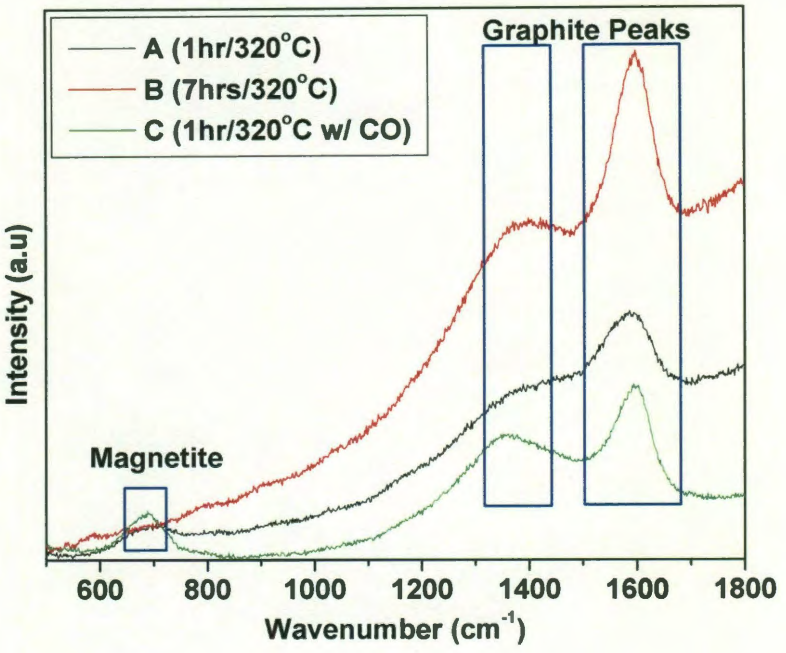

Figure 1.11: Raman spectra of iron oxide nanoparticles. Graphite peaks (1580 – in plane E2G and 1377 cm^{-1} – disorder D band) are clearly detected for samples A, B and C. Magnetite peak (670 cm^{-1}) is seen for samples A and C but not B. Higher amounts of graphite is seen for sample B in comparison with A and C.

Two samples that are considered throughout this study - one obtained by maintaining 320°C for 1hr (Figure 1.11A) and the other for 7hrs (Figure 1.11B), were analyzed using Raman spectroscopy. For both the samples in question two first order spectrum peaks – an in-plane G peak at 1580 cm^{-1}, which appears due to bond stretching of sp^2 carbon pairs and D peak at 1377 cm^{-1} (breathing modes of sp^2 carbon atoms in rings) that appears due to disorder in the laser focal spot, are seen.[49-51] The D and G peaks clearly prove the presence of graphitic carbon on the surface of iron oxide particles. Furthermore, for amorphous sp^2 carbon G peak appears at 1510 cm^{-1} and not at 1580

cm^{-1}. This corroborates that the carbon present on the surface of the samples analyzed is crystalline in nature.

Also, iron oxide, in the form of magnetite peak is found at 670 cm^{-1} for 1hr sample but not for 7hrs sample.[52] It suggests that, even though 7hrs sample has magnetite (as seen from XRD), its signal is being blocked by a substantial amount of carbon deposition on the surface. As expected, similar Raman spectra was obtained when the reaction mixture was pumped with pure CO at 320°C (Figure 1.11C), providing further evidence for the formation of graphite *via* CO disproportionation.

In flake graphite, a double resonance second order spectrum peak is usually obtained at 2700 cm^{-1}, but cannot be seen on the surface of nanoparticles due to edge effects. In principle, electronic bond structure associated double resonance of sp^2 bonded carbon materials like graphite leads to a D* overtone in the second order spectrum.[49] The G and D* peaks change in shape, position and relative intensity with the number of graphene layers and disorder. With the increase in disorder in the graphitic structure, the G peak position shifts from ≈1580-1600 cm^{-1} and also broadens. This can be seen to occur for the 7hrs sample (which has 2-3 layers of graphite as will be shown later) and can be attributed to the curvature affects associated with surface coverage of nanocrystalline graphite.[49] Also, G peak in the 1hr sample is at 1586 cm^{-1} which, indicates a graphene layer.[50]

To support these findings, Fourier transform infrared spectroscopy (FTIR) was performed. Aromatic carbon stretching couplet was seen in all the samples, providing

further evidence for the presence of graphite (Figure 1.12). Two distinct aromatic carbon peaks can be seen at 1462/1419.2 cm^{-1} in 1hr and 7hrs sample.[53] As expected, the carbonyl peak from oleic acid at 1715 cm^{-1} is diminished, due to the formation of organometallic complex between oleic acid and the iron oxide surface. FTIR spectra of just oleic acid (control) shows a much higher carbonyl peak while showing a single band for sp^2 carbon stretching. This comparison between control and samples suggests the presence of an additional aromatic C=C stretching on the surface of iron oxide nanoparticles.

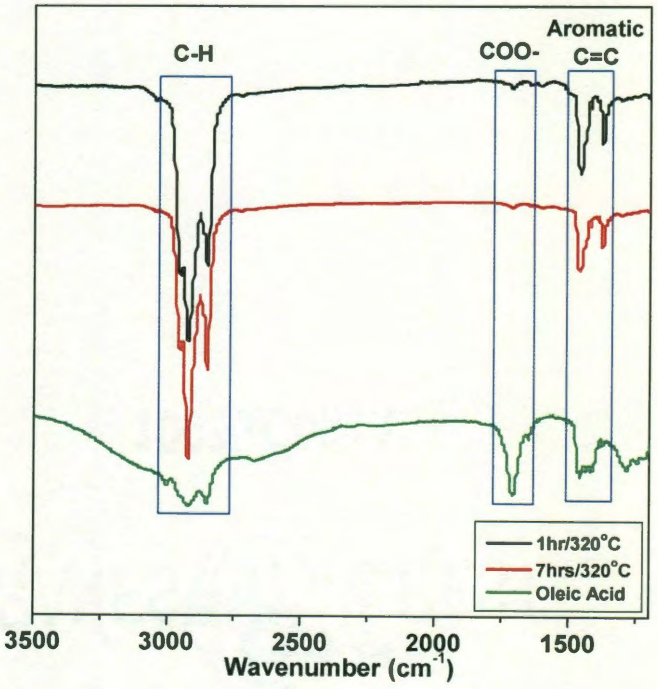

Figure 1.12: FTIR spectra of iron oxide nanoparticles. All samples clearly indicate the graphitic aromatic carbon stretching (1462 and 1419 cm^{-1}), C-H stretching (2953-2853 cm^{-1}) from oleic acid hydrocarbon chain and carbonyl group (1715 cm^{-1}) of the oleic acid.

1.3.4 Mechanism

After proving the presence of graphite, we looked closer into the mechanism of graphite formation. As mentioned earlier, CO evolved during oleic acid decomposition at 320°C interacts with iron oxide surface, forming graphitic layer while releasing CO_2 in the process. CO_2 is also a common decomposition product of hydrocarbons.[54] Oleic acid decomposes to give CO, CO_2, water, hydrocarbons and other side products.[39] The reduced forms of iron oxide resulting due to the action of CO, catalyze the disproportionation of CO on the surface.[55]

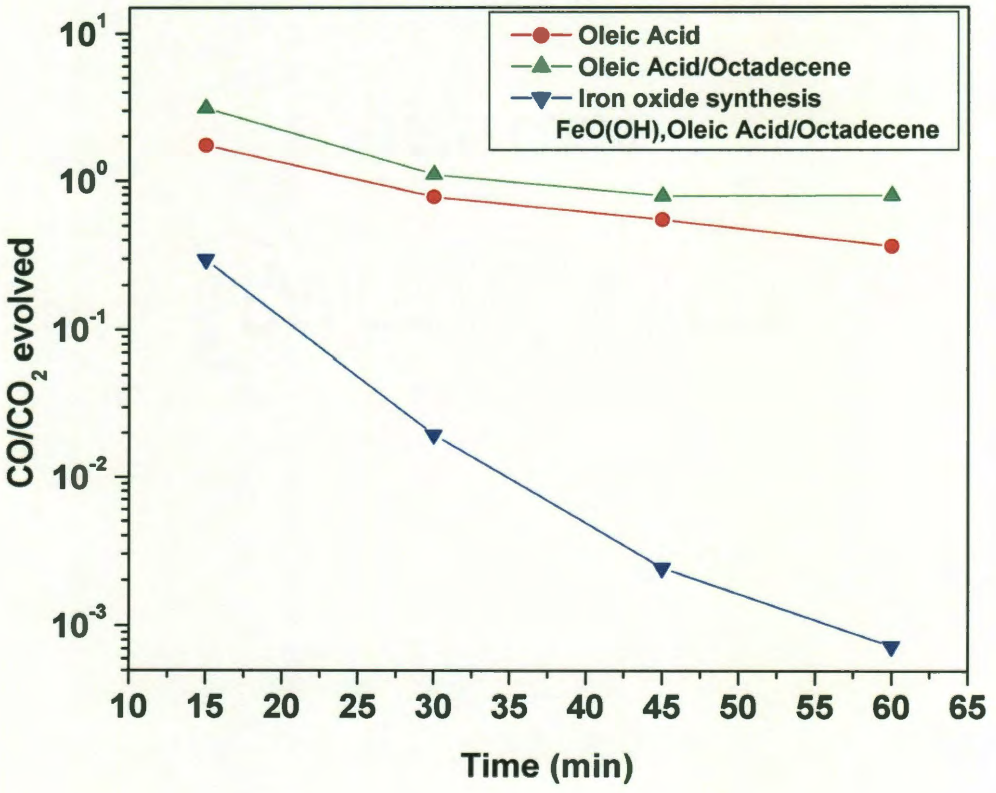

Figure 1.13: Ratio of CO/ CO_2 evolved vs. time at 320°C as computed from GC-MS.

Gas chromatography - mass spectrometry (GC-MS) was performed in order to quantitatively analyze the extent of gases evolved. As seen in Figure 1.13, CO/ CO_2 ratio

evolved during decomposition of just oleic acid or a mixture of oleic acid/octadecene at 320°C gradually decreases in the range 3-0.5. Whereas in the presence of iron oxide particles (that can catalyze the fatty acid decomposition), the ratio falls sharply.

More specifically, the CO/ CO_2 ratio evolved during iron oxide synthesis differs by three orders of magnitude in comparison with that of only oleic acid or a mixture of oleic acid and octadecene indicating the utilization and conversion of CO to CO_2 during iron oxide synthesis. Also, from GC-MS data - the rate of oleic acid decomposition can be seen to be the highest at 15 min after reaching 320°C. This is in agreement with the size sharpening that starts to occur around the same time (Figure 1.9).

Previous studies have thrown light upon the mechanism of CO conversion on iron oxide surfaces.[55] The reactant gas, CO evolved from the decomposition of oleic acid diffuses to the reaction site on the nanoparticle. CO gets adsorbed on the surfaces and reduces iron oxide. The reduced forms catalyze the disproportionation of CO depositing carbon on the surface followed by desorption of the product gas CO_2. The carbon dioxide then diffuses into the bulk.

Disproportionation of CO on iron oxide particle surface can be monitored by following the evolution of CO_2. The difference between the carbon dioxide amounts evolved during iron oxide synthesis and the control mixture of oleic acid and octadecene gives the value of carbon dioxide that is primarily evolved by the conversion of CO. This analysis shows that the rate of graphite formation peaks at 30min at 320°C when CO_2 evolved is at its highest (Figure 1.14).

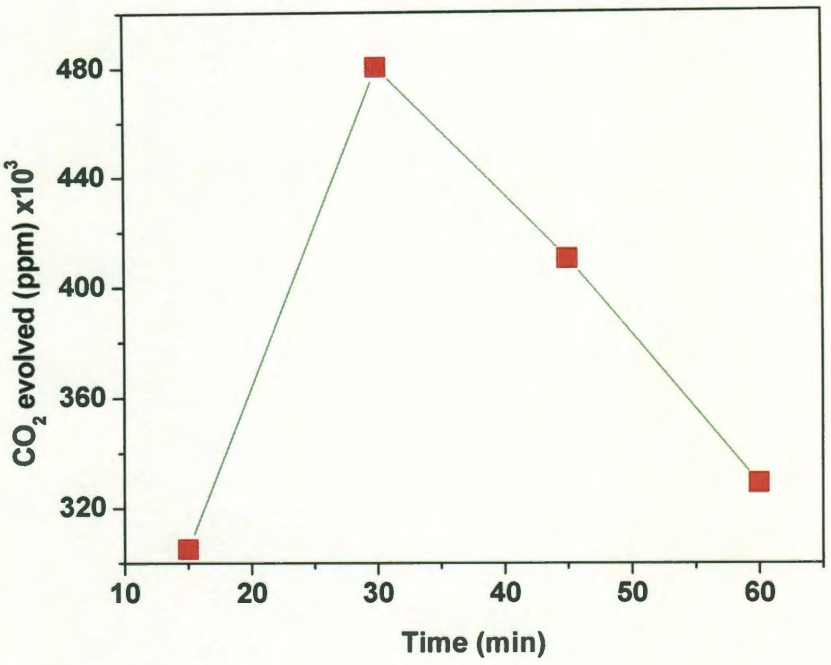

Figure 1.14: Evolution of CO_2 at 320°C.

The data further confirms that oleic acid decomposition during iron oxide synthesis is high enough only at 320°C, and that the coincidence of graphite formation with monomer depletion plays a key role in controlling the size distribution of particles.

Figure 1.15: X-ray diffraction data of particles obtained at 1hr and 7hrs at 320°C and 1hr with CO bubbling.

Furthermore, the reduced forms of iron oxide from the action of carbon monoxide were monitored *via* X-ray diffraction. Magnetite gets reduced to wustite, that decomposes to

α-Fe easily, which in turn catalyzes the disproportionation reaction of CO.[25,26,39,44] Wustite being unstable, can be found on the surface of iron oxide particles only if present in significant amounts. The 7hrs sample, subject to longer reduction can be seen to contain about 22% wustite; whereas, the 1hr sample does not register any wustite in the whole pattern fitting (WPF) refinement done on the XRD data (Figure 1.15). The 1hr sample with CO bubbling shows a greater amount of wustite (37%) due to a higher flux of CO diffusing to the surface of the iron oxide particles. This data further proves the strong reducing action of carbon monoxide. In addition, a wustite monolayer being unstable can react with oleic acid better than magnetite to form the organometallic complex that renders stabilization for iron oxide particles.

1.3.5 Quantification of graphite

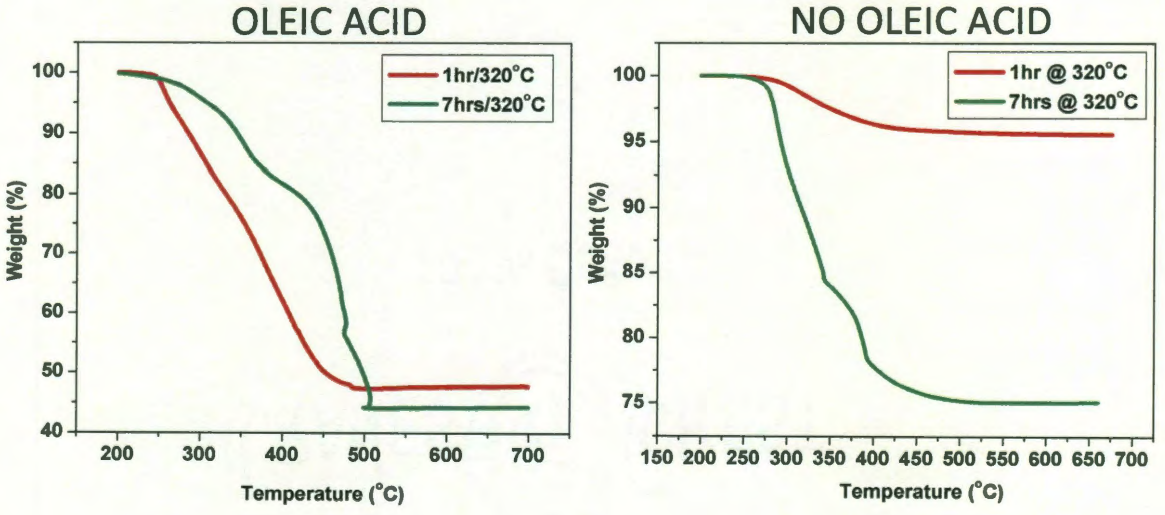

Figure 1.16: TGA data of iron oxide nanoparticles with (right) and without (left) oleic acid coating.

Sample	$C_{graphite}$ wt%	$C_{oleic\ acid}$ wt%	# Graphite layers
1hr/320°C	4.2	45.4	0.4
7hrs/320°c	25.0	25.8	2.9

Table 1.1: Contribution of carbon from oleic acid and graphite on the surface of iron oxide nanoparticles.

After mechanistic study, the next step in this direction was to analyze the amount of graphite present on iron oxide nanoparticles and to see if it increased with synthesis duration. To get this quantitative information, thermo-gravimetric analysis (TGA) was carried out on two sets of samples, one devoid of any oleic acid surface coating and the other in the presence of oleic acid. Each set had samples prepared for 1hr and 7hrs at 320°C respectively (Figure 1.16). This served two purposes, one to confirm the presence of carbon on the surface after removal of surfactant, two to get quantitative information about the amount of carbon content contributed by graphitic layer and oleic acid individually.

Total carbon content in 1hr and 7hrs sample was 47.6 and 50.8 wt% respectively. Individual breakdown of carbon content from graphite and oleic acid is shown in Table 1.1. We can see that the amount of graphite on 7hrs sample is about 6 times that on 1hr sample, from which we can compute the number of carbon layers on the nanoparticle surface as 0.4 graphene monolayer (40% of surface coverage) for 1hr sample and 3 layers of graphite on 7hrs sample. The calculation assumes full surface coverage of carbon layers. Further analysis of the data shows that 1hr sample has twice the oleic acid (6700 OA/NP – number of oleic acid molecules/nanoparticle) coverage in

comparison with 7hrs sample (3600 OA/NP). This indicates pronounced decomposition of oleic acid at longer durations leading to cleavage of oleic acid with the buildup of graphitic layer on nanoparticle surface.

The data obtained by TGA analysis was reflected in the elemental mapping using Gatan image filter (GIF) in high resolution transmission electron microscopy. 1hr and 7hrs sample devoid of any oleic acid were analyzed in order to visualize the extent of graphite coverage on nanoparticle surface. An enhanced amount of carbon (mapped in red) was seen in the 7hrs sample compared to the 1hr sample (Figure 1.17). This was expected as 7hrs sample has more carbon layers than the 1hr sample. Particles are seen to be aggregated due to the removal of the surfactant. This result further proves that oleic acid decomposition - if allowed to go to for a longer duration will deposit more carbon on the particle surface.

Energy dispersive spectroscopy (EDS) gives the weight and the atomic percentages of constituent atoms in iron oxide samples. The results in Table 1.2, clearly show an increased amount of graphite on 7hrs sample as opposed to 1hr sample (in corroboration with TGA and GIF data). Also, previous research that found several layers of graphite on surface of an iron-platinum particles by annealing at high temperatures found about 40-50 atomic percentage of carbon content.[42] This supports the 45% atomic content obtained for carbon in the 7hrs sample. Furthermore, the ratio of atomic percentages of iron to oxygen confirms that the iron oxide phase present is magnetite (in addition to XRD).

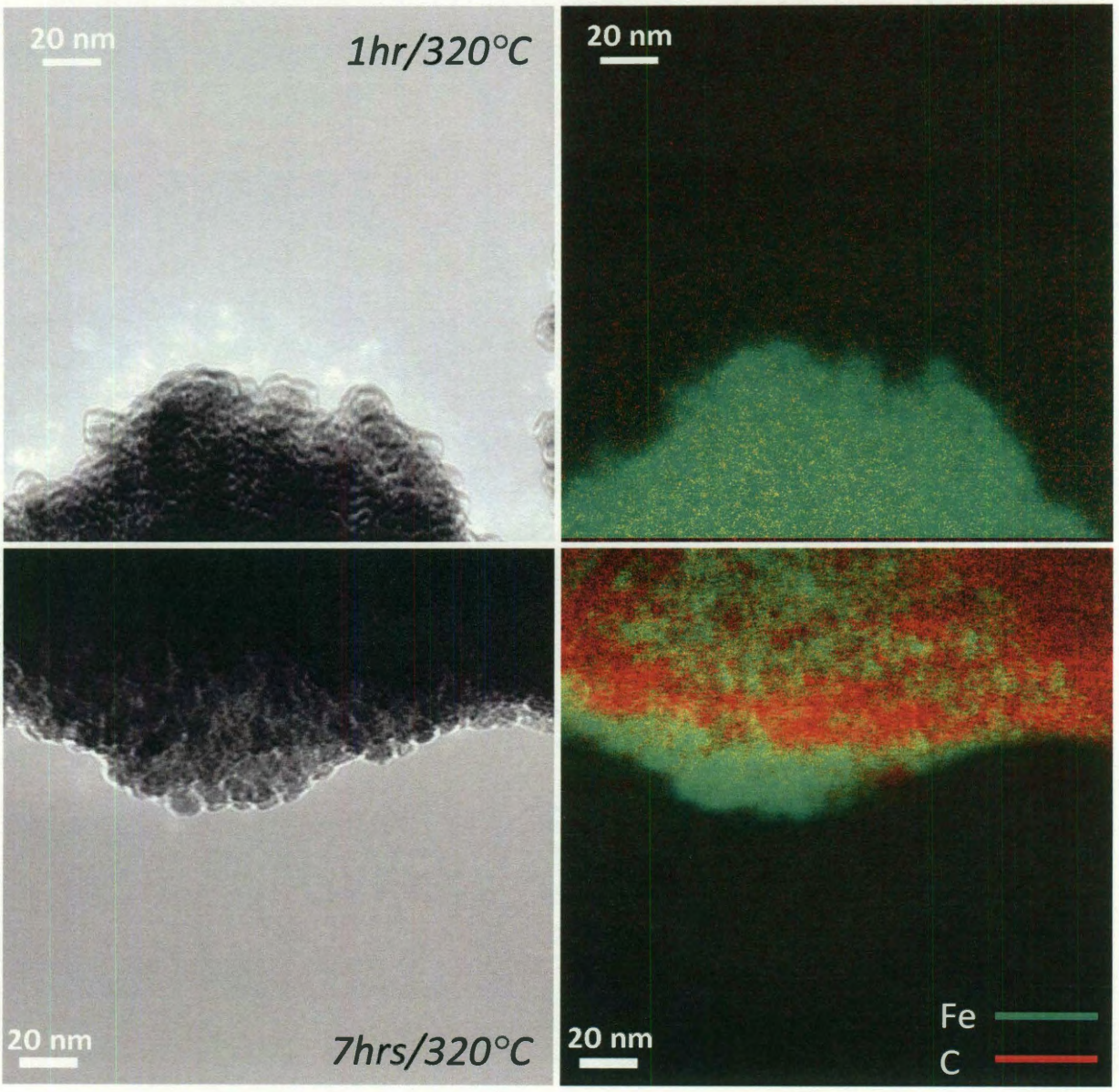

Figure 1.17: GIF analysis of HRTEM images of 1hr/320°C and 7hrs/320°C sample.

Sample (Wt %)	C	Fe	O
1hr/320°C	7.2	65.1	27.7
7hrs/320°C	23.2	54.4	22.4

Sample (At %)	C	Fe	O
1hr/320°C	17.2	33.3	49.5
7hrs/320°C	44.9	22.6	32.5

Table 1.2: Wt% and At% of constituent atoms obtained from EDS.

As further evidence, X-ray photo-electron spectroscopy (XPS) performed on the surface of iron oxide nanoparticle shows higher carbon content in 7hrs sample (Figure 1.18). XPS was carried out on 1hr and 7hrs sample to look for differences in the amount of carbon coverage. Carbon peak intensity in 7hrs sample is two times that in 1hr sample at 45 degree scan (as seen by the C1s peak at 284.5 eV). The satellite π- π^* transition peak at 290 eV for 7hrs sample is more prominent than that for 1hr sample indicating an enhanced carbon to carbon layer interaction. Furthermore, the iron 2p peaks are higher in intensity for the 7hrs sample. This is expected as greater carbon content in the 7hrs sample reduces the signal from the iron on the surface.

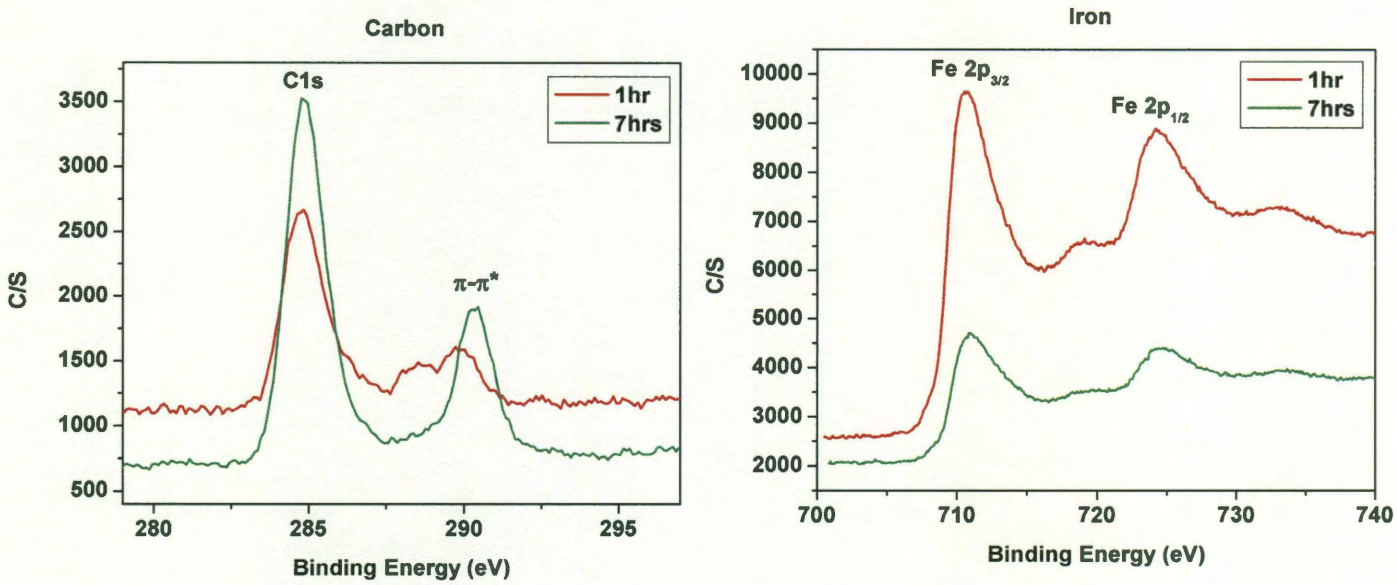

Figure 1.18: X-ray photoelectron spectra of 1hr and 7hrs samples scanned at 45°.

1.3.6 Further evidence

Presence of higher quantities of oleic acid results in a greater decomposition followed by graphitic layer coating on iron oxide nanoparticles that inhibits further growth, preventing the broadening of size distribution on account of monomer depletion. To get a secondary verification of this process, iron oxide synthesis was carried out with different ratios of FeO(OH):OA - 1:4 and 1:2 while keeping other conditions a constant (270°C ½ hr; 320°C 1 hr). As expected, synthesis with 1:4 formed 11 nm monodisperse particles, whereas that with 1:2 molar ratio resulted in a polydisperse sample. This shows that graphite layer is formed in presence of excess oleic acid, but not when lesser amount of oleic acid is present. It proves again that graphite layer coating preserves

monodispersity (Figure 1.19A) on monomer depletion at 320°C, while its absence results in broadening of size distribution (Figure 1.19B).

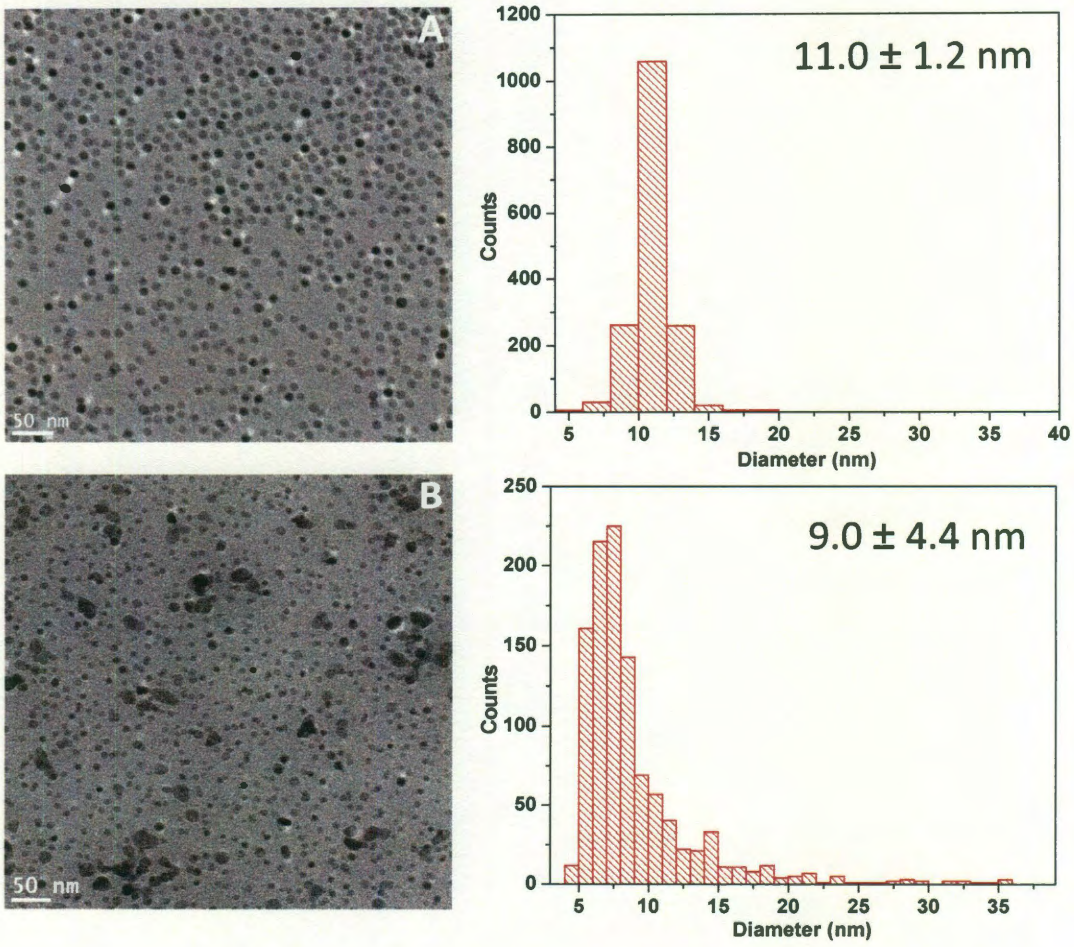

Figure 1.19: TEM images showing the stark contrast in size distribution obtained with FeO(OH)/Oleic acid ratios of 1:4 (A) and 1:2 (B).

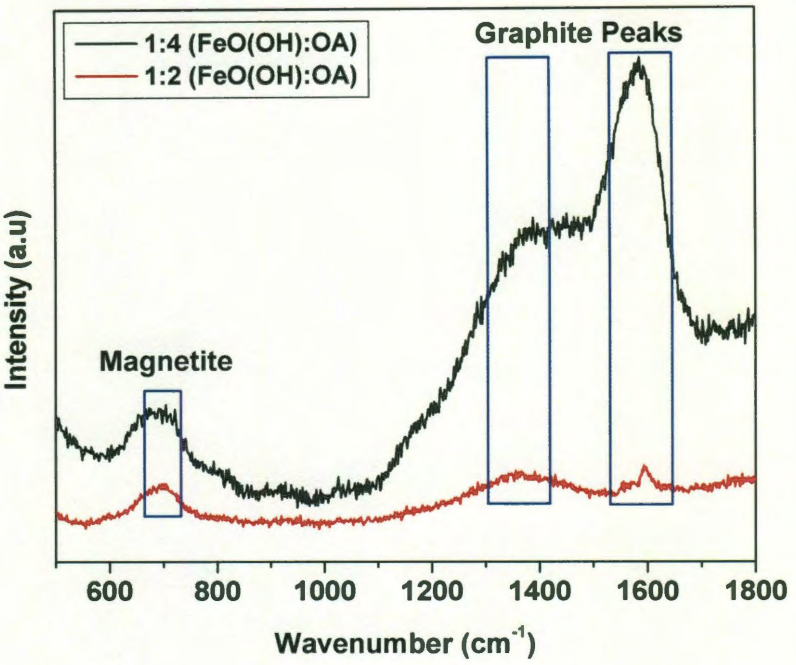

Figure 1.20: Raman spectra of iron oxide nanoparticles obtained using different molar ratio of reactants.

Raman spectra of the aforementioned samples clearly shows almost negligible amount of graphite when less oleic acid is used (red) as opposed to strong graphite peak in 1:4 (FeO(OH):OA) sample with magnetite reference peak present in both cases, proving that oleic acid decomposition is responsible for the formation of graphite layer (Figure 1.20).

1.3.7 Applications

Different sized nanoparticles can be obtained by changing time and temperature for growth without changing molar ratio of reactants. With the knowledge of carbon coating occurring at 320°C in mind, we were able to synthesize bigger sized particles

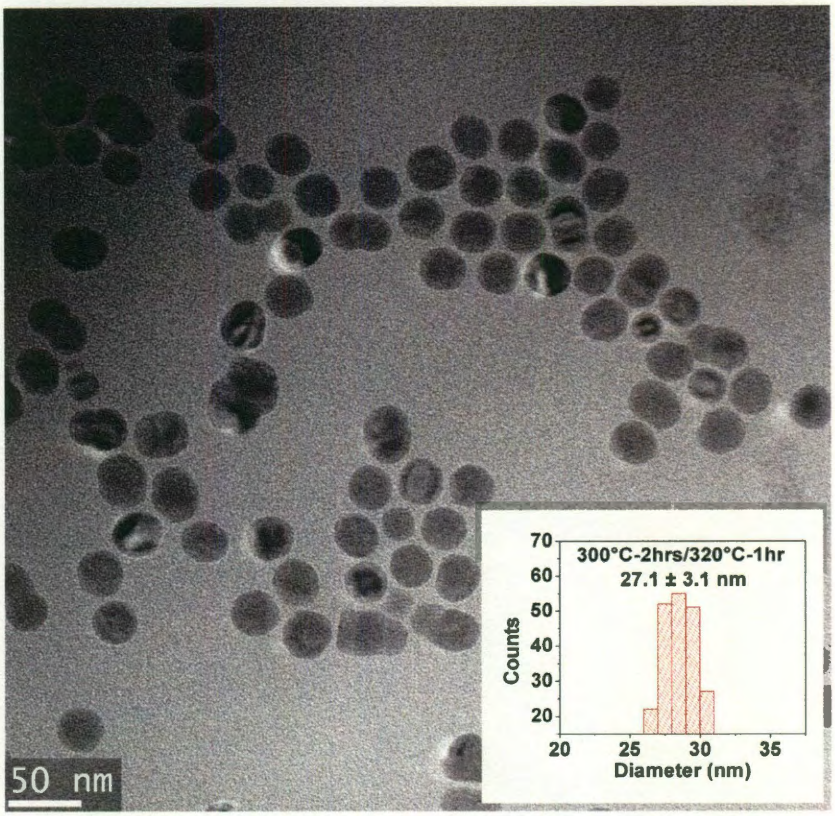

Figure 1.21: TEM images showing the formation of bigger sized particles with uniform size distribution, obtained by varying the synthesis time below 320°C.

without varying the molar ratio of the reactants, but allowing longer duration for particle growth prior to size focusing. 27 nm sized monodisperse particles were obtained by maintaining the temperature at 300°C for 2hrs followed by 1hr at 320°C (Figure 1.21). This methodology can be applied to make much bigger particles in future.

Sample	As added (ppm)	As adsorbed (ppm)	% As removed
1hr/320°C	20.5	14.7	72
7hrs/320°c	20.5	0	0

Table 1.3: Arsenic adsorption data of iron oxide nanoparticles with varying amounts of graphite on the surface. 1hr sample shows very high sorption efficiency as compared to no As removal for 7hrs sample.

Amount of graphite present on the iron oxide nanoparticle surface affects the chemical activity, such as arsenic adsorption. One of the major applications of iron oxide nanocrystals is water remediation to remove pollutants such as arsenic.[2] Arsenic sorption was carried out on 1hr and 7hrs powder sample. As seen in Table 1.3, 1hr sample is highly effective in arsenic removal (72%) whereas 7hrs sample does not remove any arsenic. It can be qualitatively said that graphite coating on 7hrs sample, being thicker is blocking any As adsorption with iron oxide surface.

As another aspect for future study, thicker coating can be used as a substrate to grow carbon nanotubes. This mechanism for preserving the monodipsersity can be explored in the synthesis of other metal oxides such as ceria and manganese dioxide. Fatty acids with different degree of unsaturation and chain lengths can be studied to better understand their contribution to the size distribution and stabilization of nanoparticles.

1.4 CONCLUSIONS

Oleic acid decomposition has been shown to play a key role in the quality of iron oxide nanoparticles obtained. Evolution of carbon monoxide due to the breakdown of the fatty acid leads to the formation of graphite on iron oxide nanoparticles that preserves monodispersity. Graphite presence was confirmed by different methods such as Raman spectroscopy and Fourier transform infrared spectroscopy. The mechanism of graphite formation was studied using gas chromatography – mass spectrometry. Disproporationation of carbon monoxide peaked at 30min at 320°C as observed from the ratio of carbon monoxide to carbon dioxide evolved. This result was corroborated by the size focusing observed to happen around the same time in corresponding transmission electron micrographs. Thermo-gravimetric analysis and energy dispersive spectrometry was used to quantify graphite on the surface of iron oxide nanoparticles. The amount of carbon coating increases with time at higher temperatures and its presence affects the surface activity of iron oxide nanocrystals. With this knowledge, one can obtain different sized particles and tailor their properties for specific applications.

1.5 METHODS AND MATERIALS

1.5.1 Synthesis of iron oxide nanoparticles

Iron oxy-hydrate (FeO(OH) iron(III) oxide, hydrated; catalyst grade, 30-50 mesh), 1-octadecene (ODE 90%), oleic acid (90%), super hydride (lithium triethyl borohydride, 1M solution in THF) and nitric acid (trace metal grade) were purchased from Sigma-Aldrich. 0.2µm NYL syringe filter was obtained from WHATMAN.

Iron oxide nanoparticles were obtained by thermal decomposition of iron carboxylate salts.[10] In a typical run 0.176g of FeO(OH), 2.24g of oleic acid and 8g of 1-octadecene were heated in a 50mL three-neck flask with stirring under Argon. The mixture was heated to 120°C and held for 1hr for removal of any water, followed by heating to 270°C for 30min in order to facilitate precursor formation (pyrolysis) and nucleation. The temperature was then raised and held at 320°C for different durations of time (1hr/7hrs) for particle growth and annealing. The resulting mixture contained brown-black iron oxide nanocrystals that were stabilized by oleic acid and was soluble in organic solvents such as hexane.[10]

The iron oxide nanocrystals were purified by repeated cycles of precipitation and sedimentation followed by dispersion in hexane. Reaction products were treated with a 1:1 volumetric amount of acetone and methanol leading to the formation of visible aggregates; these were collected *via* centrifugation in a pellet and could be dispersed back into hexanes. This procedure was repeated five times to remove unreacted iron salts, octadecene or unbound oleic acid. Purified nanocrystal solutions in hexanes were

digested by strong nitric acid and analyzed for their iron content with atomic emission spectroscopy (ICP-OES). Using the average diameter of the material obtained from TEM and the density of iron oxide (5.17 g/cm^3), the atomic concentration of iron was converted into a nanoparticle concentration. Nanocrystals were phase transferred into water using an oleic acid bilayer methodology.[1]

To obtain powder samples of nanoparticles devoid of surface coating, 5mL of purified nanocrystals were centrifuged and the precipitate was subjected to strong reduction using 5mL of super hydride with stirring under argon.[56] Super hydride reduces carboxylic moieties to alcohols, thereby cleaving the organometallic bond between the iron oxide surface and oleic acid.[57] Methanol was then added to this solution followed by sonication and centrifugation for further precipitation. The whole procedure was repeated three times. Hexanes were then added to the pellet and sonicated to dissolve any remaining organics. One more step of centrifugation resulted in a dry powder of iron oxide nanoparticles.

The arsenic adsorption experiment was performed by adding the dried iron oxide samples to 12 ppm As solutions (1 g Fe_3O_4/L) that were pH adjusted to a value of 12. These samples were run in triplicate. The control was prepared without iron oxide nanoparticles. All samples were then bath sonicated for 1 hr to disrupt aggregates. The samples were then immediately (before settling occurs) placed in a tumbler to rotate end over end at 4 rpm for 70 hrs. All samples were then filtered, and the filtrate was acidified to 1% nitric acid. The samples were then analyzed for Arsenic *via* ICP-OES. The

extent of adsorption was then calculated by subtracting the arsenic in the filtrate from the 12 ppm arsenic control sample.

1.5.2 Characterization of nanocrystals

High Resolution transmission electron microscopy (TEM) was carried out using JEOL 2100 field emission gun TEM at 200kV with a single tilt holder using 400 mesh ultra-thin carbon type-A copper grids from Ted Pella Inc. More than 1000 particles were measured to capture both the mean size and size distribution of the particles using ImagePro software. Thermo-gravitmetric Analysis (TGA) was carried out using TA INSTRUMENTS SDT Q-600 instrument with sample deposited in a platinum pan. Samples were maintained at 200°C for 5hrs for removal of any associated solvent/moisture before further heating. The samples were then heated to 700°C at the rate of 50°C/min under air. All sizing data with respective significant figures was reported with error bars representing their standard deviation. Inductively coupled plasma (ICP) analysis was carried out using PERKIN ELMER® ICP-OES instrument equipped with auto-sampler.

Raman Spectroscopy was done on a Renishaw inVia Raman Microscope using a 514 nm laser with an 1800 lines/mm filter. Powder samples were placed onto a glass slide for measurement. Spectra were collected using a 20x lens with the laser set at 100% power for 60 seconds and averaged over 5 scans. Fourier transform infrared spectroscopy (FTIR) was recorded on a ThermoScientific Nexus 670 FTIR spectrometer. Iron oxide samples in hexanes were dropped and dried on a CaF_2 disc. Gas chromatography-mass spectrometry (GC-MS) was carried out using Agilent 7898A GC with 5975 inert XL mass

spectrometer. 10μL of gas sample was directly injected and analyzed through an Agilent GS-GASPRO column for 5min. Abundance values obtained from GC-MS were calibrated using ultra-high purity carbon dioxide and carbon monoxide gases (Tri-Matheson Gas).

X-ray Photoelectron Spectroscopy was carried out on a PHI Quantera XPS using a substrate of indium foil at 140 eV (low resolution) for survey scans and 26 eV (high resolution) for elemental scans. 1hr and 7hrs powder sample devoid of oleic acid were analyzed. All scans utilized electron and ion neutralizers. Using PHI Multipak 7.0, the spectrum was corrected using the adventitious carbon peak at 284.5 eV.

For CO_2 calibration, a crimped 10mL gas-tight headspace vial (National Scientific) was purged with argon for 5min while maintaining a positive pressure. Similar procedure was carried out to fill a vial with carbon dioxide. 0.5mL of CO_2 was drawn and injected into the argon purged vial to prepare a standard. Similarly, standards with different concentrations were prepared and calibrated. CO was calibrated using CO_2 as the reference gas. Gas concentrations were calculated by considering Ar and CO_2 purged vials to be at 1atm pressure, followed by the mass computation of the respective gases.

CHAPTER 2

Bilayers as phase transfer agents for nanocrystals prepared in non-polar solvents

2.1 ABSTRACT

The effective water dispersion of highly uniform nanoparticles synthesized in organic solvents is a major issue for their broad applications. In an effort to overcome this problem, iron oxide and cadmium selenide nanocrystals were surrounded by lipid bilayers to create stable, aqueous dispersions. The core inorganic particles were originally generated in oleic acid and 1-octadecene. When these organic solutions were mixed with water and a sparing amount of excess fatty acid, up to 70% of the nanoparticles transferred into the aqueous phase. This simple approach was applied to two different nanocrystal types, and nanocrystal diameters ranging from 5 to 15 nm. In all cases, the resulting materials were stable, non-aggregated suspensions that retained their original magnetic and optical properties. The phase transfer efficiency is maximum when very little oleic acid is added (*e.g.* 0.2 w/w %). At higher concentrations, above the critical micelle concentration, the formation of micelles begins to compete with bilayer generation leading to less effective phase transfer. Unlike other approaches for water dispersion that rely on amphiphiles with significant water solubility, the fatty acids used in this work are only sparingly soluble in water. As a result, there is minimal dynamic exchange between free and bound surface agents and the resulting aqueous solutions contain little residual free organic carbon. Thermo-gravimetric analysis (TGA) confirmed the presence of bilayers around the nanocrystal cores. The particle size, size distribution, process yield and colloidal stability were found using a suite of methods including Transmission Electron Microscopy (TEM), Small Angle X-ray Scattering (SAXS), Dynamic Light Scattering (DLS), Inductively Coupled Plasma – Optical Emission

Spectroscopy (ICP-OES) and Ultraviolet-visible Spectroscopy (UV-vis). Bilayer-nanocrystal complexes possess many of the same size-dependent features as the original materials, and as such offer new avenues for exploring and exploiting the interface between nanocrystals and biology.

Note: The iron-oxide nanoparticles used throughout this chapter corresponds to the 1h sample explained in Chapter 1 with sub-monolayer carbon coating on the surface.

2.2 INTRODUCTION

2.2.1 Significance of phase transfer

The phase transfer of nanoparticles from non-polar to polar suspensions remains an outstanding challenge for material chemists. The best quality nanocrystals, with respect to uniformity, size control and crystallinity, are generally formed in organic solutions at elevated temperatures.[10,14,15,58,59] These synthetic methods produce nanomaterials as diverse as gold, cadmium selenide and iron oxide which as a consequence of their formation conditions possess surfaces that terminate in organic, non-polar moieties. However, to apply the unique optical and magnetic properties of these nanocrystals often requires surface modifications that yield well dispersed and non-aggregated materials stable in water.[60-63] Nanoscale iron oxides, for example, in water purification as well as magnetic resonance imaging must be used in aqueous solutions.[2,5,62] Quantum dots find enormous application as biological imaging agents, a technology that requires compact and isolated particles whose surfaces are compatible with a variety of biological fluids.[64-66] These and other uses for nanocrystals have sustained interest in this topic for nearly a decade; researchers have focused on methods that are both efficient in their transfer of nanocrystals and capable of preventing material aggregation and dissolution.[12,14,67-71]

2.2.2 Methods in literature

Many of the existing strategies for nanocrystal phase transfer use lipids as essential components of amphiphilic surface coatings.[14,61,72] One commercial quantum dot

material reports the use of a proprietary PEG-lipid to create a stable and water soluble material.[73] In these examples, the lipids – typically fatty acids – function as the non-polar constituent of larger amphiphiles (*e.g.* surfactants). Their hydrophobic tail interacts with the nanocrystal's non-polar organic surface, and leads to a full encapsulation of the core and its original coating. The hydrophilic end of the amphiphile is thus left to stabilize the new surface and renders the material polar and fully dispersed in water. This encapsulation approach ensures that the nanoparticle surfaces are never stripped of their original organic coatings. As a result, particle aggregation is minimized due to the presence of steric stabilization during the entire phase transfer process. Also, in the case of quantum dots encapsulation is strongly preferred as it prevents degradation of the desirable optical properties.[14,74] Nanocrystal encapsulation can be problematic in some circumstances as the size of the resulting core and surface treatment can be much larger than the starting organic material; moreover, it often requires expensive or customized co-polymers and surfactants.[63,71] Still there are good examples of phase transfer strategies that can produce non-aggregated and stable nanocrystal dispersions in water.[67-71,75] These efforts include encapsulation using polymers (*e.g* poly-acrylic acid, poly-ethylene glycol) and ligand exchange using moieties such as bifunctional thiols.[76,77]

2.2.3 Requirements and motivation for phase transfer

Whatever the surface agent selected to affect a phase transfer, it is generally desirable that the resulting nanocrystal suspensions contain little free surfactant or other organic species. Such a criterion is particularly important for biomedical and toxicological

studies.[78-80] Conventional practice relies on sedimentation or filtration to concentrate and purify nanoparticles. These treatments can be intrinsically limited if nanocrystal surface coatings are themselves soluble in water. Unless cross-linked or otherwise irreversibly attached to the nanoparticle, most surface-bound amphiphiles will exist in equilibrium with their free form.[81] As a result, coatings can be removed if nanocrystals are repeatedly washed or diluted. Moreover, the dynamic exchange of the encapsulating agents can result in an adventitious adsorption of other materials, yielding a nanocrystal interface quite different from the one originally engineered.[82] Perhaps the most significant consequence of labile surface coatings is that nanocrystal suspensions must necessarily contain some quantity of the soluble, free surfactant.

These issues motivated our interest in an alternative approach to nanoparticle phase transfer. Our goal was to form small, stable, and non-aggregated nanocrystals in water whose size-dependent properties were preserved; however, we wanted to achieve these features by using a surface coating that in its pure form would have extremely low water solubility. To achieve this end, we use a phase transfer process that generates a fatty acid bilayer at the nanoparticle interface (Figure 2.1B). The term 'bilayer' in this work is directed towards lipid bilayers, where both the layers are made up of the same moiety. We selected a fatty acid, oleic acid, whose monomer is highly insoluble in water. However, in its bilayer form it presents a stable and polar interface well suited for a variety of physiological environments. Our methods were inspired by efforts to sterically stabilize iron oxide colloids. For colloids formed in water, phase transfer due to bilayer formation is not the goal as it is in this work. Instead, bilayers are used to

slow or reverse colloidal particle aggregation; many water soluble amphiphiles have been demonstrated for this purpose including SDBS[83], dodecanoic acid[84], alkanoic acids[61,72], phospholipids[85] and PLURONIC® block copolymers.[86] This literature provides an important conceptual foundation for this effort and offers highly relevant examples of bilayer-nanoparticle characterization.

Here we show the results of a versatile and simple approach to the generation of bilayer stabilized nanocrystals, entities that we term 'bilayer-nanocrystal complexes'. While most of the examples provided in this effort center on iron oxide nanocrystals, we also have explored the stabilization of quantum dots as illustrated in our study of phase transfer efficiency. The resulting materials possess small hydrodynamic sizes and are stable under a wide range of physiological conditions. SAXS indicates that in contrast to systems stabilized by non-ionic surfactants, bilayer-nanocrystal complexes are non-aggregated in water. Little free fatty acid or other organic carbon is measurable in the nanocrystal aqueous suspensions, a result anticipated given the low aqueous solubility of free oleic acid. Bilayer nanocrystal complexes retain their size dependent physical properties in water.

2.3 RESULTS AND DISCUSSION

2.3.1 Scheme of the process

This work focuses on a relatively unexplored avenue for creating stable aqueous suspensions of nanocrystals from organic solutions: namely, the generation of fatty acid bilayers around the original hydrophobic particles. Figure 2.1B illustrates the process studied in this work and contrasts it to the more conventional use of non-ionic surfactants (Figure 2.1A) to affect nanocrystal phase transfer. Both methods use amphiphiles to change the interfacial chemistry of particles from non-polar to polar. The standard approach relies on the hydrophobic blocks of amphiphilic polymers or surfactants to wrap the non-polar surfaces of particles or groups of particles. Of interest here is the application of molecular fatty acids, identical to those already present at quantum dot and iron oxide interfaces, as phase transfer agents. In the non-polar nanocrystal solutions these fatty acids form dense and compact coatings with the hydrocarbon tail oriented towards the solution phase. We reasoned that if slightly more fatty acid is added, and the systems appropriately mixed, a second layer of fatty acid could be laid down on top of the original one. The process would result in the formation of a bilayer-nanocrystal complex that would present polar groups at the particle interface and subsequently lead to particle dispersion in water.

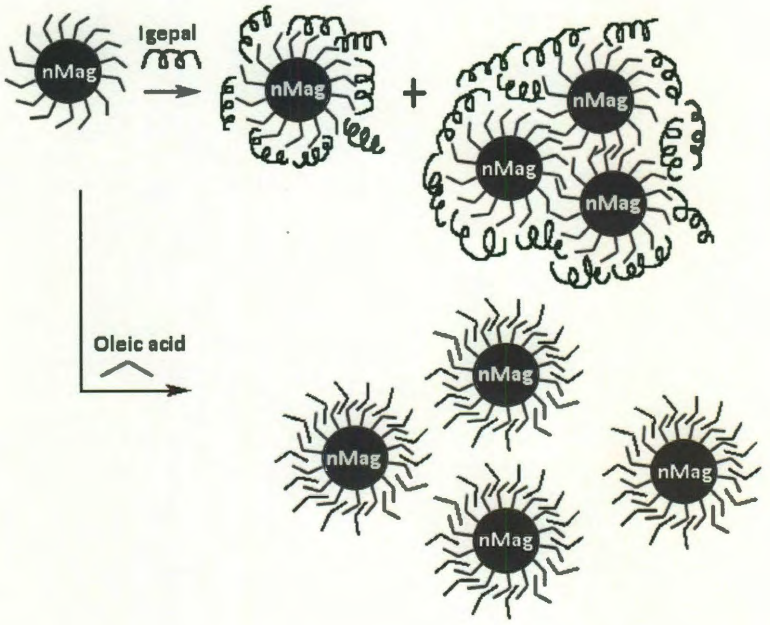

Figure 2.1: Illustration of the aqueous transfer of iron oxide nanoparticles (nMag) *via* both (A) addition of IGEPAL® CO 630 surfactant; non-ionic surfactants can result in the formation of clusters of nanoparticles in the final aqueous suspensions (B) bilayer formation.

To explore this approach, oleic acid – a C18 unsaturated fatty acid – was added as a phase transfer agent to an oil/water mixture of iron oxide or cadmium selenide nanocrystals. The choice of oleic acid was motivated by several factors: its hydrophobic tail is long enough to interact with existing hydrophobic coatings; it has poor micelle forming ability due to the presence of a double bond; and finally it is a simple choice as oleic acid is the native fatty acid used in the nanocrystal synthesis.[72] Under the appropriate mixing conditions, for example probe sonication, the colored nanocrystals could be transferred from the organic to aqueous layers with high (>70%) efficiency. Several characterization methods were then applied to confirm that the surfaces of the

nanoparticles in water were covered in bilayers; among these thermo-gravimetric analysis (TGA) is the most conclusive for these structures.

2.3.2 Proof of bilayer presence

During controlled heating of sample residues, two distinct weight loss peaks can be observed. These correlate well in temperature to those reported for fatty acid double layers in a variety of environments (Figure 2.2).[61] The mass loss between 400 to 500°C corresponds to the desorption of the outer layer of oleic acid; as expected, it occurs at a temperature slightly higher than the boiling point of neat oleic acid or 360°C at 760mm Hg.[87] A second inflection point occurs between 650 and 800°C. This feature arises from the loss of more tightly bound oleic acid. This inner layer of oleic acid is thought to be stabilized *via* a complex between iron (II) and the carboxylate groups of oleic acid.[61,63] As a result, it can only be removed from the surface at higher temperatures. Also, we note that the weight loss difference between the outer and inner layers can be semi-quantitatively attributed to the higher curvature of the smaller 10 nm particle in comparison with the bigger 17 nm particle. The coincidence of the TGA peak temperatures in these samples with that reported previously for bilayers, both on surfaces and colloids, is strong evidence that under our process conditions the materials are stabilized by oleic acid bilayers.[88] In the case of iron oxide nanoparticles the bilayer forms in those regions where the oleate carbon chains from the particle surface extend outward. As explained in Chapter 1, only about 40% of the particle surface is coated with carbon whereas the rest is stabilized by oleic acid.

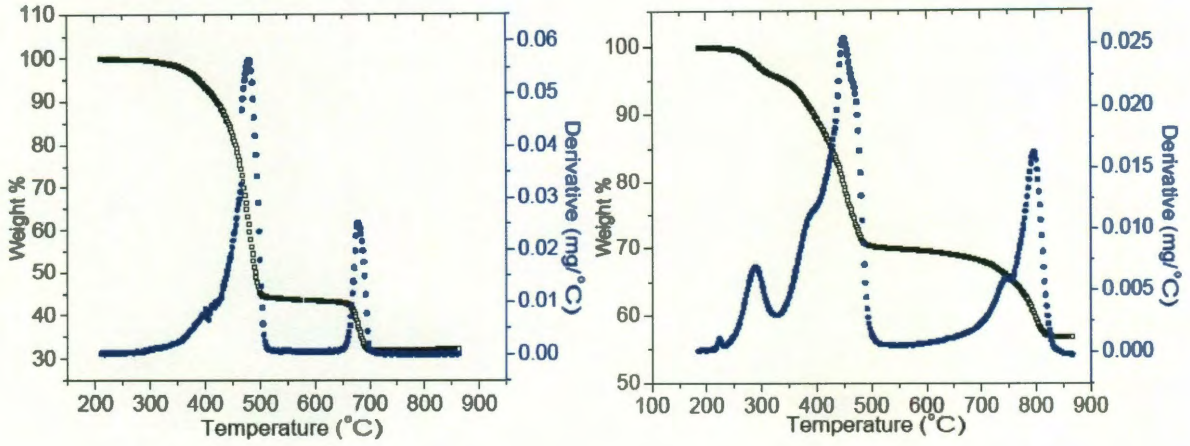

Figure 2.2: Thermo-gravimetric analysis (TGA) curves for 10 nm (left) and 17 nm (right) iron oxide nanocrystals. The black dots indicate the percent weight as a function of temperature and the weight loss derivative is indicated in blue. In both the cases, sample mass remained constant while cooling from 900°C to 50°C.

2.3.3 Variation of phase transfer yield

The formation of bilayers around the nanocrystal surfaces is also consistent with the strong sensitivity of process yield to fatty acid concentration (Figure 2.3). A striking feature of these data is the extremely low quantities of fatty acid required to obtain high phase transfer yields (Figure 2.3). For both quantum dots and iron oxide nanocrystals, over 70% of the material is transferred from hexanes to water after the addition of only 0.2 w/w% oleic acid. This is in stark contrast to particle stabilization with IGEPAL® CO 630 which requires more than 10 w/w% for reasonable phase transfer yields.[2] This observation is likely due to the competition between oleic acid micelle and bilayer formation. At or near its critical micelle concentration (CMC), oleic acid can form micelles in water and this process would remove bilayer material from the surface and reduce the solubility in water.[89,90] The outer layer on the particle surface as well as the micelles would be constituted by a varying mixture of oleic acid and oleate ions depending on the pH of the solution. As a result, the optimal phase transfer efficiency is

obtained near the CMC for oleic acid. This observation may explain why reports of bilayer phase transfer methods for highly uniform nanocrystals are limited: conventional practice involves the addition of a vast excess of phase transfer agent to a suspension in order to ensure an efficient process. As apparent in Figure 2.3, such an approach would depress the transfer efficiencies substantially. In general, if bilayer formation is desired it is best to work with fatty acid concentrations (0.7 to 3.5mM for oleic acid) that are at or below the critical micelle concentration.[90] At their highest transfer yields, the molar ratio of oleic acid to nanoparticles was found to be 90 for 10 nm iron oxide and 17 for 4 nm quantum dots. This observation between the two nanoparticle systems could be attributed to the order of magnitude difference in their surface areas.

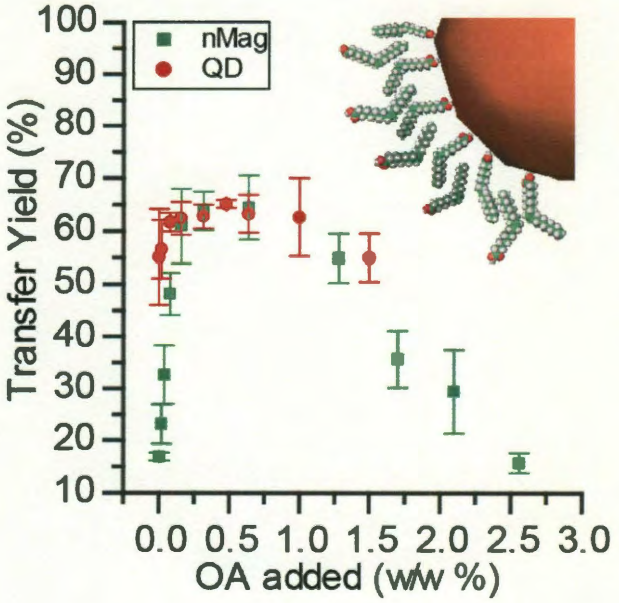

Figure 2.3: Variation of the transfer yield of iron oxide (nMAG) nanoparticles and quantum dots (QD) from hexanes into water as a function of oleic acid (OA) concentration. Inset: Scale depiction of a 10 nm diameter nanocrystal coated with a bilayer. Iron oxide concentration was obtained by ICP analysis and quantum dot concentration was obtained *via* absorbance.

Also notable in Figure 2.3 is the similarity between the process yield for both quantum dots and iron oxide nanocrystals. Not only is the core composition different in these two cases, but the core diameters are also very different (*e.g.* 4 nm diameter as opposed to 10 nm diameter). Still the behavior and optimization is comparable suggesting that as long as particles possess a hydrophobic surface, the addition of small amounts of fatty acid may be suitable for creating water stable dispersions.

The total organic carbon (TOC) found free in solution for the oleic acid stabilized nanoparticles is just 9 ppm - three orders of magnitude less than that found for equivalent non-ionic surfactant encapsulated (IGEPAL® CO 630) materials. This observation can be explained by the different solubilities of oleic acid versus conventional phase transfer agents. Large amounts of non-ionic surfactants like IGEPAL® are required to affect nanoparticle phase separation because these materials alone have high solubility in water. An excess of free non-ionic surfactant in the aqueous suspensions ensures a complete and stable surface coating. In contrast, oleic acid is virtually insoluble in water (HLB value of 1) and once incorporated into a bilayer structure will not appreciably desorb from the surface.[84] The price paid for an insoluble surface stabilizing agent is the challenge associated with combining the original hydrophobic nanoparticles, free oleic acids, and water. Here we overcome this kinetic barrier by using a brief ultrasonication process which quickly mixes the various components and results in stable aqueous suspensions. While our phase transfer yields are quite high – on the order of 70% - they are not 100% effective and this is likely due to the challenges of mixing the disparate starting materials (Figure 2.3). We note that it

may also be possible to replace ultrasonication with elevated temperatures for more polar fatty acids and their salts.[61]

2.3.4 Behavior of suspension

An important concern for applications of nanocrystals in water is that the phase transfer process should preserve the original quality of the material as well as prevent particle aggregation. The first issue is of particular concern in this process as it relies on probe sonication to ensure adequate mixing of the insoluble fatty acids, nanocrystals and water. The preparation of nanocrystals in organic media affords a great deal of control over nanocrystal nucleation and growth, and as a result the as-synthesized nanocrystals possess symmetric shapes, narrow size distributions, and high crystallinity (Figure 2.4A). These desirable features remain unchanged after the phase transfer process (Figure 2.4B). Most notably, each particle is well separated from its neighbors in the microscopy images, suggesting that an organic coating is associated with individual particles. Particle aggregation is not prevalent in the dried films. This observation is supported by the high clarity of the suspensions and their apparent lack of sedimentation over months (insets Figure 2.4).

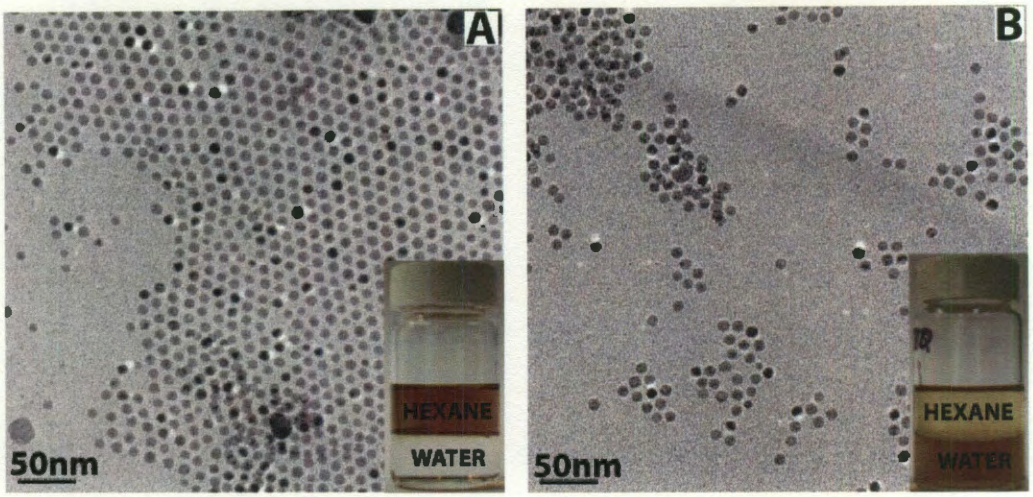

Figure 2.4: Transmission electron micrographs of iron oxide nanoparticles A) in organics (9.6 ± 1.0 nm), B) phase transferred into water *via* bilayer formation (10 ± 1 nm). Inset pictures show phase separated mixtures with water phase at the bottom and hexane phase at the top. As is clear the phase transfer efficiency is on the order of 70% as some color remains in the organic phase. More than 1000 particles were measured to capture both the average size and the size distribution.

Direct evidence that bilayer-nanocrystal complexes are not aggregated is found in an analysis of their small angle X-ray scattering (SAXS) profiles. This method is sensitive to the presence of aggregates from two to ten particles across, and complements well the visual observations and microscopic analysis in Figure 2.4.[91] Figures 2.5A and 2.5B present the SAXS profiles for bilayer coated iron oxide nanocrystals of 10 and 17 nm core diameters in water. The inverted scattering minima at low angles are very sensitive to the particle size distribution, and their appearance in the raw data confirm the finding from TEM that these are highly uniform samples. Models for X-ray scattering of small particles can be fit to these data to obtain more quantitative information, and these take as inputs the density, expected size and size distribution of the particles.[92] The best fits to the scattering data are shown as solid lines and the resulting overall size

distributions are shown in the figure inset. As expected, the larger core sizes lead to greater diameters; moreover, the average sizes are representative of non-aggregated and fully isolated nanoparticles. These basic conclusions were confirmed by dynamic light scattering data (Table 2.1) which provides a semi-quantitative measurement of the average hydrodynamic diameter of nanocrystals directly in suspension.

The hydrodynamic diameters of these materials are in good agreement with what is expected for an inorganic core surrounded by a fatty acid bilayer (Table 2.1). In this analysis, dimensions found from multiple characterization methods were compared to extract the effective thickness of the bilayers. TEM provides the inorganic core diameter; SAXS analysis provides a measure of the extent of the core and the dense organic coatings; and finally, DLS data reports the full hydrodynamic diameter of the bilayer-nanocrystal complex and associated hydration shell. The diameters obtained *via* SAXS and DLS for bilayer-nanocrystal complexes (Sample A and Sample B) are larger than the inorganic core as expected; the 4.6 nanometer difference (average of Samples A and B shell size) between the inorganic cores and the bilayer-nanoparticle complex can be attributed to the oleic acid bilayer. This corresponds to a surface coating thickness of about 2.3 nm which is comparable to the thickness of C-18 chain bilayers measured in other similar systems.[93] Both in these systems, as well in other oleic acid bilayers, there is a large degree of interpenetration of the C-18 chains - a feature depicted schematically in Figure 2.3.[61] Sample B corresponds to 17 nm core iron oxide particles coated with oleic acid bilayer. Similar bilayer dimensions were obtained *via* SAXS and DLS for this case and these are consistent with that of the smaller sample A.

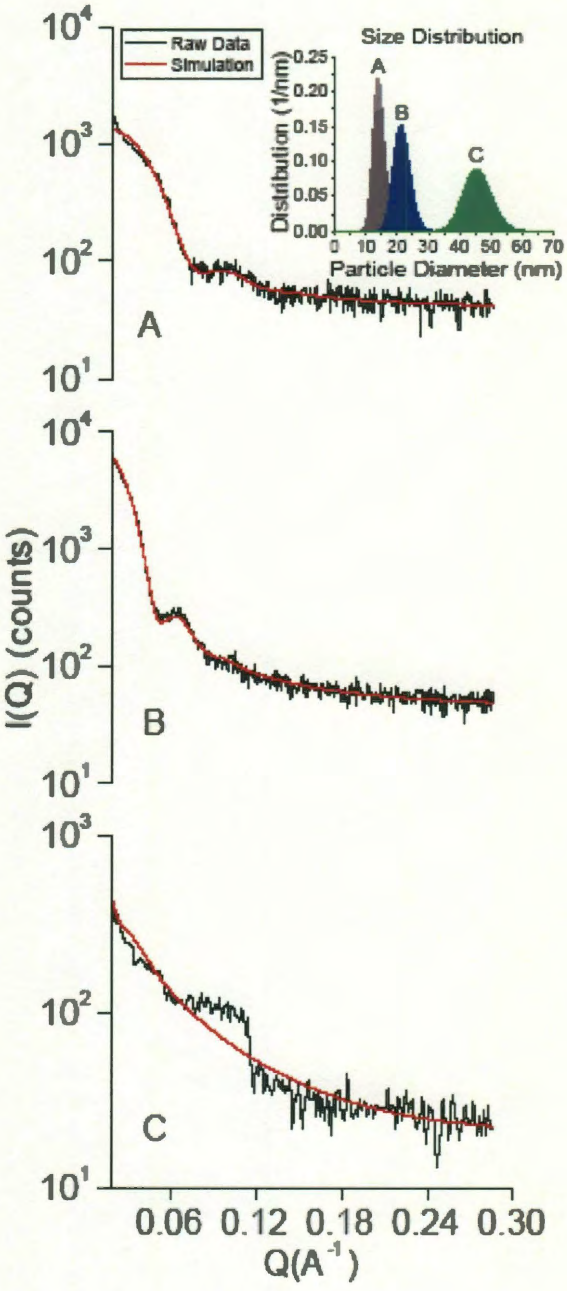

Figure 2.5: Small angle X-ray scattering profiles (in black) with simulated fits (in red) for iron oxide nanoparticles in water: A) 10 nm core (bilayer coated), B) 17 nm core (bilayer coated), C) 10 nm core (IGEPAL coated). Inset: corresponding size distributions.

Sample	A (nm)	B (nm)	C(nm)
TEM (core)	10.0 ± 1.2	16.6 ± 2.3	10.0 ± 1.2
SAXS (core+shell)	14.3 ± 1.8	21.5 ± 2.6	49.0 ± 4.8
DLS(hydrodynamic)	14.2 ± 2.6	26.3 ± 4.1	154.1 ± 15.6

Table 2.1: Diameters of iron oxide nanoparticles dispersed in water obtained by TEM(particle core), SAXS(particle core + shell) and DLS (hydrodynamic) for particles of size : A) 10 nm; bilayer coated, B) 17 nm; bilayer coated and C) 10 nm; IGEPAL coated.

An important feature of bilayer-nanocrystal complexes highlighted by Table 2.1 is that they form compact structures in aqueous suspensions. Typically, the bilayer-nanocrystal complexes are only 4.6 nm larger than the core nanocrystal. Quantum dots stabilized by amphiphilic surfactants, for example, can possess hydrodynamic diameters nearly five to ten times larger than their core diameter.[75,94,95]

2.3.5 Variation of pH, ionic strength and temperature

Bilayers produced *via* oleic acid have remarkable chemical and thermal stability. The formation of a bilayer on the nanocrystal surface leads to a pH dependent charge stabilization confirmed by Zeta potential measurements (-55mV on account of oleate ions at a pH of 6.0). Figure 2.6 shows the visual appearance of bilayer-nanocrystal complex suspensions under different conditions of pH, ionic strength and temperature. As expected for these systems, in acidic conditions the surface groups are protonated; above the pKa of oleic acid (≈5.0), however, the nanocrystals are quite stable.[96] The addition of salts to these suspensions can result in the precipitation of nanocrystal aggregates; the middle panel of Figure 2.6 illustrates that above 250 mM the electrostatic repulsion is effectively shielded and interparticle aggregation becomes substantial. DLS confirms these visual observations. While the materials are somewhat

sensitive to both charge and pH, they are remarkably stable over a variety of temperatures (bottom, Figure 2.6).

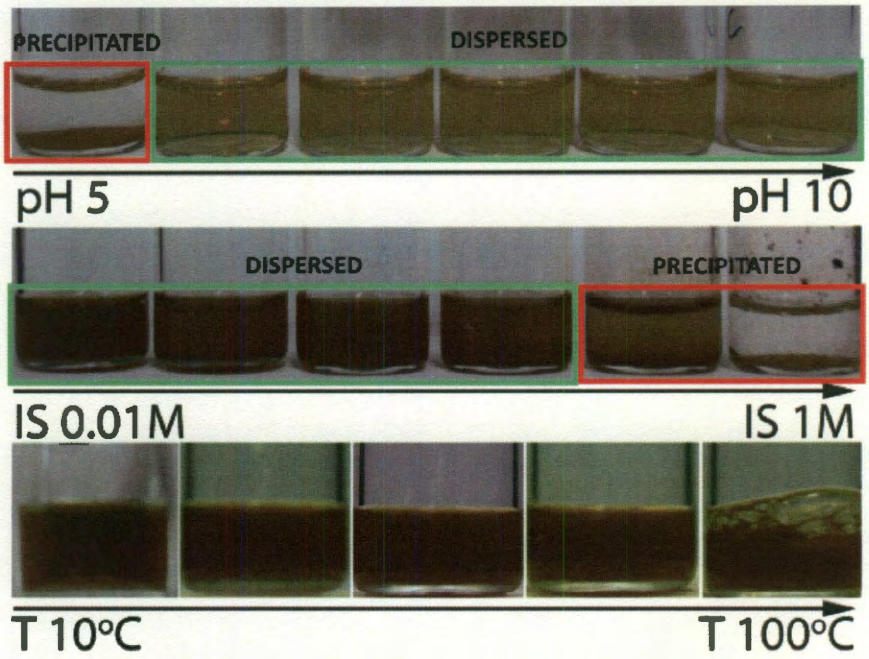

Figure 2.6: Iron oxide nanocrystal suspensions (10 nm core size) under varying solution phase conditions. Particles that were visibly sedimented or cloudy are surrounded by a red box; solutions with unchanged visual appearance are surrounded in green. These charge stabilized materials become unstable at low pH, when the fatty acid coatings are protonated (top panel) as well as at high ionic strengths in NaCl (middle panel). Temperature has remarkably little effect on the systems.

2.3.6 Applications to different classes of nanocrystals

A delineation of the unique and valuable optical and magnetic properties of nanocrystals has been the subject of extensive prior work.[2,14,66,97] Here, we simply confirm that the important physical properties of both of these model systems remain unchanged after transfer into water (Figure 2.7). Nanocrystalline iron oxide phase transferred into water can be captured by an external magnetic field; the time for capture and the overall efficiency of the process is unchanged as would be expected

given the physical characterization of the materials (Figure 2.4). Figure 2.7 also illustrates that the optical properties of quantum dots before and after bilayer stabilization are relatively unchanged. Most importantly, the quantum yield for these quantum dots systems remains within 20% of its original value after phase transfer. Complete analysis of the optical and magnetic properties of these complexes is the subject of future work. This data is presented here only to establish that the process does not significantly alter the core nanocrystal features.

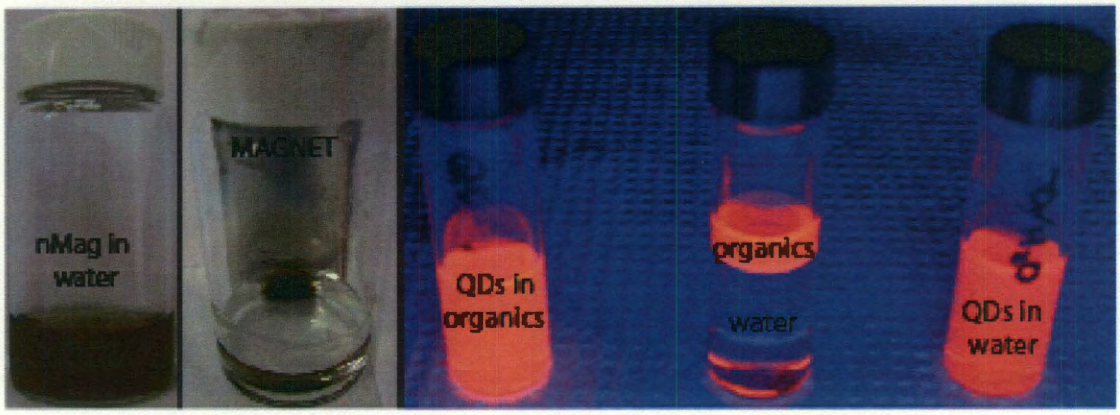

Figure 2.7. Optical and magnetic properties of bilayer-nanocrystal complexes are similar to the original materials. On the far left panels, a strong permanent magnet is able to concentrate the iron oxide materials (nMAG) much as is observed in hexanes. On the right panel, the fluorescence of quantum dots (QD) is relatively unchanged after the formation of a bilayer and the transfer of the material into water.

Finally, in order to identify the advantages of a bilayer stabilization approach we compare these results to those found using a conventional non-ionic surfactant, IGEPAL® CO 630. Figure 2.5C shows that these surfactants when applied to iron oxide nanocrystals result in particle flocculation; larger amphiphilic phase transfer agents have been reported to encapsulate multiple particles.[71,88] This results in polydisperse

groupings of iron oxide nanocrystals. Also, corresponding DLS diameters (Table 2.1: sample C) show a significant increase over the particle core size, indicating the presence of either aggregates or flocs in IGEPAL stabilized materials. These observations highlight the significant challenges faced in preventing aggregation of these magnetic materials during phase transfer. The approach outlined in this paper, in contrast, is successful in generating isolated magnetic nanocrystals as well as quantum dots.

2.4 CONCLUSIONS

Lipid bilayers prepared from a water insoluble fatty acid can be generated around both iron oxide and cadmium selenide nanocrystals. These surface coatings form around nanoparticles after mixing hexane solutions of the materials, free fatty acids and water; thermogravimetric analysis confirms the existence of lipid bilayers. The bilayer thickness on a variety of nanocrystal cores was deduced from both dynamic light scattering and small angle X-ray scattering; typical values of 2.2-2.5 nanometer are consistent with those reported for comparable immobilized bilayers. An interesting finding is that bilayer formation is only successful when a small amount (0.2 w/w %) of oleic acid is incorporated into the organic solutions. Phase transfer efficiencies may be depressed at higher concentrations due to the self-association of the fatty acids into micelles. An important advantage of using a highly insoluble fatty acid to affect nanocrystal phase transfer is the resulting purity of the aqueous suspension: once captured into a lipid bilayer around a nanoparticle, there is no driving force for the desorption of free fatty acid. Small angle X-ray scattering of the aqueous suspensions reveals that the materials are uniform and non-aggregated. The resulting bilayer-nanoparticle complexes are highly stable over a wide range of temperatures, ionic strength and pH as expected for a moderately charged interface. Bilayer formation does not change the essential size-dependent properties of nanocrystals and offers several advantages over conventional encapsulation strategies.

2.5 METHODS AND MATERIALS

2.5.1 Nanocrystal synthesis

Iron oxy-hydrate (FeO(OH) iron(III) oxide, hydrated; catalyst grade, 30-50 mesh;), 1-octadecene (ODE 90%), cadmium oxide (CdO 99.99%), selenium powder (Se 100mesh 99%), tri-octylphosphine (TOP 99%), oleic acid (90%) and nitric acid (trace metal grade) were all purchased from SIGMA-ALDRICH®. The 1µm PTFE AERODISC® syringe filter was purchased from PALL LIFE SCIENCE® and a 0.2µm NYL syringe filter was purchased from WHATMAN®.

Iron oxide nanoparticles were synthesized by the thermal decomposition of iron carboxylate salts.[10,16] A mixture of 0.178g of FeO(OH), 2.26g oleic acid and 5.0g of 1-octadecene was stirred and purged with nitrogen; moderate heating up to 280°C in a three neck-flask led to the formation of an orange solution thought to contain iron carboxylates. Further heating to 320°C led to a decomposition of this precursor and the generation of brown-black iron oxide nanocrystals. The reaction product was soluble in hexane because of the adsorption of oleic acid to the nanocrystal surface *via* polar, carboxylate groups.

The iron oxide nanocrystals were purified by repeated cycles of precipitation, sedimentation followed by dispersion in hexane. Reaction products were treated with a 1:1 volumetric amount of acetone and methanol leading to the formation of visible aggregates; these were collected *via* centrifugation in a pellet and could be dispersed back into hexanes. This procedure was repeated five times to remove unreacted iron

salts, 1-ODE or unbound oleic acid. Purified nanocrystal solutions in hexanes could be digested by strong nitric acid and analyzed for their iron content with atomic emission spectroscopy (ICP-OES). Using the average diameter of the material obtained from TEM, and the density of iron oxide (5.17 g/cm^3), the atomic concentration of iron could be converted into a nanoparticle concentration.

CdSe nanocrystals were prepared by heating a stirred mixture of 0.3g of CdO and 2.7g of oleic acid in a 100mL three-neck flask at 200°C until a transparent liquid was obtained.[98] After cooling to room temperature, 15 g of oleic acid and 30g of ODE was added and the mixture heated to 100°C under vacuum for 40 minutes. The solution was then purged with ultra-pure N_2 and heated to 300°C. An injection solution, prepared by mixing 10.68g of Se/TOP (10 wt %) and 4.13g of ODE, was swiftly injected into the flask with a 20mL syringe fitted with a large bore needle. After cooling to room temperature, the crude quantum dots were precipitated by the addition of acetone and methanol, in a fashion similar to that used for the iron oxide. These pellets could be isolated and purified after repeated centrifugation at 3500g followed by redispersion into hexanes. The final purified nanocrystal pellet was ultimately redispersed in hexane, filtered through 1μm PTFE syringe filter and stored in the dark. Quantum dot concentrations were estimated from absorbance data using methods published elsewhere.[99]

2.5.2 Phase transfer of nanocrystals

Oleic acid was added in variable amounts (0.5 - 300μL) to 1.0 mL of purified nanocrystal suspensions in hexanes (typically 1g nanoparticle/L). The resulting solution was then

sonicated in a bath for one minute with no visible change in appearance (FS6 sonicator from FISCHER SCIENTIFIC®). Next, 10mL of ultrapure water (MILLIPORE®, 18.2MΩcm) was then added to the hexane solution resulting in an obvious phase separation between the clear water and colored non-polar solution. To affect the transfer of material from hexanes into water, this solution was subjected to sonication *via* a probe (UP 50H probe sonciator from DR.HIELSCHER®) for 5 minutes at 50% amplitude and full cycle. Care was taken to ensure that the tip of the probe, where the power is the highest, was located near the interfacial region between the hexanes and water phase. Immediately after sonication a cloudy and colored solution was obtained, but if left to sit undisturbed for one day the mixture phase separated with the colored nanoparticles appearing in the bottom, aqueous fraction. This layer was collected and the nanoparticles purified *via* centrifugation at 3500 g for 15min, followed by redispersion and filtration through a syringe filter (pore size of 0.2μm, Whatman-NYL). The filtered product was a clear, colored suspension that could be further concentrated (typically 10X) *via* rotary evaporation. The above procedure was also used to phase transfer cadmium selenide nanocrystals. Methods to describe the phase transfer using IGEPAL® CO 630 are described elsewhere.[2]

2.5.3 Characterization of nanocrystals

Small Angle X-ray Scattering (SAXS) profiles were obtained on a RIGAKU SMARTLAB® system operating in transmission mode with a line collimation setup. A capillary tube (0.8mm diameter) was filled with a sample, and the low angle scattering was collected

from 2θ values of 0.15 to 4 degrees with a Cu K-α X-ray beam of wavelength 1.54Å. The X-rays were generated at 40kv and 44mA. Typical data collection times were on the order of two hours. The raw scattering data was analyzed using Rigaku's NANOSOLVER® software using a split interval of 30 with low slit correction factor.

Dynamic Light Scattering (DLS) data was collected using a BROOKHAVEN® instrument equipped with a BI-9000AT digital autocorrelator using a monitoring wavelength of 656 nm. Standard 1.5 mL poly-methacrylate cuvettes were used as sample holders and each sample was analyzed for 4 minutes to obtain a minimum intensity of 200,000 cps. A histogram of the particle diameter distribution was obtained *via* a "Contin" fit to the raw autocorrelation data.

Transmission electron microscopy (TEM) was carried out using JEOL 2100 field emission gun TEM at 200kV with a single tilt holder using 300mesh copper grids with holey carbon from Ted Pella Inc. Thermo-gravitmetric Analysis (TGA) was carried out using TA INSTRUMENTS® SDT 2960 simultaneous DSC-TGA instrument with sample deposited in a platinum pan. Samples were maintained at 150°C for 5hrs for removal of any associated solvent/moisture before further heating. The samples were then heated to 900°C at the rate of 50°C/min. UV-visible spectroscopy was carried out using Cary 5000 VARIAN® UV-vis-NIR spectrophotometer with 1.5mL poly-methacrylate cuvettes used as sample holders. All sizing data with respective significant figures was reported with error bars representing their standard deviation. Inductively coupled plasma (ICP) analysis was carried out using PERKIN ELMER® ICP-OES instrument equipped with auto-sampler.

Total organic carbon content of the supernatant was computed using SHIMADZU® TOC analyzer after sedimentation of particle suspension (1mL of 1µM) (BECKMAN-COULTER OPTIMA® L-80XP Ultracentrifuge) at 118,000g for 4 hours at 25°C.

CHAPTER 3

Optical tracking of iron oxide nanoparticles

3.1 ABSTRACT

Aqueous dispersions of iron oxide nanoparticles have broad applications in biotechnology and environmental remediation.[4,100] In this regard we have reported highly efficient Arsenic removal using low field magnetic separation.[2] This is achieved by utilizing the high surface to volume ratio of the nanoparticles, which is maximized on uniform dispersion. Therefore, understanding the aggregation of these particles is the key to explain the mechanism behind highly effective magnetic separation at low field gradients. Despite being superparamagnetic, magnetite nanoparticles are known to aggregate even in the absence of a magnetic field owing to their dipolar interactions.[101, 102] Here, we report diffusion measurements of nanoparticles under Brownian motion to determine the size of the particles and hence their degree of aggregation in the absence of a magnetic field by using Stokes-Einstein diffusion equation. An optical tracking system was used where nanoparticles of 11 nm core diameter were tracked using epifluorescence microscopy. Interestingly, the particles with concentration on the order of 10^{-7}M were found to be monodisperse, in confirmation with their superparamagnetic behavior. The data is supported by corresponding small angle X-ray scattering (SAXS) analysis and cryogenic transmission electron microscopy (Cryo-TEM) images. Also, DLS measurements under magnetic field showed that the particles aggregated with time irrespective of initial concentration, followed by re-dispersion into the medium on magnetic field removal without the loss of colloidal stability. The results not only explain the trend observed by previous studies[101,103], but also provide an insight into the

length scales of dipolar as well as van der Waals interactions between the magnetic nanoparticles.

3.2 INTRODUCTION

3.2.1 Uses of iron oxide nanoparticles

Magnetic separation using aqueous nanomagnetite dispersions have tremendous applications in environmental pollution, biotechnology and manufacturing processes[4, 100]. Such iron oxide nanoparticles with high degree of monodispersity can be prepared in organic solutions at high temperatures.[10] These particles can then be made viable for point-of-use by phase transferring them into water by different methods such as bilayer coating, ligand exchange or polymer stabilization.[1,71,76,77] However, it is imperative to understand the suspension behavior of the resulting colloidal system in water in order to tailor these materials to suit their needs.[2,10]

Specifically, iron oxide nanoparticles can be used to chemically adsorb pollutants like arsenic on their surface and then be removed by magnetic separation. Higher the surface area of the magnetic particles larger would be the amount of target molecules that could potentially be adsorbed and separated.[2] In this regard a spherical 12 nm particle has about 40% of total iron oxide molecules on its surface. Hence, surface material accounts for a major portion of the entire particle and therefore represents its physico-chemical properties to a large extent.

3.2.2 Motivation

The surface area availability is directly correlated to the degree of aggregation present in the system. Increased aggregation leads to reduced adsorption of target molecules. Iron oxide nanoparticles below 20 nm are in general, considered to be

superparamagnetic in nature. This means that they do not retain any magnetization on removal of the magnetic field unlike bigger micron sized particles. However, there is ambiguity in literature as to when the exact transition to superparamagnetism occurs.[104,105] Other factors such as inadequate surface stabilization can also lead to aggregation of these iron oxide nanoparticles even in absence of a magnetic field.

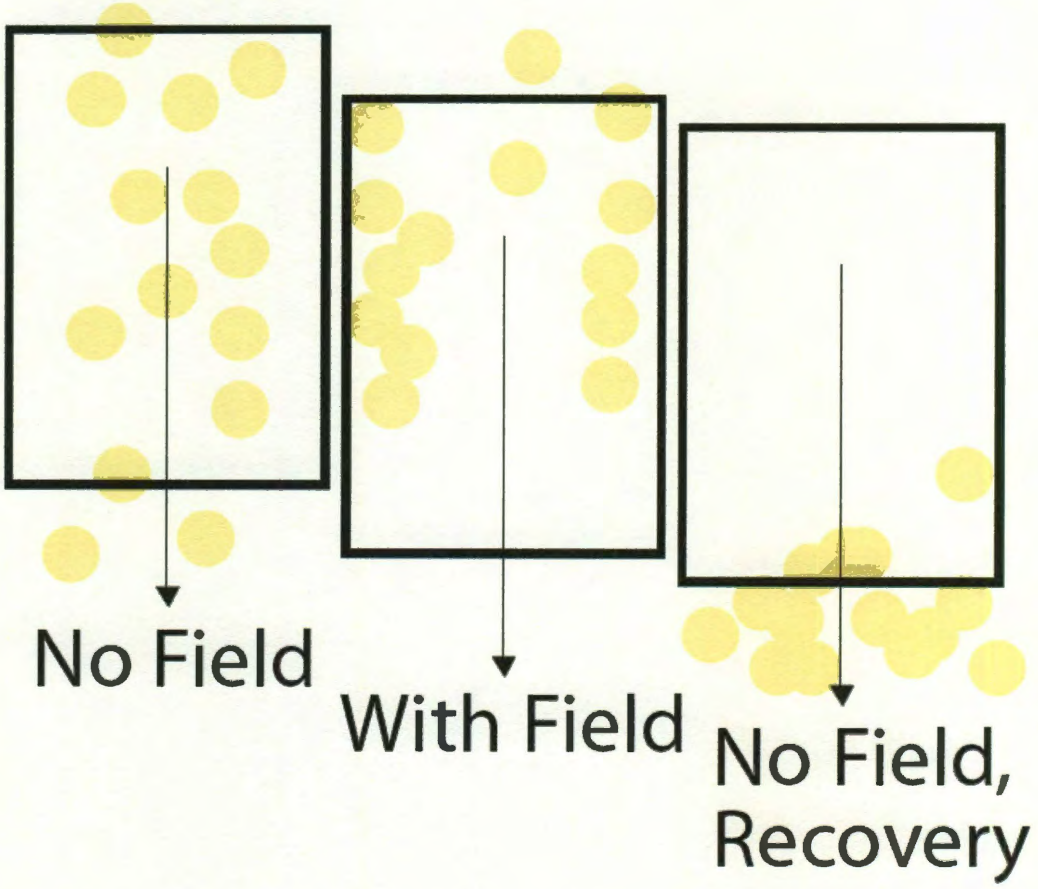

Figure 3.1: Cartoon depiction of magnetic separation of superparamagnetic iron oxide nanoparticles.

A study was previously reported involving the use of such superparamagnetic materials for magnetic separation at extremely low fields.[2] The field gradients used in this study was lower than that needed to separate individual particles below 50 nm. This means

that particles are behaving as groups that can be easily removed at lower field gradients, which implies either aggregation or flocculation in these systems. Aggregation here refers to merging of the physical boundaries of nanocrystals, whereas flocculation refers to the formation of groups or 'flocs' that move together in a magnetic field. The aforementioned work proposed a reversible flocculation mechanism where particles behave as 'flocs' in presence of a magnetic field but disperse back into solution on shaking, once the field is removed (Figure 3.1). Hence, our goal is to evaluate the aggregation behavior of these materials and to verify the validity of the above proposition. This we achieve by single particle tracking coupled with new analysis strategies and error minimization.

3.2.3 Single particle tracking

Single particle tracking uses tools like fluorescence microscopy and back scattering.[106-108] These methods give the hydrodynamic size that is pertinent to the solution behavior of the particles.[109] Researchers have been successful in tracking gold particles up to 5 nm in size *via* backscattering methods and auto-fluorescent quantum dots as small as 15 nm *via* fluorescence microscopy.[106,110,111]

Albeit backscattering is a powerful technique, it cannot be applied to iron oxide nanoparticles owing to their strong absorption; fluorescence imaging however, is still a viable visualization tool.[112] To the best of our knowledge, there are no studies reporting the single particle tracking of iron oxide nanoparticles as small as 10 nm that are tagged with a fluorescent dye. This is due to the complexities and challenges involved in imaging sub-resolution particles. Some of these problems from the materials

perspective are lack of good starting nanocrystals and optimal aqueous stabilization methods. Whereas, those from the imaging viewpoint are diffraction limited resolution, pixelization effect, inefficient fluorophore tagging and ultra-fast particle diffusion.

3.2.4 Novelty

Development of new methods for data collection and dye-tagging are therefore needed to overcome these difficulties. On doing so, the data obtained can be effectively used to decipher the aggregation state of the particle population. The diffusion coefficients of particles in a medium can be calculated and correlated to their size using the Stokes-Einstein diffusion equation – and thereby information about their suspension behavior can be obtained.

Here we report trajectory measurements of nanoparticles under Brownian motion in the absence of a magnetic field. An optical tracking system was used where nanoparticles of 11 nm core diameter were tracked using epifluorescence microscopy. Interestingly the particles with concentration on the order of 10^{-7}M were found to be monodisperse, in confirmation with their superparamagnetic behavior. The data was supported by corresponding Small Angle X-ray Scattering (SAXS) and Dynamic Light Scattering (DLS) analysis along with Cryogenic Transmission Electron Microscopy (Cryo-TEM) images.

3.3 RESULTS AND DISCUSSION

3.3.1 Magnetism on the nanoscale

Basic Concepts of Magnetism

Magnetic materials in nature are classified as diamagnetic, paramagnetic and ferromagnetic, based on their volumetric magnetic susceptibility χ.[113]

$$M = \chi H \tag{3.1}$$

where, M is the magnetization (magnetic moment per unit volume) induced in a material by a field strength H. Typical χ values range from 10^{-3} to 10^{-6} for diamagnets, from 10^{-5} to 10^{-3} for paramagnets and from 50 to 10,000 for ferromagnets. When a magnetic field (H) is applied to a ferromagnetic material, it becomes magnetized as the spins within material align with the applied field.[114] The result is an induced field with a value of

$$B = \mu_o(M + H) \tag{3.2}$$

$$B = \mu H \tag{3.3}$$

where, μ_o is the permeability of free space, μ is the absolute permeability of the material.[113]

With an increase in H, the material attains a maximum value known as saturation magnetization, M_s. This occurs because all the spins are aligned with the applied field. If H is reduced to zero, the material still retains some of the magnetization (residual

magnetic moment) known as remanence. On reversal of applied field, the plot of magnetization (M) versus magnetic field strength (H) traverses a sigmoidal shape, attaining zero magnetization at an applied field H_c, known as coercive field. This traversal continues until a saturation magnetization is achieved in the reverse direction. This hysteretic behavior is characteristic of ferromagnets (Figure 3.2).

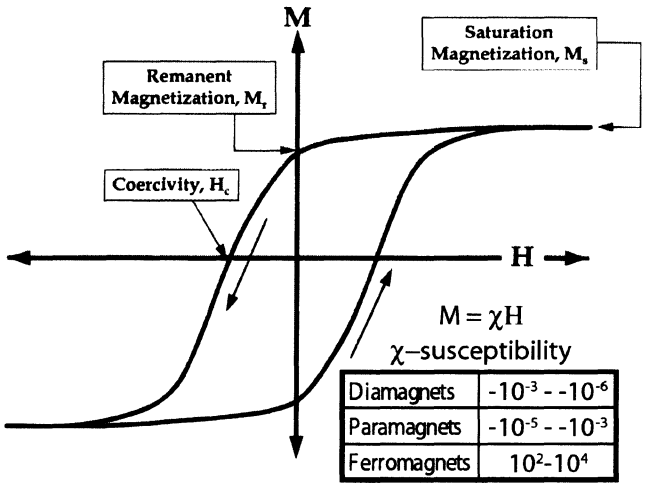

Figure 3.2: Typical magnetic hysteresis loop.[114]

Now let us look into the magnetic properties in the nano-regime. Nanomagnetic materials have crystalline and shape anisotropies arising from spin - orbit coupling. This is uniaxial in nature and thermodynamically favors a specific direction or easy axis for crystallographic alignment in the presence of field.[114] Magnetic materials in general, consist of domains that represent a group of spins, which behave cooperatively by aligning in the same direction and are terminated by domain walls. In micron sized particles there are many such domains and thus the material is described to possess a multi-domain state. Magnetization reversal in these particles is achieved by the motion of the domain walls.[114]

Below a critical diameter, domain walls are no longer formed, and what results is a single domain state (Figure 3.3). These particles require a synchronous spin rotation to achieve magnetization reversal and hence have a higher coercive force. For magnetite nanoparticles this transition occurs around 60 nm. As the particle gets smaller, another critical diameter is reached, where the thermal fluctuations ($\Delta E = K_b T$) become dominant and can flip the magnetic moment, thereby destabilizing the magnetization. At this size, the coercive field approaches zero as $\Delta E = KV$ becomes $< K_b T$. Here, ΔE is the energy barrier for moment reversal, *K* is the anisotropic energy density and *V* is the particle volume, K_b is Boltzmanns' constant and *T* is the absolute temperature.[4,115,116] Such particles are said to be superparamagnetic in nature and have no preferred directional ordering in the absence of a magnetic field, as their net magnetic moment is zero.[4,117]

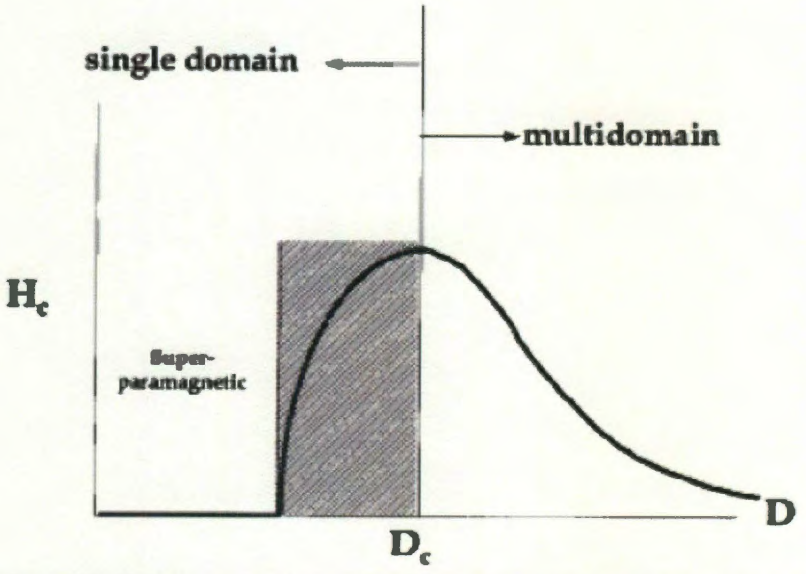

Figure 3.3: Qualitative description of change in coercivity (H_c) as a function of particle size (D_c< 100 nm).[114]

It is now clear that the shape of hysteresis loops depend upon the size of the particles and the domain states. Larger particles that have a multi-domain state exhibit a narrow hysteresis loop on account of lower field energy required to magnetize them whereas, smaller single domain particles exhibit a broad hysteresis loop. Superparamagnetic materials, however, display a sigmoidal anhysteric loop (Figure 3.4).

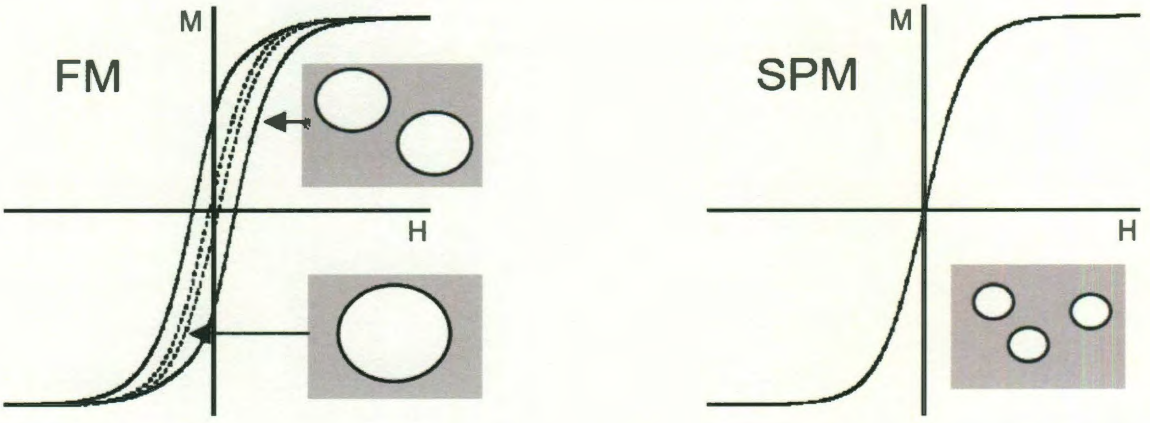

Figure 3.4: Hysteresis loop comparison: Multi-domain ferromagnetic material versus single-domain superparamagnetic material.[116]

3.3.2 Superparamagnetic limit

Many researchers have undertaken the task of determining the size at which nanoparticles become superparamagnetic (SPM). The experimental results are usually compared with Neels single domain theory that predicts a size of 30 nm at room temperature for magnetite. Dunlop (1973) conducted saturation remanence measurements and concluded a critical size d_s = 29-36 ± 5 nm for the onset of SPM in magnetite at room temperature.[118] Goya *et al.* (2005) carried out H_c studies and reported a size of 10 nm.[117] Dearing *et al.*(1996) suggested that most superparamagnetic grains are between 10 and 25 nm in diameter.[104] Study by Worm

(1998) is of particular interest as it concludes the SPM onset on the basis of blocking volume by measuring the frequency dependence of AC susceptibility.[105] This study gives a SP/SSD threshold of d_s(500Hz) = 17 nm. Our laboratory measurements using superconducting quantum interference device (SQUID) gives a value of 15 nm.

3.3.3 Basis

However, it is crucial to know if the nanoparticles behave as superparamagnetic materials in a solution - to see if they act individually or as flocculated particles in the absence of a magnetic field. Theoretical models for the force balance on a single magnetic particle in presence of a magnetic field that take into account the hydrodynamic drag force, the randomizing Brownian force and the magnetic force conclude that for an applied field of 1T, the magnetic force exceeds the hydrodynamic force at around 20 nm at a distance of 1cm away from the magnetic field.[119] On the contrary, previously reported experiments efficiently separate particles below 20 nm in magnetic fields as low as 0.1T (Figure 3.5).[2]

A reversible phenomena where particles flocculate in the presence of a field and hence separate at low field gradients, but disperse back into solution once the field is removed was proposed.[2] To prove this the first step was to find out whether the particles were aggregated or not, in the absence of a magnetic field. Also, superparamagnetic limit was not measured experimentally in any other way than by susceptibility measurements, which unfortunately does not give any information about their behavior in suspension.

This motivated us to compute the aggregation state of particles by optical tracking *via* fluorescence microscopy.

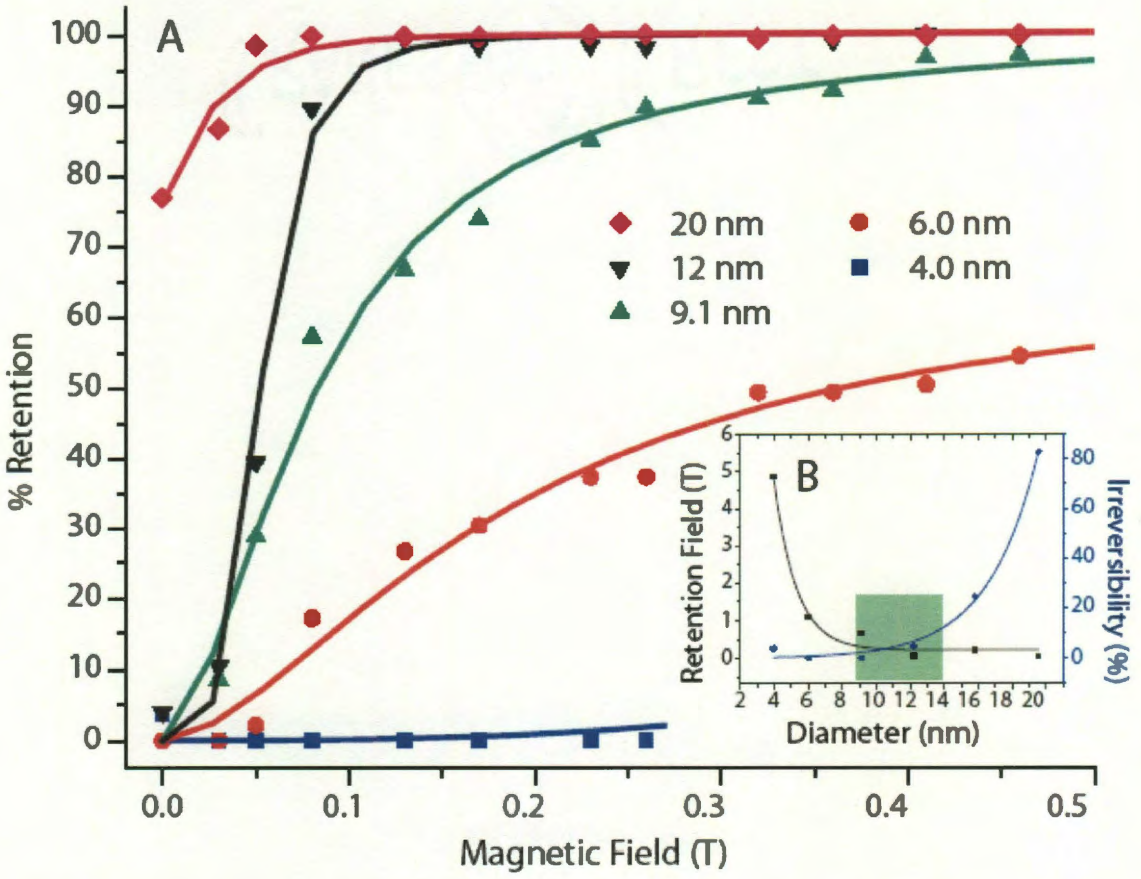

Figure 3.5: Size dependent magnetic separation: % Retention as a function of applied magnetic field.[2]

3.3.4 Theoretical considerations

The idea behind optical tracking is to determine the particle size by obtaining the associated diffusion coefficient. In this regard, starting with Fokker Plank equation for Brownian motion for continuous time symmetric random walk, an equation for diffusion coefficient (D) of an N-dimensional Brownian motion can be derived as

$$D = \frac{1}{2 \cdot N \cdot \Delta t} \cdot \left\langle \sum_{i=1}^{n} \Delta x_i^{\,2} \right\rangle_{x_1,\ldots,x_N} \tag{3.4}$$

where, Δx is the particle displacement in an interval of time Δt and n is the number of samples. (Appendix A)

Equation 3.4 can be used as an unbiased estimator of *D* as long as the particle displacements between the time intervals and the overall observation time are large enough compared to the optical resolution of the imaging system and the sampling rate respectively.

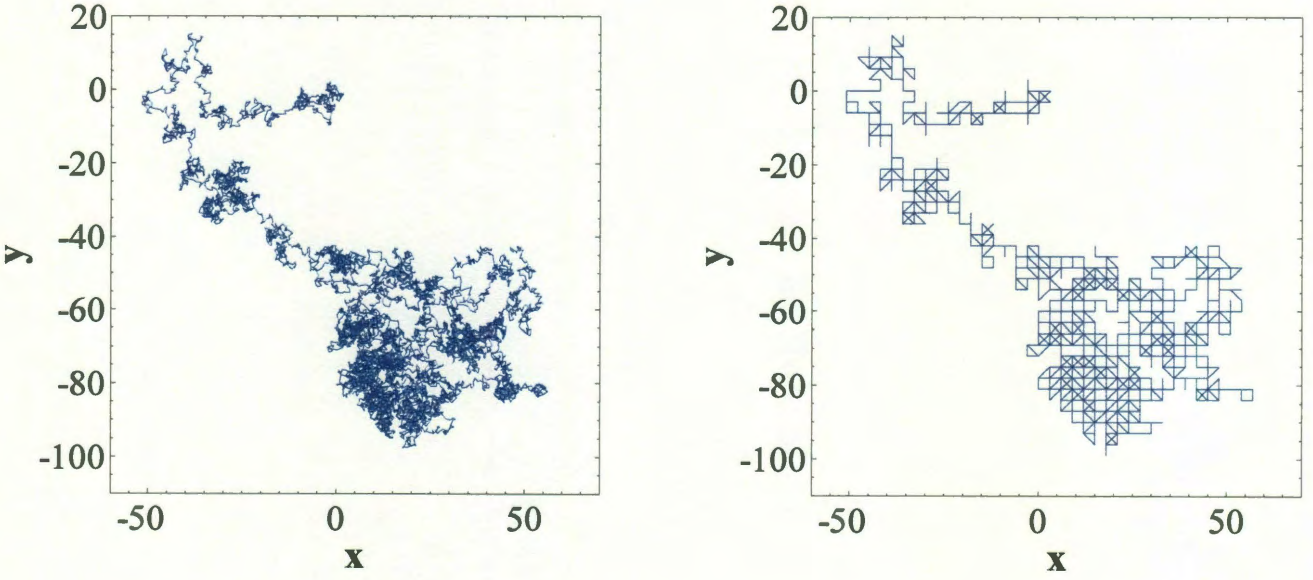

Figure 3.6: Simulation of an example random walk (left) and the walk pixilated (right).

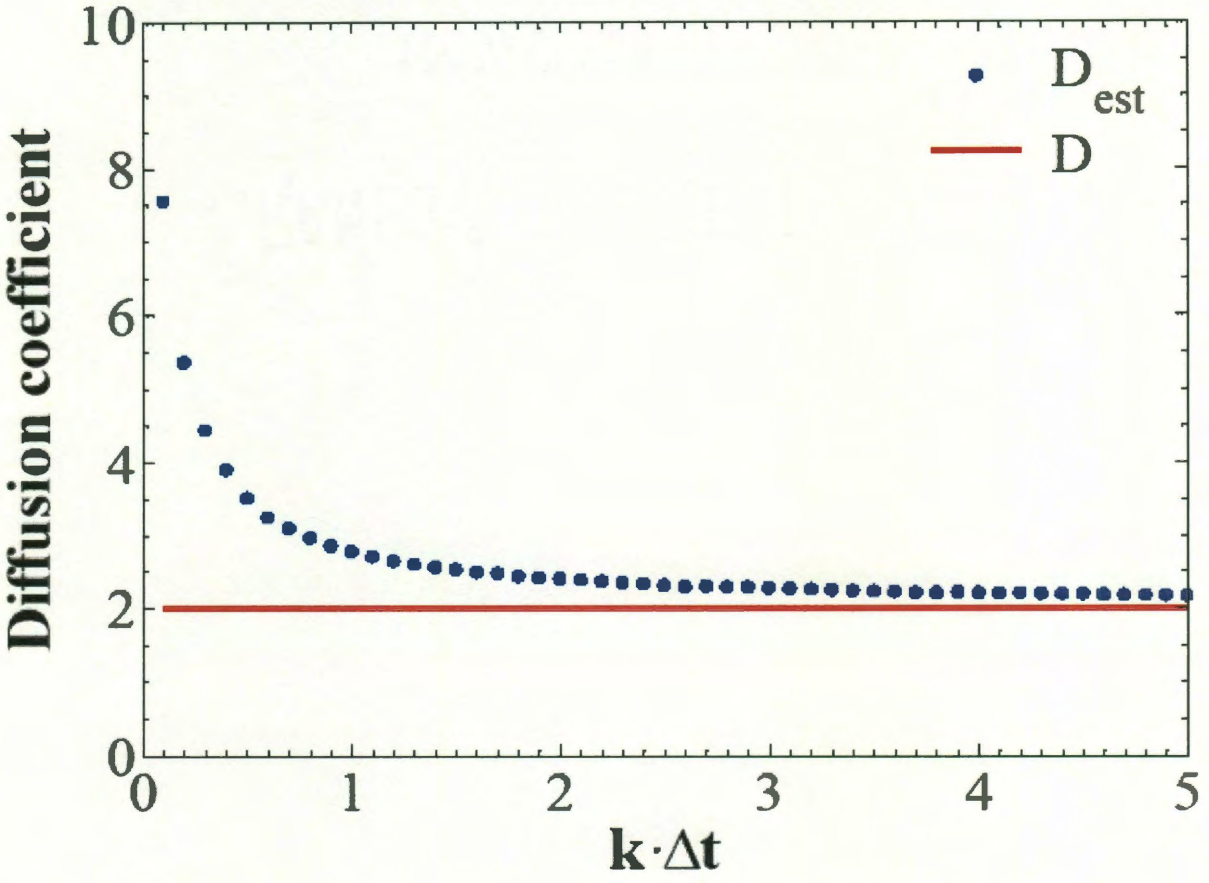

Figure 3.7: Plot of diffusion coefficient with time showing that at higher sampling factor (k) values the estimated D approaches the actual D.

3.3.5 Visualization challenges at nanoscale

There are several obstacles encountered in visualizing the trajectories traversed by nanoparticles. For example, 12 nm core iron oxide particles – in a medium such as water, move out of focus every 50 frames on average at a capture rate of 30 frames per second. This occurs due to the combination of fast thermal diffusion and the depth of field associated with the objective. A 1.4 numerical aperture oil objective with 60x magnification has a depth of field of about 200 nm.

Also, the diffraction limited optical resolution achievable is 250-300 nm, which means that one cannot visualize the shape of a particle below this limit. A part of the solution for this is the use of fluorescence microscopy where the image obtained is not that of the particle but the fluorescence signal from the dye molecules tagged to the particle. Nevertheless, tracking the motion of a particle whose length scale is an order of magnitude lesser than the optical limit requires new strategies. In addition capture of the trajectory *via* a charge coupled device (CCD) camera inevitably gives rise to pixelization effect, where the position of the particle whose size is smaller than that of a pixel cannot be computed easily (Figure 3.6). Electron-bombarded CCD's have a fixed resolution (Hamamatsu C7190 - 140 nm/pixel) traded for the enhanced light sensitivity. This inability to change the resolution of the camera adds a limitation to the visualization process.

These problems result in not being able to capture a continuous large set of in-focus frames that is necessary for deciphering statistically significant information from the data. The error in the computation of the diffusion coefficient D varies at $n^{-½}$, where n is number of sample frames comprising of the particle trajectory (Appendix A).[109] As a result of this, the estimated diffusion coefficient (D_{est}) approaches the actual D value with increasing time, and hence makes it crucial to procure large sets of continuous frames. For example, if one were to sample at integral multiples of a fixed Δt that we define as a sampling factor k, then the calculated D_{est} value converges to the actual D as k increases. (Figure 3.7).

In order to overcome these difficulties, a new track-shift methodology was developed (Figure 3.8). We were able to obtain a trajectory comprising of at least 5000 frames that was extracted from individual sets of frames collected while the particles were in focus. These initial sets of frames were hence discontinuous in time; each set comprising of about 30-40 frames collected at a rate of 30 frames per second. Assuming an ideal Brownian path which essentially is a "memory-less" random Markovian process, these data sets were combined, for example, by connecting the end of the first in-focus trace to the beginning of the second and so on. This not only resulted in large continuous set of in-focus frames but also helped us to utilize all the collected data without the need of interpolation for the missing out-of-focus frames in between traces.

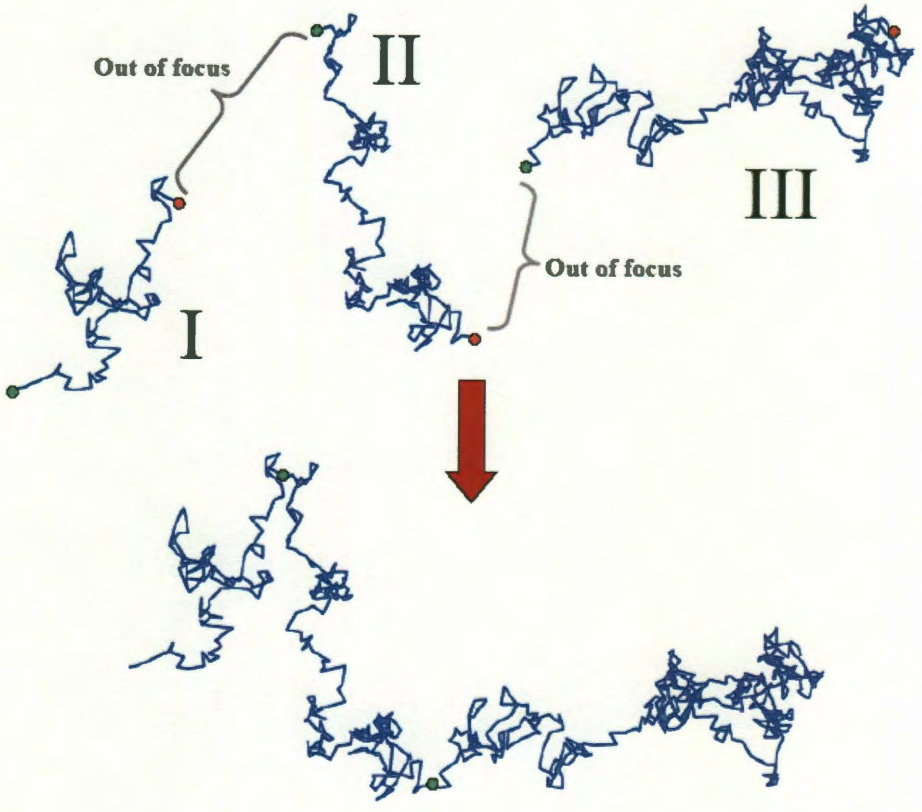

Figure 3.8: Track-shift methodology utilized to obtain large set of continuous frames.

The different sets of "in-focus" traces stitched together using this track-shift methodology can correspond to different nanoparticles. In fact, the measured diffusion coefficient ‹*D*› is the ensemble average of the *D* of the particle size distribution. Since *D* is inversely proportional to the particle hydrodynamic radius *a*, ‹*D*› and ‹*a*› both represent the same first moment of distribution.

The pixelization effect was minimized by the tracking algorithm embedded in the Metamorph software. The position of the particle (coordinates of maximum intensity) was resolved at a sub-pixel level by deconvolution followed by a centroid fit on the resulting image. However, Gaussian errors were still present in the estimating of the position of the particle. This leads us into an explanation of statistical errors.

3.3.6 Errors

As explained above, the Brownian process being stochastic in nature is bound to have theoretically expected statistical variances.[120,121] The sample size that is proportional to the numbers of time steps analyzed is an important factor in deciding the error of the estimation. The accuracy of the diffusion coefficient obtained varies as the inverse of the square root of the number of samples (Appendix A).

Also, bias in the estimation of diffusion coefficient can be introduced due to the error in estimating the exact position of the particle at any given time. By assuming a Gaussian profile for this error, we have derived the bias to be inversely proportional to the time interval between two consecutive positions of the particle in consideration (Δt) and the

diffusion coefficient (D) (Appendix B). It implies that if we fix the acceptable bias in the measurement at a particular value, say 5%, then using a higher viscous solvent that leads to a lower D value, will increase the acceptable Δt. Using a lower Δt will result in the computed displacements that are comparable to the length scale of the errors. This calls for minimizing the error by collecting a large number of frames that result in the stabilization of the obtained diffusion coefficient.

3.3.7 Fluorophore tagging

The fluorophore PKH-26 was used to track the iron oxide nanoparticles. The fluorophore needs to have a long lifetime, large extinction coefficient and a good quantum yield.[122] PKH-26 has excitation and emission peaks at 551 and 567 nm respectively and a half life greater than 100 days.[123] At 10mM and 555 nm excitation, it has an absorbance of 1.4 which is a measure of its high extinction coefficient. Tagging was carried out to ensure at least about 200 dye molecules were present per particle, wherein the dye molecules tag onto the oleic acid bilayer *via* van der Waals interaction.

3.3.8 Optical tracking

Here, we present visualization of iron oxide nanoparticles whose size is below 20 nm. Sample droplet was placed in between a coverslip and glass slide with a mylar spacer (50 μm). The Brownian paths of the particles were then captured *via* epifluorescence microscopy at a frame rate of 30fps. The trajectory of the Brownian particle was obtained using Metamorph software. Displacements calculated from the trajectory information were then input to a code (Appendix C) to compute diffusion coefficient in

accordance with Equation 3.4. Diameter of the particles and hence their state of aggregation was computed using Stokes-Einstein relation $D = K_b T / 6\pi\eta a$ where K_b is the Boltzmann's constant, η is the dynamic viscosity of the dispersion medium at temperature *T* and *a* is the particle hydrodynamic radius.

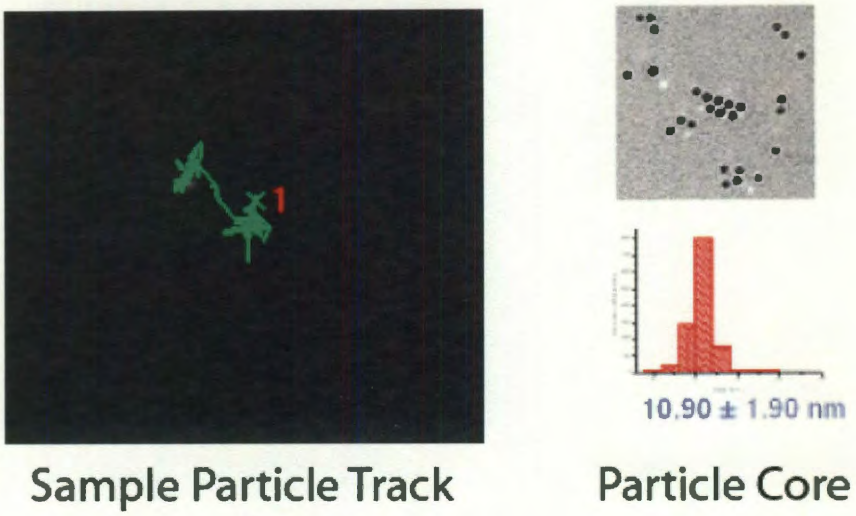

Figure 3.9: Sample of a particle track obtained *via* fluorescence microscopy (left) and particle core size distribution obtained by Cryo-TEM (right).

3.3.9 Tracking results

Eighteen sets of particle traces with at least 500 frames/set were collected and analyzed for the diffusion coefficient (sample trace: Figure 3.9). In a high viscosity solvent such as PEG 400, a particle typically stays in focus long enough to get a mean square displacement of approximately 30 $(\mu m)^2$ which corresponds to a linear displacement of 400 pixels on average. As shown in Figure 3.10, for an expected hydrodynamic size of 22 nm of tagged iron oxide nanoparticles stabilized by an oleic acid bilayer, the diameter value stabilized at 29 nm at increased sample sizes corresponding to a k value greater

than 4. This data was corroborated by other techniques such as small angle X-ray scattering (SAXS – Figure 3.11) and cryogenic transmission electron microscopy (Cryo-TEM – Figure 3.9). SAXS gives a value of 14.3 ± 1.8 nm which comprises the magnetic core and oleic acid coating. This proves that the particles in consideration are superparamagnetic and hence monodisperse in absence of a magnetic field.

Further work in this direction would involve the tracking of particles under a flow and in presence of a magnetic field to determine their capture trajectory and flocculation behavior. Preliminary experiments using dynamic light scattering (DLS) has shown that particles reversibly flocculate on application of a magnetic field. The next step would be to track particles whose sizes are above 20 nm to determine their departure trend from superparamagnetism. Also, concentration dependence of iron oxide particles on their aggregation could be explored using the methodology reported in this study as a basis.

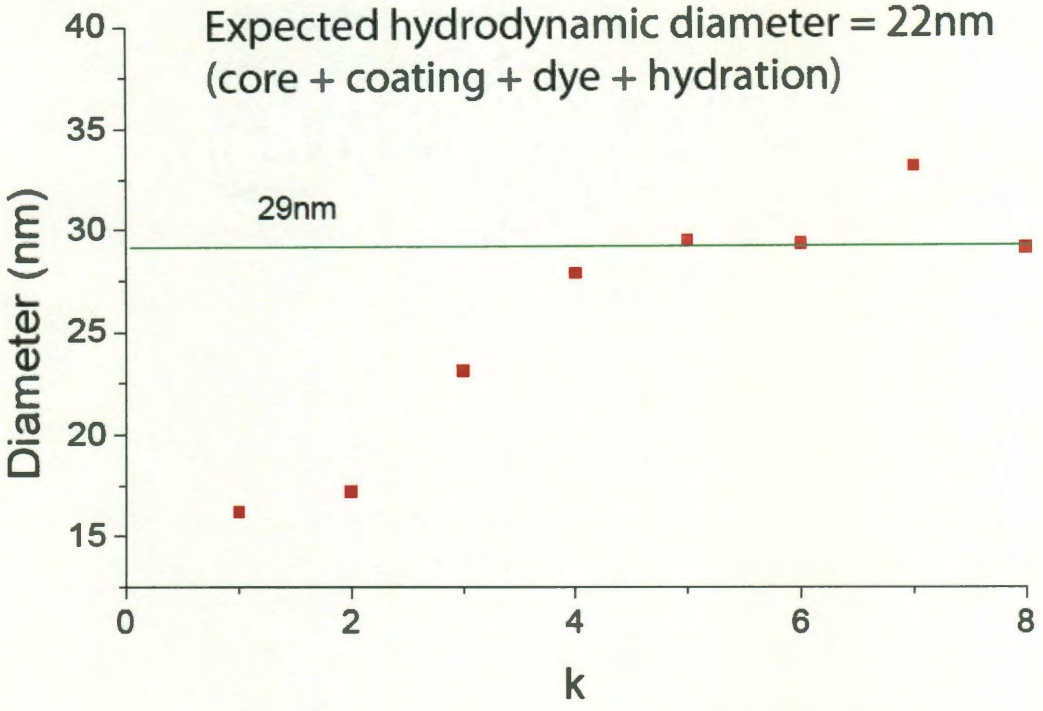

Figure 3.10: Plot of diameter versus sampling factor (k) shows that the diameter stabilizes in the k range 5-10.

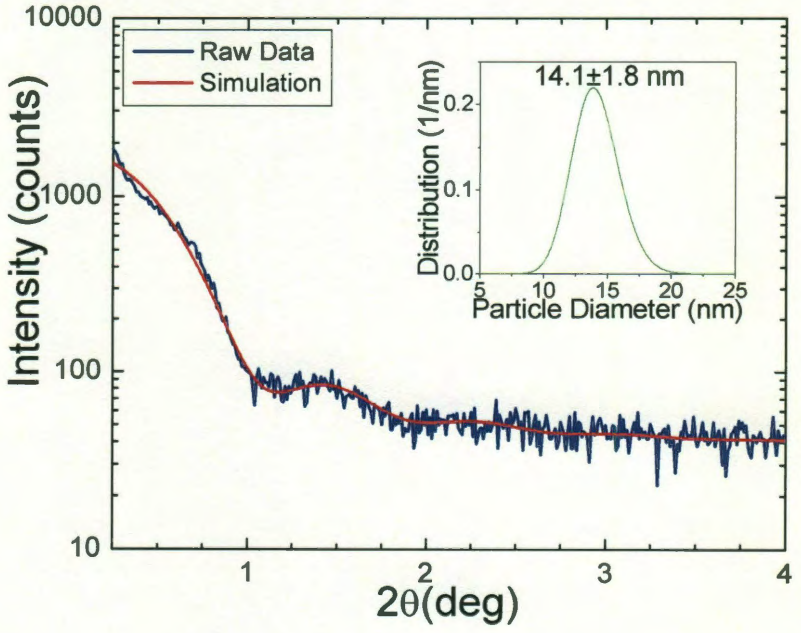

Figure 3.11: SAXS analysis of 11 nm sized particles in water.

3.4 CONCLUSIONS

Optical tracking of magnetite nanoparticles in water was carried out successfully. A novel track shift methodology was developed to maximize data collection and obtain large sets of continuous in-focus frames. Brownian paths were simulated to prove that the diffusion coefficient estimated from experiments converges to the true diffusion coefficient. The associated computational errors were modeled and minimized by different strategies. The particles analyzed were found to be monodisperse in nature in confirmation with their superparamagnetic behavior. The data obtained was corroborated by other characterization techniques such as SAXS and DLS. With these results it could be inferred that the superparamagnetic particles separate at low field gradients (100 T/m) only under reversible flocculation.

3.5 METHODS AND MATERIALS

Fluorescence microscopy was carried out using a Nikon eclipse E600 epifluorescence microscope in transmission mode, coupled with a CCD camera. A 100W mercury lamp was used as the light source with a 1.40 NA Nikon Plan-Apo 60X oil immersion objective at a working distance of 0.21mm. PKH26 fluorophore was used to tag the nanomagnetite. PKH 26 has an excitation peak at 551 nm and emission peak at 567 nm. Hence, the filter cube (XF37 Omega Inc.) was used that had a bandpass excitation filter (540-550 nm), dichroic mirror (555 nm) and a long pass emission filter (570-600 nm). The dye fluoresced in the visible region, rendering the visualization of nanomagnetite indirectly. The images were collected at 30 frames per second using an electron bombarded CCD (EBCCD) camera *C*7190 (Hamamatsu, Japan) monitored by the software Metamorph (Universal Imaging Inc), and were of dimensions 480x640 pixels. The glass slides used were plasma cleaned in order to render a hydrophilic surface that would avoid any surface immobilization of particles.

The nanomagnetite sample used had a magnetite core, coated with oleic acid bilayer in water.[1] 5μL of dye was added to 1mL of nanomagnetite of 500 nM concentration and stirred overnight. The sample was then subjected to a static separator (Dexter Magnetic LifeSep 50SX) in order to separate the tagged magnetite and free dye. This process was repeated three times to ensure the absence of free dye in the solution. The separation in the magnetic separator served as a proof for the presence of magnetite. Dye coverage of approximately 200 dye molecules per nanoparticle was estimated using UV-

vis absorption (Cary-5000 UV-Vis-NIR, VARIAN) and inductively coupled plasma atomic emission spectroscopy (Perkin Elmer ICP-Optimal Emission Spectrophotometer).

Small Angle X-ray Scattering was carried out on Rigaku SmartLab in transmission mode with a line collimation setup. A capillary tube (1mm diameter) with a sample length of 30mm was filled with sample (magnetite in water), and was analyzed at small angles between 0.06 and 8 degrees with a CuK-α x-ray beam of wavelength 1.54Å. The X-rays were generated at 40kV and 44mA. The capillary tube was sealed off at both the ends using a fast-setting epoxy. Typical analysis time was 2hrs, each for sample and the blank capillary. The raw data obtained was analyzed on NanoSolver (Rigaku Instruments Inc.) software by considering a core-shell model. Dynamic light scattering was conducted in a Brookhaven BI- 9000AT with a digital autocorrelator at 656nm wavelength, at $\Theta = 90°$ and 25 °C. Standard 4ml quartz cuvettes were used to hold the sample.

REFERENCES

1. Prakash, A.; Zhu, H. G.; Jones, C. J.; Benoit, D. N.; Ellsworth, A. Z.; Bryant, E. L.; Colvin, V. L., Bilayers as Phase Transfer Agents for Nanocrystals Prepared in Nonpolar Solvents. *Acs Nano* **2009,** *3*, 2139-2146.

2. Yavuz, C. T.; Mayo, J. T.; Yu, W. W.; Prakash, A.; Falkner, J. C.; Yean, S.; Cong, L. L.; Shipley, H. J.; Kan, A.; Tomson, M., *et al.*, Low-Field Magnetic Separation of Monodisperse Fe3o4 Nanocrystals. *Science* **2006,** *314*, 964-967.

3. Zhu, H.; Prakash, A.; Benoit, D. N.; Jones, C. J.; Colvin, V. L., Low Temperature Synthesis of Zns and Cdzns Shells on Cdse Quantum Dots. *Nanotechnology* **2010,** *21*, 255604.

4. Bucak, S.; Jones, D. A.; Laibinis, P. E.; Hatton, T. A., Protein Separations Using Colloidal Magnetic Nanoparticles. *Biotechnology Progress* **2003,** *19*, 477-484.

5. Kim, J.; Lee, J. E.; Lee, J.; Yu, J. H.; Kim, B. C.; An, K.; Hwang, Y.; Shin, C. H.; Park, J. G.; Kim, J., *et al.*, Magnetic Fluorescent Delivery Vehicle Using Uniform Mesoporous Silica Spheres Embedded with Monodisperse Magnetic and Semiconductor Nanocrystals. *Journal of the American Chemical Society* **2006,** *128*, 688-689.

6. Oberteuffer, J., Magnetic Separation: A Review of Principles, Devices, and Applications. *Ieee Transactions on Magnetics* **1974,** *10*, 223-238.

7. Yu, H.; Gibbons, P. C.; Kelton, K. F.; Buhro, W. E., Heterogeneous Seeded Growth: A Potentially General Synthesis of Monodisperse Metallic Nanoparticles. *Journal of the American Chemical Society* **2001,** *123*, 9198-9199.

8. Huang, J. H.; Parab, H. J.; Liu, R. S.; Lai, T. C.; Hsiao, M.; Chen, C. H.; Sheu, H. S.; Chen, J. M.; Tsai, D. P.; Hwu, Y. K., Investigation of the Growth Mechanism of Iron Oxide Nanoparticles Via a Seed-Mediated Method and Its Cytotoxicity Studies. *Journal of Physical Chemistry C* **2008,** *112*, 15684-15690.

9. Park, J.; An, K. J.; Hwang, Y. S.; Park, J. G.; Noh, H. J.; Kim, J. Y.; Park, J. H.; Hwang, N. M.; Hyeon, T., Ultra-Large-Scale Syntheses of Monodisperse Nanocrystals. *Nature Materials* **2004,** *3*, 891-895.

10. Yu, W. W.; Falkner, J. C.; Yavuz, C. T.; Colvin, V. L., Synthesis of Monodisperse Iron Oxide Nanocrystals by Thermal Decomposition of Iron Carboxylate Salts. *Chemical Communications* **2004**, 2306-2307.

11. Raj, K.; Moskowitz, R., Commercial Applications of Ferrofluids. *Journal of Magnetism and Magnetic Materials* **1990,** *85*, 233-245.

12. Sun, S. H.; Zeng, H.; Robinson, D. B.; Raoux, S.; Rice, P. M.; Wang, S. X.; Li, G. X., Monodisperse Mfe2o4 (M = Fe, Co, Mn) Nanoparticles. *Journal of the American Chemical Society* **2004,** *126*, 273-279.

13. Sugimoto, T., Preparation of Monodispersed Colloidal Particles. *Advances in Colloid and Interface Science* **1987,** *28*, 65-108.

14. Dubertret, B.; Skourides, P.; Norris, D. J.; Noireaux, V.; Brivanlou, A. H.; Libchaber, A., In Vivo Imaging of Quantum Dots Encapsulated in Phospholipid Micelles. *Science* **2002,** *298*, 1759-1762.

15. Murray, C. B.; Norris, D. J.; Bawendi, M. G., Synthesis and Characterization of Nearly Monodisperse Cde (E = S, Se, Te) Semiconductor Nanocrystallites. *Journal of the American Chemical Society* **1993,** *115*, 8706-8715.

16. Hyeon, T.; Lee, S. S.; Park, J.; Chung, Y.; Bin Na, H., Synthesis of Highly Crystalline and Monodisperse Maghemite Nanocrystallites without a Size-Selection Process. *Journal of the American Chemical Society* **2001,** *123*, 12798-12801.

17. Buffat, P.; Borel, J. P., Size Effect on Melting Temperature of Gold Particles. *Physical Review A* **1976,** *13*, 2287-2298.

18. Hai, H. T.; Yang, H. T.; Kura, H.; Hasegawa, D.; Ogata, Y.; Takahashi, M.; Ogawa, T., Size Control and Characterization of Wustite (Core)/Spinel (Shell) Nanocubes Obtained by Decomposition of Iron Oleate Complex. *Journal of Colloid and Interface Science* **2010,** *346*, 37-42.

19. Sun, S. H.; Zeng, H., Size-Controlled Synthesis of Magnetite Nanoparticies. *Journal of the American Chemical Society* **2002,** *124*, 8204-8205.

20. Xie, J.; Peng, S.; Brower, N.; Pourmand, N.; Wang, S. X.; Sun, S. H., One-Pot Synthesis of Monodisperse Iron Oxide Nanoparticles for Potential Biomedical Applications. *Pure and Applied Chemistry* **2006,** *78*, 1003-1014.

21. Yin, Y.; Alivisatos, A. P., Colloidal Nanocrystal Synthesis and the Organic-Inorganic Interface. *Nature* **2005,** *437*, 664-670.

22. Lamer, V. K.; Dinegar, R. H., Theory, Production and Mechanism of Formation of Monodispersed Hydrosols. *Journal of the American Chemical Society* **1950,** *72*, 4847-4854.

23. Overbeek, J. T. G., Monodisperse Colloidal Systems, Fascinating and Useful. *Advances in Colloid and Interface Science* **1982,** *15*, 251-277.

24. Wey, J. S.; Strong, R. W., Growth Mechanism of Agbr Crystals in Gelatin Solution. *Photographic Science and Engineering* **1977,** *21*, 14-18.

25. Bronstein, L. M.; Huang, X. L.; Retrum, J.; Schmucker, A.; Pink, M.; Stein, B. D.; Dragnea, B., Influence of Iron Oleate Complex Structure on Iron Oxide Nanoparticle Formation. *Chemistry of Materials* **2007,** *19*, 3624-3632.

26. Yin, M.; Chen, Z. Y.; Deegan, B.; O'Brien, S., Wustite Nanocrystals: Synthesis, Structure and Superlattice Formation. *Journal of Materials Research* **2007,** *22*, 1987-1995.

27. Peng, X. G.; Wickham, J.; Alivisatos, A. P., Kinetics of Ii-Vi and Iii-V Colloidal Semiconductor Nanocrystal Growth: "Focusing" Of Size Distributions. *Journal of the American Chemical Society* **1998,** *120*, 5343-5344.

28. Chen, S. L.; Dong, P.; Yang, G. H., The Size Dependence of Growth Rate of Monodisperse Silica Particles from Tetraalkoxysilane. *Journal of Colloid and Interface Science* **1997,** *189*, 268-272.

29. Nagao, D.; Satoh, T.; Konno, M., A Generalized Model for Describing Particle Formation in the Synthesis of Monodisperse Oxide Particles Based on the Hydrolysis and Condensation of Tetraethyl Orthosilicate. *Journal of Colloid and Interface Science* **2000,** *232*, 102-110.

30. Vanderhoff, J. W.; Vitkuske, J. F.; Bradford, E. B.; Alfrey, T., Some Factors Involved in the Preparation of Uniform Particle Size Latexes. *Journal of Polymer Science* **1956,** *20*, 225-234.

31. Park, J.; Lee, E.; Hwang, N. M.; Kang, M. S.; Kim, S. C.; Hwang, Y.; Park, J. G.; Noh, H. J.; Kini, J. Y.; Park, J. H., *et al.*, One-Nanometer-Scale Size-Controlled Synthesis of Monodisperse Magnetic Iron Oxide Nanoparticles. *Angewandte Chemie-International Edition* **2005,** *44*, 2872-2877.

32. Kahlweit, M., Ostwald Ripening of Precipitates. *Advances in Colloid and Interface Science* **1975,** *5*, 1-35.

33. Liu, Y.; Kathan, K.; Saad, W.; Prud'homme, R. K., Ostwald Ripening of Beta-Carotene Nanoparticles. *Physical Review Letters* **2007,** *98*.

34. Wey, J. S.; Strong, R. W., Influence of Gibbs-Thomson Effect on Growth-Behavior of Agbr Crystals. *Photographic Science and Engineering* **1977,** *21*, 248-252.

35. Huang, F.; Zhang, H. Z.; Banfield, J. F., Two-Stage Crystal-Growth Kinetics Observed During Hydrothermal Coarsening of Nanocrystalline Zns. *Nano Letters* **2003,** *3*, 373-378.

36. Kimijima, K.; Sugimoto, T., Growth Mechanism of Agcl Nanoparticles in a Reverse Micelle System. *Journal of Physical Chemistry B* **2004,** *108*, 3735-3738.

37. Feldmann, G.; Fabrim, Z. E.; Hennig, G. L., Ostwald Ripening of Precipitates and Self Similarity of Size Distributions in Reaction Controlled Growth. *Journal of Materials Science* **2008,** *43*, 614-620.

38. Huber, D. L., Synthesis, Properties, and Applications of Iron Nanoparticles. *Small* **2005,** *1*, 482-501.

39. Marks, B. M.; Howard, H. C., The Catalytic Decomposition of Oleic Acid. *Journal of Physical Chemistry* **1928,** *32*, 1040-1048.

40. Li, P.; Miser, D. E.; Rabiei, S.; Yadav, R. T.; Hajaligol, M. R., The Removal of Carbon Monoxide by Iron Oxide Nanoparticles. *Applied Catalysis B-Environmental* **2003,** *43*, 151-162.

41. Galuszka, J.; Sano, T.; Sawicki, J. A., Study of Carbonaceous Deposits on Fischer-Tropsch Oxide-Supported Iron Catalysts. *Journal of Catalysis* **1992,** *136*, 96-109.

42. Sun, S. H.; Murray, C. B.; Weller, D.; Folks, L.; Moser, A., Monodisperse Fept Nanoparticles and Ferromagnetic Fept Nanocrystal Superlattices. *Science* **2000,** *287*, 1989-1992.

43. Perez-Dieste, V.; Castellini, O. M.; Crain, J. N.; Eriksson, M. A.; Kirakosian, A.; Lin, J. L.; McChesney, J. L.; Himpsel, F. J.; Black, C. T.; Murray, C. B., Thermal Decomposition of Surfactant Coatings on Co and Ni Nanocrystals. *Applied Physics Letters* **2003,** *83*, 5053-5055.

44. Roonasi, P. Adsorption and Surface Reaction Properties of Synthesized Magnetite Nano-Particles. Lulea University of Technology, Lulea, 2007.

45. Berry, C. R., New Model for Double-Jet Precipitations. *Photographic Science and Engineering* **1976,** *20*, 1-4.

46. Cimino, A.; Deangelis, B. A.; Minelli, G.; Persini, T.; Scarpino, P., Investigation of the Surface-Composition of Nio-Mgo Solid-Solutions by X-Ray Photoelectron-Spectroscopy. *Journal of Solid State Chemistry* **1980,** *33*, 403-411.

47. Zhang, L.; He, R.; Gu, H. C., Synthesis and Kinetic Shape and Size Evolution of Magnetite Nanoparticles. *Materials Research Bulletin* **2006,** *41*, 260-267.

48. Kwon, S. G.; Piao, Y.; Park, J.; Angappane, S.; Jo, Y.; Hwang, N. M.; Park, J. G.; Hyeon, T., Kinetics of Monodisperse Iron Oxide Nanocrystal Formation By "Heating-Up" Process. *Journal of the American Chemical Society* **2007,** *129*, 12571-12584.

49. Ferrari, A. C., Raman Spectroscopy of Graphene and Graphite: Disorder, Electron-Phonon Coupling, Doping and Nonadiabatic Effects. *Solid State Communications* **2007,** *143*, 47-57.

50. Kudin, K. N.; Ozbas, B.; Schniepp, H. C.; Prud'homme, R. K.; Aksay, I. A.; Car, R., Raman Spectra of Graphite Oxide and Functionalized Graphene Sheets. *Nano Letters* **2008,** *8*, 36-41.

51. Reich, S.; Thomsen, C., Raman Spectroscopy of Graphite. *Philosophical Transactions of the Royal Society of London Series a-Mathematical Physical and Engineering Sciences* **2004,** *362*, 2271-2288.

52. RRUFF Spectral Database Magnetite R060191. http://rruff.info/magnetite/names/asc/R060191.

53. Socrates, G., *Infrared Characteristic Group Frequencies*. Wiley: New York, 1979; Vol. XI, p 153.

54. U.S.Environmental-Protection-Agency. Climate Change - Greenhouse Gas Emissions. http://www.epa.gov/climatechange/emissions/co2.html.

55. Kawasaki, E.; Sanscrainte, J.; Walsh, T. J., Kinetics of Reduction of Iron Oxide with Carbon Monoxide and Hydrogen. *Aiche Journal* **1962,** *8*, 48-52.

56. Joo, J.; Kwon, S. G.; Yu, T.; Cho, M.; Lee, J.; Yoon, J.; Hyeon, T., Large-Scale Synthesis of Tio2 Nanorods Via Nonhydrolytic Sol-Gel Ester Elimination Reaction and Their Application to Photocatalytic Inactivation of E. Coli. *Journal of Physical Chemistry B* **2005,** *109*, 15297-15302.

57. Jang, E.; Jun, S.; Chung, Y. S.; Pu, L. S., Surface Treatment to Enhance the Quantum Efficiency of Semiconductor Nanocrystals. *Journal of Physical Chemistry B* **2004,** *108*, 4597-4600.

58. Kim, S.; Lim, Y. T.; Soltesz, E. G.; De Grand, A. M.; Lee, J.; Nakayama, A.; Parker, J. A.; Mihaljevic, T.; Laurence, R. G.; Dor, D. M., *et al.*, Near-Infrared Fluorescent Type Ii Quantum Dots for Sentinel Lymph Node Mapping. *Nature Biotechnology* **2004,** *22*, 93-97.

59. Battaglia, D.; Peng, X. G., Formation of High Quality Inp and Inas Nanocrystals in a Noncoordinating Solvent. *Nano Letters* **2002,** *2*, 1027-1030.

60. Woo, K.; Hong, J. W., Surface Modification of Hydrophobic Iron Oxide Nanoparticles for Clinical Applications. *IEEE Transactions on Magnetics* **2005,** *41*, 4137-4139.

61. Shen, L. F.; Laibinis, P. E.; Hatton, T. A., Bilayer Surfactant Stabilized Magnetic Fluids: Synthesis and Interactions at Interfaces. *Langmuir* **1999,** *15*, 447-453.

62. Qin, J.; Laurent, S.; Jo, Y. S.; Roch, A.; Mikhaylova, M.; Bhujwalla, Z. M.; Muller, R. N.; Muhammed, M., A High-Performance Magnetic Resonance Imaging T-2 Contrast Agent. *Advanced Materials* **2007,** *19*, 1874-1878.

63. De Palma, R.; Peeters, S.; Van Bael, M. J.; Van den Rul, H.; Bonroy, K.; Laureyn, W.; Mullens, J.; Borghs, G.; Maes, G., Silane Ligand Exchange to Make Hydrophobic Superparamagnetic Nanoparticles Water-Dispersible. *Chemistry of Materials* **2007,** *19*, 1821-1831.

64. Bruchez, M.; Moronne, M.; Gin, P.; Weiss, S.; Alivisatos, A. P., Semiconductor Nanocrystals as Fluorescent Biological Labels. *Science* **1998,** *281*, 2013-2016.

65. Chan, W. C. W.; Nie, S. M., Quantum Dot Bioconjugates for Ultrasensitive Nonisotopic Detection. *Science* **1998,** *281*, 2016-2018.

66. Michalet, X.; Pinaud, F. F.; Bentolila, L. A.; Tsay, J. M.; Doose, S.; Li, J. J.; Sundaresan, G.; Wu, A. M.; Gambhir, S. S.; Weiss, S., Quantum Dots for Live Cells, in Vivo Imaging, and Diagnostics. *Science* **2005,** *307*, 538-544.

67. Rembaum, A., Us Patent Specification 4267234. **1983**.

68. Yu, W. W.; Chang, E.; Sayes, C. M.; Drezek, R.; Colvin, V. L., Aqueous Dispersion of Monodisperse Magnetic Iron Oxide Nanocrystals through Phase Transfer. *Nanotechnology* **2006,** *17*, 4483-4487.

69. Chen, Y.; Thakar, R.; Snee, P. T., Imparting Nanoparticle Function with Size-Controlled Amphiphilic Polymers. *Journal of the American Chemical Society* **2008,** *130*, 3744-+.

70. Veiga, V.; Ryan, D. H.; Sourty, E.; Llanes, F.; Marchessault, R. H., Formation and Characterization of Superparamagnetic Cross-Linked High Amylose Starch. *Carbohydrate Polymers* **2000,** *42*, 353-357.

71. Lattuada, M.; Hatton, T. A., Functionalization of Monodisperse Magnetic Nanoparticles. *Langmuir* **2007,** *23*, 2158-2168.

72. Wooding, A.; Kilner, M.; Lambrick, D. B., Studies of the Double Surfactant Layer Stabilization of Water-Based Magnetic Fluids. *Journal of Colloid and Interface Science* **1991,** *144*, 236-242.

73. Evident_Technologies. Cdse/Zns Evitags, Type 1 and Type 2-Mp Msds V1.1 *http://www.evidenttech.com/assets/docs/MSDS/CdSe-ZnS-T1-T2-EviTags-MSDS-v2.pdf* [Online], January 2006.

74. Aldana, J.; Wang, Y. A.; Peng, X. G., Photochemical Instability of Cdse Nanocrystals Coated by Hydrophilic Thiols. *Journal of the American Chemical Society* **2001,** *123*, 8844-8850.

75. Yu, W. W.; Chang, E.; Falkner, J. C.; Zhang, J. Y.; Al-Somali, A. M.; Sayes, C. M.; Johns, J.; Drezek, R.; Colvin, V. L., Forming Biocompatible and Nonaggregated Nanocrystals in Water Using Amphiphilic Polymers. *Journal of the American Chemical Society* **2007,** *129*, 2871-2879.

76. Choi., H. S.; Ipe., B. I.; Misra., P.; Lee., J. H.; Bawendi., M. G.; Frangioni., J. V., Tissue- and Organ-Selective Biodistribution of Nir Fluorescent Quantum Dots. *Nano. Lett.* **2009,** *9*, 2354-2359.

77. Xie., R.; Chen., K.; Chen., X.; Peng., X., Inas/Inp/Znse Core / Shell / Shell Quantum Dots as near-Infrared Emitters: Bright, Narrow-Band, Non-Cadmium Containing, and Biocompatible. *Nano. Res.* **2008,** *1*, 457-464.

78. Pisanic, T. R.; Blackwell, J. D.; Shubayev, V. I.; Finones, R. R.; Jin, S., Nanotoxicity of Iron Oxide Nanoparticle Internalization in Growing Neurons. *Biomaterials* **2007,** *28*, 2572-2581.

79. Hilger, I.; Fruhauf, S.; Linss, W.; Hiergeist, R.; Andra, W.; Hergt, R.; Kaiser, W. A., Cytotoxicity of Selected Magnetic Fluids on Human Adenocarcinoma Cells. *Journal of Magnetism and Magnetic Materials* **2003,** *261*, 7-12.

80. Lacava, Z. G. M.; Azevedo, R. B.; Martins, E. V.; Lacava, L. M.; Freitas, M. L. L.; Garcia, V. A. P.; Rebula, C. A.; Lemos, A. P. C.; Sousa, M. H.; Tourinho, F. A., *et al.*, Biological Effects of Magnetic Fluids: Toxicity Studies. *Journal of Magnetism and Magnetic Materials* **1999,** *201*, 431-434.

81. Shen, A. Q.; Gleason, B.; McKinley, G. H.; Stone, H. A., Fiber Coating with Surfactant Solutions. *Physics of Fluids* **2002,** *14*, 4055-4068.

82. Linse, S.; Cabaleiro-Lago, C.; Xue, W. F.; Lynch, I.; Lindman, S.; Thulin, E.; Radford, S. E.; Dawson, K. A., Nucleation of Protein Fibrillation by Nanoparticles. *Proc. Natl. Acad. Sci. U. S. A.* **2007,** *104*, 8691-8696.

83. Shimoiizaka, J.; Nakatsuka, K.; Fujita, T.; Kounosu, A., Sink-Float Separators Using Permanent-Magnets and Water Based Magnetic Fluid. *IEEE Transactions on Magnetics* **1980,** *16*, 368-371.

84. Khalafalla, S. E.; Reimers, G. W., Preparation of Dilution-Stable Aqueous Magnetic Fluids. *IEEE Transactions on Magnetics* **1980,** *16*, 178-183.

85. Decuyper, M.; Joniau, M., Magnetoliposomes - Formation and Structural Characterization. *European Biophysics Journal with Biophysics Letters* **1988,** *15*, 311-319.

86. Morales, M. A.; Jain, T. K.; Labhasetwar, V.; Leslie-Pelecky, D. L., Magnetic Studies of Iron Oxide Nanoparticles Coated with Oleic Acid and Pluronic (R) Block Copolymer. *Journal of Applied Physics* **2005,** *97*.

87. Young, A. J., Oleic Acid, Chemical Laboratory Information Profile. *Journal of Chemical Education* **2002,** *79*.

88. Landfester, K.; Ramirez, L. P., Encapsulated Magnetite Particles for Biomedical Application. *Journal of Physics-Condensed Matter* **2003,** *15*, S1345-S1361.

89. Murakami, K.; Chan, S. Y.; Routtenberg, A., Protein-Kinase-C Activation by Cis-Fatty Acid in the Absence of Ca-2+ and Phospholipids. *Journal of Biological Chemistry* **1986,** *261*, 5424-5429.

90. Jakubowski, H., Biochemistry Online: An Approach Based on Chemical Logic. 2008. http://employees.csbsju.edu/hjakubowski/classes/ch331/bcintro/default.html.

91. Dabbousi, B. O.; RodriguezViejo, J.; Mikulec, F. V.; Heine, J. R.; Mattoussi, H.; Ober, R.; Jensen, K. F.; Bawendi, M. G., (Cdse)Zns Core-Shell Quantum Dots: Synthesis and Characterization of a Size Series of Highly Luminescent Nanocrystallites. *Journal of Physical Chemistry B* **1997,** *101*, 9463-9475.

92. Rigaku-Corporation, Particle/Pore Size Analysis Software Instruction Manual. *Nanosolver (V 3.4)* **2006**.

93. Watanabe, J.; Ono, H.; Uematsu, I.; Abe, A., Thermotropic Polypeptides .2. Molecular Packing and Thermotropic Behavior of Poly(L-Glutamates) with Long Normal-Alkyl Side-Chains. *Macromolecules* **1985,** *18*, 2141-2148.

94. Zhang, L. W.; Yu, W. W.; Colvin, V. L.; Monteiro-Riviere, N. A., Biological Interactions of Quantum Dot Nanoparticles in Skin and in Human Epidermal Keratinocytes. *Toxicology and Applied Pharmacology* **2008,** *228*, 200-211.

95. Gao, X. H.; Cui, Y. Y.; Levenson, R. M.; Chung, L. W. K.; Nie, S. M., In Vivo Cancer Targeting and Imaging with Semiconductor Quantum Dots. *Nature Biotechnology* **2004,** *22*, 969-976.

96. Levasseur, B.; Renard, B.; Barbier, J.; Duprez, D., Catalytic Wet Air Oxidation of Oleic Acid on Ceria-Supported Platinum Catalyst. Effect of Ph. *Reaction Kinetics and Catalysis Letters* **2006,** *87*, 269-279.

97. Travert-Branger, N.; Dubois, F.; Carion, O.; Carrot, G.; Mahler, B.; Dubertret, B.; Doris, E.; Mioskowski, C., Oligomeric Peg-Phospholipids for Solubilization and Stabilization of Fluorescent Nanocrystals in Water. *Langmuir* **2008,** *24*, 3016-3019.

98. Yu, W. W.; Peng, X. G., Formation of High-Quality Cds and Other Ii-Vi Semiconductor Nanocrystals in Noncoordinating Solvents: Tunable Reactivity of Monomers. *Angewandte Chemie-International Edition* **2002,** *41*, 2368-2371.

99. Yu, W. W.; Qu, L. H.; Guo, W. Z.; Peng, X. G., Experimental Determination of the Extinction Coefficient of Cdte, Cdse, and Cds Nanocrystals. *Chemistry of Materials* **2003,** *15*, 2854-2860.

100. Hubbuch, J. J.; Matthiesen, D. B.; Hobley, T. J.; Thomas, O. R. T., High Gradient Magnetic Separation Versus Expanded Bed Adsorption: A First Principle Comparison. *Bioseparation* **2001,** *10*, 99-112.

101. Butter, K.; Bomans, P. H.; Frederik, P. M.; Vroege, G. J.; Philipse, A. P., Direct Observation of Dipolar Chains in Ferrofluids in Zero Field Using Cryogenic Electron Microscopy. *Journal of Physics-Condensed Matter* **2003,** *15*, S1451-S1470.

102. Donselaar, L. N.; Frederik, P. M.; Bomans, P.; Buining, P. A.; Humbel, B. M.; Philipse, A. P., Visualisation of Particle Association in Magnetic Fluids in Zero-Field. *Journal of Magnetism and Magnetic Materials* **1999,** *201*, 58-61.

103. Klokkenburg M., E. B. H., Comparison of Reversible and Irreversible Dipolar Assemblies in a Ferrofluid. *Journal of Magnetism and Magnetic Materials* **2006,** *306*, 85-91.

104. Dearing, J. A.; Dann, R. J. L.; Hay, K.; Lees, J. A.; Loveland, P. J.; Ogrady, K., Frequency-Dependent Susceptibility Measurements of Environmental Materials. *Geophysical Journal International* **1996,** *124*, 228-240.

105. Worm, H. U., On the Superparamagnetic-Stable Single Domain Transition for Magnetite, and Frequency Dependence of Susceptibility. *Geophysical Journal International* **1998,** *133*, 201-206.

106. Cognet, L.; Lounis, B., Ultra-Sensitive Detection of Individual Gold Nanoparticles: Spectroscopy and Applications to Biology. *Gold Bulletin* **2008,** *41*, 139-146.

107. Murase, K.; Fujiwara, T.; Umemura, Y.; Suzuki, K.; Iino, R.; Yamashita, H.; Saito, M.; Murakoshi, H.; Ritchie, K.; Kusumi, A., Ultrafine Membrane Compartments for Molecular Diffusion as Revealed by Single Molecule Techniques. *Biophysical Journal* **2004,** *86*, 4075-4093.

108. Strano, M. S.; Jin, H., Where Is It Heading? Single-Particle Tracking of Single-Walled Carbon Nanotubes. *Acs Nano* **2008,** *2*, 1749-1752.

109. Xu, C. S.; Cang, H.; Montiel, D.; Yang, H., Rapid and Quantitative Sizing of Nanoparticles Using Three-Dimensional Single-Particle Tracking. *Journal of Physical Chemistry C* **2007,** *111*, 32-35.

110. Lasne, D.; Blab, G. A.; Berciaud, S.; Heine, M.; Groc, L.; Choquet, D.; Cognet, L.; Lounis, B., Single Nanoparticle Photothermal Tracking (Snapt) of 5-Nm Gold Beads in Live Cells. *Biophysical Journal* **2006,** *91*, 4598-4604.

111. Rife, J. C.; Long, J. P.; Wilkinson, J.; Whitman, L. J., Particle Tracking Single Protein-Functionalized Quantum Dot Diffusion and Binding at Silica Surfaces. *Langmuir* **2009,** *25*, 3509-3518.

112. Wikipedia, Magnetite. http://en.wikipedia.org/wiki/Magnetite.

113. Jiles, D., *Introduction to Magnetism and Magnetic Materials*. Chapman & Hall 1991.

114. LesliePelecky, D. L.; Rieke, R. D., Magnetic Properties of Nanostructured Materials. *Chemistry of Materials* **1996,** *8*, 1770-1783.

115. Brosseau, C.; Ben Youssef, J.; Talbot, P.; Konn, A. M., Electromagnetic and Magnetic Properties of Multicomponent Metal Oxides Heterostructures: Nanometer Versus Micrometer-Sized Particles. *Journal of Applied Physics* **2003,** *93*, 9243-9256.

116. Pankhurst, Q. A.; Connolly, J.; Jones, S. K.; Dobson, J., Applications of Magnetic Nanoparticles in Biomedicine. *Journal of Physics D-Applied Physics* **2003,** *36*, R167-R181.

117. Goya, G. F.; Berquo, T. S.; Fonseca, F. C.; Morales, M. P., Static and Dynamic Magnetic Properties of Spherical Magnetite Nanoparticles. *Journal of Applied Physics* **2003,** *94*, 3520-3528.

118. Dunlop, D. J., Thermoremanent Magnetization in Submicroscopic Magnetite. *Journal of Geophysical Research* **1973,** *78*, 7602-7613.

119. Prakash, A. Uncovering the Mechanism for Low Field Magnetic Separations of Fe_3o_4 Nanocrystals. Thesis Proposal, Rice, Houston, 2007.

120. Berglund, A. J.; McHale, K.; Mabuchi, H., Fluctuations in Closed-Loop Fluorescent Particle Tracking. *Optics Express* **2007,** *15*, 7752-7773.

121. Qian, H.; Sheetz, M. P.; Elson, E. L., Single Particle Tracking Analysis of Diffusion and Flow in Two-Dimensional Systems. *Biophysical Journal* **1991,** *60*, 910-921.

122. Vrljic, M.; Nishimura, S. Y.; Moerner, W. E., Single-Molecule Tracking. *Methods Mol Biol* **2007,** *398*, 193-219.

123. Gaskill, L., Pkh Linker Kits for Fluorescent Cell Labeling. *Sigma-Aldrich*.

APPENDIX A

On the Brownian Motion – In collaboration with Dr.Michail Stamatakis

In this appendix, we will first derive the Fokker Plank equation for Brownian motion from the Master equation for the continuous time symmetric random walk. We will simulate 2D Brownian motion sample paths by solving the corresponding Langevin equation using a Forward Euler scheme. Further, we will use the output of the simulations to estimate the diffusion coefficient D used in the simulations. We will show that the estimator used is unbiased and converges in the mean square sense to the "true" diffusion coefficient used in the simulations. We will compare sampling schemes and show how the relative error in estimating D is affected by the sampling scheme. Finally, we will investigate the effect of "pixelization", namely what happens when the position data are integer multiples of a "pixel size".

PART I: DERIVATION OF THE FOKKER-PLANK EQUATION FROM THE MASTER EQUATION

The one-dimensional Brownian motion process is a limiting case of a continuous time discrete symmetric random walk. Suppose that a particle, initially found at x = 0, can jump Δx units to the right or to the left with equal probability. The times of the jumps follow exponential distributions (no-memory process). Thus, the Master equation for the probability of finding the particle at position $k \cdot \Delta x$ is:

$$\dot{p}_k(\tau) = \frac{\Gamma}{2} \cdot \left(p_{k+1}(\tau) + p_{k-1}(\tau) \right) - \Gamma \cdot p_k(\tau) \qquad (1)$$

This Master equation is of diffusion type and thus we can use a system size expansion technique by introducing the Anszatz (N. G. Van Kampen, "Stochastic Processes in Physics and Chemistry", NH PL 2004, Chapter XI):

$$\kappa = \frac{x}{\Delta x} \tag{2)}$$

and requiring that:

$$p_k(\tau) = \Pi(\kappa,\tau) = P(x,\tau) \quad \forall \kappa = k \tag{3)}$$

From a mathematical point of view, note that k is integer, but κ and x real numbers. Thus, equation 3) expresses the necessity for p, Π and P to agree on the points κ = k. Therefore:

$$\frac{\partial \Pi(\kappa,\tau)}{\partial \kappa} = \frac{1}{\Delta x}\cdot\frac{\partial P(x,\tau)}{\partial x} = \frac{1}{\Delta x}\cdot\left(\frac{p_{k+1}(\tau)-p_k(\tau)}{\Delta x}+\mathcal{O}(\Delta x)\right) \tag{4}$$

and:

$$\frac{\partial \Pi(\kappa,\tau)}{\partial \tau} = \frac{\partial P(x,\tau)}{\partial \tau} = \dot{p}_k(\tau) \tag{5}$$

Furthermore, we want to relate p_{k+1} and p_{k-1} to P:

$$\begin{aligned} p_{k+1}(\tau) &= \Pi(\kappa+1,\tau) = P(x+\Delta x,\tau) \\ p_{k-1}(\tau) &= \Pi(\kappa-1,\tau) = P(x-\Delta x,\tau) \end{aligned} \tag{6}$$

Thus, the Master equation becomes:

$$\frac{\partial P(x,\tau)}{\partial \tau} = \frac{\Gamma}{2}\cdot\left(P(x+\Delta x,\tau) - 2\cdot P(x,\tau) + P(x-\Delta x,\tau)\right) \tag{7}$$

We now rescale time:

$$\Delta x^2 \cdot \tau = t \tag{8}$$

and therefore:

$$\frac{\partial P(x,t)}{\partial t} = \frac{\Gamma}{2} \cdot \frac{P(x+\Delta x,t) - 2 \cdot P(x,t) + P(x-\Delta x,t)}{\Delta x^2} \tag{9}$$

Now in the limit $\Delta x \rightarrow 0$ we get the well known Fokker Plank equation for the 1-D Brownian motion process (Wiener process):

$$\frac{\partial P(x,t)}{\partial t} = \frac{\Gamma}{2} \cdot \frac{\partial^2 P(x,t)}{\partial^2 x} \tag{10}$$

Panels a, b, c of Figure show a comparison between sample paths obtained from

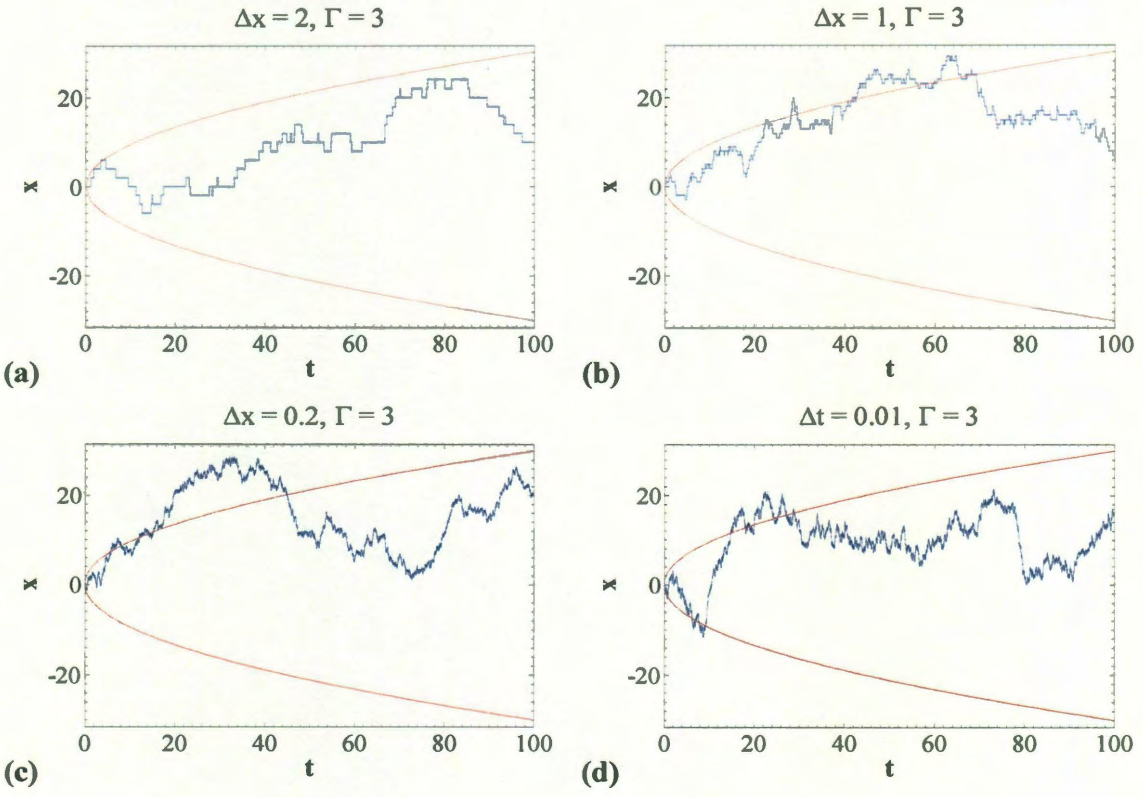

Figure A1: Panels (a-c): Comparison between sample paths obtained from simulating the random walk of equation 1) as Δx decreases. The red curves are the functions $\pm \Gamma \cdot \mathrm{sqrt}(t)$. Panel (d) shows a path obtained from simulating Brownian motion with the Langevin formulation.

simulating the continuous time discrete space symmetric random walk (equation 1)) as Δx decreases. Every random jump event is simulated in two steps: first we draw a random number following the exponentially distribution:

$$\tau_i \overset{\text{i.i.d.}}{\sim} exp\left(\frac{\Gamma}{\Delta x^2}\right) \tag{11}$$

This number corresponds to the time interval between the previous jump event and the jump event to be simulated. The next step determines whether the jump will occur to the right ($+\Delta x$) or the left ($-\Delta x$) direction. The probability for a left jump is equal to that of a right jump and thus we draw a uniformly distributed random number and if this number is less than ½ the jump will be towards the right direction otherwise towards the left.

Panel (d) shows a path obtained from simulating Brownian motion with the Langevin formulation (see next part).

PART II: FOKKER-PLANK AND LANGEVIN EQUATIONS OF BROWNIAN MOTION

We showed in Part I that the Fokker Plank equation for the 1-D Brownian motion process is:

$$\frac{\partial P(x,t)}{\partial t} = \frac{\Gamma}{2} \cdot \frac{\partial^2 P(x,t)}{\partial^2 x} \tag{10))}$$

where P(x, t) is the probability density function of finding a particle at position x at time t. Equation (10)) is subject to the initial condition:

$$P(x,0) = \delta(x) \tag{12}$$

Thus, if we consider an ensemble of Brownian particles initially concentrated at x = 0, the particle's positions in time are essentially sample paths of a Markovian process. Equation (10)) subject to (12)) has the following solution:

$$P(x,t) = \frac{1}{\sqrt{4\cdot\pi\cdot D}}\cdot\exp\left(-\frac{x^2}{4\cdot D\cdot t}\right) \tag{13}$$

where D is the diffusion coefficient, which is related to Γ as:

$$D = \frac{\Gamma}{2} \tag{14}$$

According to the following relation derived by Einstein, the phenomenological diffusion coefficient can be calculated by averaging the square displacement of the particle during a given time interval:

$$D = \frac{\langle \Delta x^2 \rangle_x}{2\cdot\Delta t} \tag{15}$$

Equation (10)) is equivalent to the Langevin equation (N. G. Van Kampen, Chapter IX.3):

$$\dot{x} = \Xi(t) \tag{16}$$

where $\Xi(t)$ is Gaussian white noise specified by:

$$\langle \Xi(t)\cdot\Xi(t') \rangle = \Gamma\cdot\delta(t-t') \tag{17}$$

The Langevin equation (16)) can be solved by using a modified forward Euler scheme (Peter E. Kloeden, Eckhard Platen, Henri Schurz, "Numerical Solution of SDE Through Computer Experiments", Springer 1997). The discretized time domain is represented as:

$$t_i = i \cdot \Delta t \qquad \forall i \in \mathbb{N}_0^+ \tag{18}$$

and the position of the particle is calculated as:

$$\begin{aligned} x_0 &= 0 \\ x_{i+1} &= x_i + \xi_i \cdot \sqrt{2 \cdot D \cdot \Delta t} \qquad \forall i \in \mathbb{N}_0^+ \end{aligned} \tag{19}$$

where we have substituted Γ according to equation (14)) and ξ_i are independent identically distributed Gaussian variables with zero mean and standard deviation equal to unity:

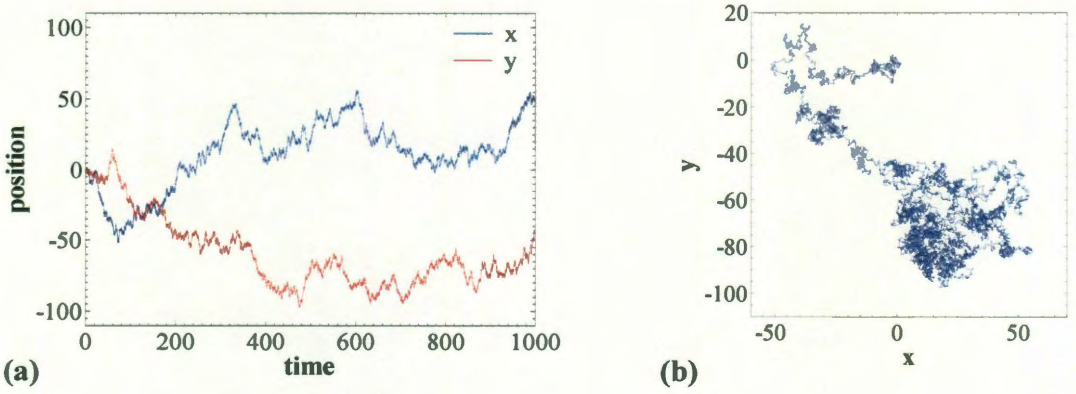

Figure A1: Panel (a): Two independent Brownian paths are simulated as the x and y coordinates of a particle diffusing in the plane. Panel (b): 2D trajectory of the particle simulated in panel (a). D = 2, Δt = 0.1.

$$\xi_i \overset{\text{i.i.d.}}{\sim} \mathcal{N}(0,1) \tag{20}$$

Thus, one can simulate one-dimensional Brownian motions by applying equations (19)) given the diffusion coefficient, the Δt and a Gaussian pseudo-random number generator. Multi-dimensional Brownian motions for an isotropic medium can also be simulated by noting that the motion for each direction is independent of the motion for the other directions. Thus, for a 2D Brownian motion one can use equations (19)) to simulate two different sample paths that will constitute the x and y positions of the particle. Note, however, that for an N-dimensional Brownian motion process the diffusion coefficient Einstein's relation will be:

$$D = \frac{1}{2 \cdot N \cdot \Delta t} \cdot \left\langle \sum_{i=1}^{n} \Delta x_i^{\,2} \right\rangle_{x_1,\ldots,x_N} \tag{21}$$

PART II: ESTIMATING THE DIFFUSION COEFFICIENT FROM 2D POSITION DATA

Figure A1 shows typical Brownian paths and the corresponding 2D path simulated by applying equation 19). Using Einstein's relation (21)) for the case of 2D diffusion, the obvious estimator to be used for the calculation of the diffusion coefficient is:

$$\hat{D}_n = \frac{1}{4 \cdot \Delta t} \cdot \left(\frac{1}{n} \cdot \sum_{i=1}^{n} \Delta x_i^{\,2} + \frac{1}{n} \cdot \sum_{i=1}^{n} \Delta y_i^{\,2} \right) \tag{22}$$

where n is the number of samples (how many measurements of the displacement during time Δt we have). Suppose now that we use data generated from simulating a 2D Brownian motion (by using equations 19)) and try to back-calculate the diffusion

coefficient. It is easy to show that estimator (22)) is an unbiased estimator in the sense that its expectation is the value of the true diffusion coefficient which we seek:

$$\begin{aligned}\mathbf{E}\left[\hat{D}_n\right] &= \frac{1}{4\cdot\Delta t}\cdot\left(\frac{1}{n}\cdot\sum_{i=1}^{n}\mathbf{E}\left[\Delta x_i^{\,2}\right]+\frac{1}{n}\cdot\sum_{i=1}^{n}\mathbf{E}\left[\Delta y_i^{\,2}\right]\right) = \\ &\frac{1}{4\cdot\Delta t}\cdot\left(\frac{1}{n}\cdot n\cdot\mathbf{E}\left[\Delta x_i^{\,2}\right]+\frac{1}{n}\cdot n\cdot\mathbf{E}\left[\Delta y_i^{\,2}\right]\right) = \\ &\frac{1}{4\cdot\Delta t}\cdot\left(\mathbf{E}\left[\Delta x_i^{\,2}\right]+\mathbf{E}\left[\Delta y_i^{\,2}\right]\right)\end{aligned} \tag{23}$$

Now for this process we know that the displacements are Gaussian random variables:

$$\begin{aligned}\Delta x_i &\overset{\text{i.i.d.}}{\sim} \mathcal{N}\left(0,\sqrt{2\cdot D\cdot\Delta t}\right) \\ \Delta y_i &\overset{\text{i.i.d.}}{\sim} \mathcal{N}\left(0,\sqrt{2\cdot D\cdot\Delta t}\right)\end{aligned} \tag{24}$$

and thus:

$$\mathbf{E}\left[\Delta x_i^{\,2}\right] = \mathbf{E}\left[\left(\Delta x_i - 0\right)^2\right] = \mathbf{E}\left[\left(\Delta x_i - \mathbf{E}\left[\Delta x_i\right]\right)^2\right] = \mathbf{Var}\left[\Delta x_i\right] = 2\cdot D\cdot\Delta t \tag{25}$$

similarly: $\mathbf{E}\left[\Delta y_i^{\,2}\right] = 2\cdot D\cdot\Delta t$

Therefore:

$$\mathbf{E}\left[\hat{D}_n\right] = \frac{1}{4\cdot\Delta t}\cdot 4\cdot D\cdot\Delta t = D \tag{26}$$

Equation (26)) reveals another interesting fact, namely that the expectation of $\hat{D}_n$ is equal to the true value D *no matter how big the sampling timestep* Δt *is taken to be.*

Furthermore, a more slightly more tedious calculation can show that estimator (22)) converges to the true diffusion coefficient in the mean square sense, namely that:

$$\lim_{n\to\infty} \mathbf{E}\left[\left(\hat{D}_n - D\right)^2\right] = 0 \tag{27}$$

Indeed:

$$\begin{aligned}\mathbf{E}\left[\left(\hat{D}_n - D\right)^2\right] = \mathbf{Var}\left[\hat{D}_n\right] = \frac{1}{(4\cdot\Delta t)^2}\cdot\left(\frac{1}{n^2}\cdot\mathbf{Var}\left[\sum_{i=1}^{n}\Delta x_i^{\,2}\right] + \frac{1}{n^2}\cdot\mathbf{Var}\left[\sum_{i=1}^{n}\Delta y_i^{\,2}\right]\right) = \\ \frac{1}{(4\cdot n\cdot\Delta t)^2}\cdot\left(\mathbf{Var}\left[\sum_{i=1}^{n}\Delta x_i^{\,2}\right] + \mathbf{Var}\left[\sum_{i=1}^{n}\Delta y_i^{\,2}\right]\right)\end{aligned} \tag{28}$$

We will calculate only the term $\mathbf{Var}\left[\sum_{i=1}^{n}\Delta x_i^{\,2}\right]$ which is apparently equal to

$\mathbf{Var}\left[\sum_{i=1}^{n}\Delta y_i^{\,2}\right]$:

$$\begin{aligned}\mathbf{Var}\left[\sum_{i=1}^{n}\Delta x_i^{\,2}\right] = \mathbf{E}\left[\left(\sum_{i=1}^{n}\Delta x_i^{\,2} - \mathbf{E}\left[\sum_{i=1}^{n}\Delta x_i^{\,2}\right]\right)^2\right] = \\ \mathbf{E}\left[\left(\sum_{i=1}^{n}\left(\Delta x_i^{\,2} - \mathbf{E}\left[\Delta x_i^{\,2}\right]\right)\right)^2\right] = \\ \mathbf{E}\left[\sum_{i=1}^{n}\left(\Delta x_i^{\,2} - \mathbf{E}\left[\Delta x_i^{\,2}\right]\right)^2 + 2\cdot\sum_{i=1}^{n-1}\sum_{j=i+1}^{n}\left(\Delta x_i^{\,2} - \mathbf{E}\left[\Delta x_i^{\,2}\right]\right)\cdot\left(\Delta x_j^{\,2} - \mathbf{E}\left[\Delta x_j^{\,2}\right]\right)\right] = \\ n\cdot\mathbf{Var}\left[\Delta x_i^{\,2}\right] + 2\cdot\frac{n^2-n}{2}\cdot\mathbf{Cov}\left[\Delta x_i^{\,2}, \Delta x_j^{\,2}\right]\end{aligned} \tag{29}$$

Now, if our samples are completely uncorrelated, the covariance term is zero and we are left with:

$$\mathbf{Var}\left[\Delta x_i^{\,2}\right] = \mathbf{E}\left[\left(\Delta x_i^{\,2} - \mathbf{Var}\left[\Delta x_i\right]\right)^2\right] = \mathbf{E}\left[\Delta x_i^{\,4}\right] - \left(\mathbf{Var}\left[\Delta x_i\right]\right)^2 \tag{30}$$

For a random variable ζ following the Gaussian distribution $\zeta \sim \mathcal{N}(\mu, \sigma)$ it follows that:

$$\mathbf{E}\left[\zeta^4\right] = \mu^4 + 6\cdot\mu^2\cdot\sigma^2 + 3\cdot\sigma^4 \tag{31}$$

and thus in our case (recall equation 24)):

$$\mathbf{Var}\left[\Delta x_i^{\,2}\right] = 3\cdot(2\cdot D\cdot\Delta t)^2 - (2\cdot D\cdot\Delta t)^2 = 2\cdot(2\cdot D\cdot\Delta t)^2 \tag{32}$$

Thus, substitution of the terms $\mathbf{Var}\left[\sum_{i=1}^{n}\Delta x_i^{\,2}\right]$ and $\mathbf{Var}\left[\sum_{i=1}^{n}\Delta y_i^{\,2}\right]$ in equation 28) yields:

$$\mathbf{E}\left[\left(\hat{D}_n - D\right)^2\right] = \frac{1}{(4\cdot n\cdot\Delta t)^2}\cdot\left(4\cdot n\cdot(2\cdot D\cdot\Delta t)^2\right) = \frac{D^2}{n} \tag{33}$$

Apparently, the requirement for convergence (equation 27)) is satisfied and thus we have shown that estimator (22)) converges to the true D value in the mean square sense.

Moreover, equation (33)) reveals that the relative error, as quantified by the coefficient of variation depends *only on the sample size* and *not on the timestep* Δt *or the true value of* D:

$$\text{Error} = \frac{\mathbf{Var}\left[\hat{D}_n\right]}{\mathbf{E}\left[\hat{D}_n\right]} = \frac{1}{\sqrt{n}} \tag{34}$$

Equation (34)) provides information about the "rate of convergence" of our estimator

and as it is typical for such cases the relative error drops with the inverse square root of the sample size. Now let us take a look back at equation (29)) in order to see what can affect this rate of convergence. We argued that when the samples are uncorrelated then $\mathbf{Cov}\left[\Delta x_i^2, \Delta x_j^2\right]$ is zero. However, if all samples are correlated then this term never becomes zero and thus the estimator fails to converge to the real value (of course in this case the displacements are not i.i.d. and expressions 24) do not hold true).

There is also the less extreme case where some of the samples are correlated. We will show this with an example: suppose that one has data for the x and y positions of the particle in discrete time:

$$\begin{aligned} t_k &= k \cdot \Delta t \qquad \forall k = 0,...n \\ \text{data: } &\left(x_k, y_k\right) \end{aligned} \tag{35}$$

Now, one forms the displacement data as follows:

$$\begin{aligned} \Delta x_i &= x_i - x_{i+10} \qquad \forall i = 0,...n-10 \\ \Delta y_i &= y_i - y_{i+10} \qquad \forall i = 0,...n-10 \end{aligned} \tag{36}$$

Apparently, in this case there exist correlations between some of the samples. For example:

$$\Delta x_0 = x_0 - x_{10} = \underbrace{\left(x_0 - x_1\right)}_{\sim \mathcal{N}\left(0, \sqrt{2 \cdot D \cdot \Delta t}\right)} + \underbrace{x_1 - x_{11}}_{= \Delta x_1} + \underbrace{\left(x_{11} - x_{10}\right)}_{\sim \mathcal{N}\left(0, \sqrt{2 \cdot D \cdot \Delta t}\right)} \tag{37}$$

thus there is a correlation of the values of Δx_0 and Δx_1 essentially because that they share a "common part" in the history of displacements of the particle. But, the values

Δx_0 and Δx_{10} do not share such a common part and thus they are not correlated. Thus, a better choice in forming the displacement data would be:

$$\begin{aligned} \Delta x_i &= x_{10\cdot i} - x_{10\cdot(i+1)} \qquad \forall i = 0,\ldots,\text{floor}\left(\frac{n}{10}\right)-1 \\ \Delta y_i &= y_{10\cdot i} - y_{10\cdot(i+1)} \qquad \forall i = 0,\ldots,\text{floor}\left(\frac{n}{10}\right)-1 \end{aligned} \tag{38}$$

PART III: ESTIMATING D FROM SIMULATIONS OF EXACT BROWNIAN PATHS

Let us now use the results of the previous sections to simulate Brownian paths (equation 19)), estimate the diffusion coefficient and check if the convergence patterns follow the theoretically predicted rate (equation 34)). In this section we will consider "exact" Brownian paths in the sense that the position of the particle is specified with infinite precision. In reality this is not the case, for example if a digital camera is used and the particle is smaller than one pixel, the position of the particle will be a multiple of the pixel size.

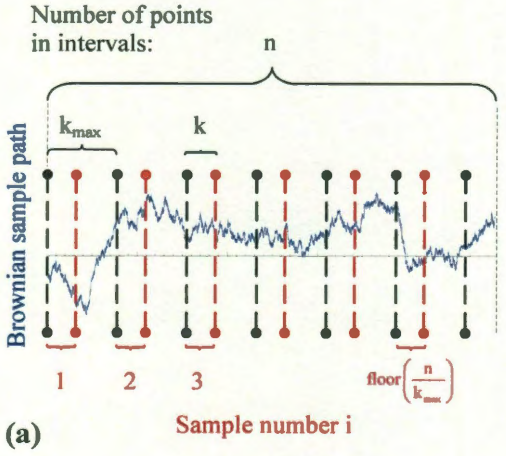

(a)

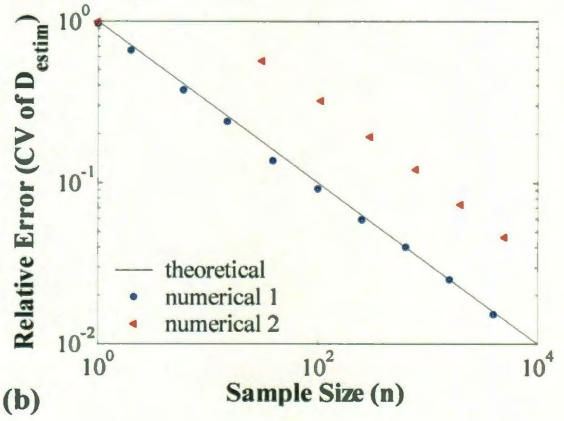

(b)

Figure A2: Panel (a): Schematic showing the sampling scheme that corresponds to the estimator in equation 39). Samples of the position of the particle are taken every Δt time units. Panel (b): Comparison of the theoretical convergence rate and the numerical ones. For the latter, the relative error $\mathbf{Var}\left[\hat{D}_n\right]/D$ was estimated from 1000 Brownian paths for various sample sizes n. D = 2, Δt = 0.1, k = 17, k_{max} = 20. For the blue dots the estimator of equation 39) was used and for the red triangles the estimator of equation 40) was used.

The first estimator we will use for estimating D from time – position data is as follows:

$$\hat{D}_n = \frac{1}{4 \cdot \text{floor}\left(\frac{n}{k_{max}}\right) \cdot k \cdot \Delta t} \cdot \sum_{i=1}^{\text{floor}\left(\frac{n}{k_{max}}\right)} \left[\left(x_{(i-1)\cdot k_{max}+k} - x_{(i-1)\cdot k_{max}} \right)^2 + \left(y_{(i-1)\cdot k_{max}+k} - y_{(i-1)\cdot k_{max}} \right)^2 \right] \quad (39)$$

where floor(z) returns the highest integer less than or equal to z and k_{max} and k are explained in Figure A2a. Application of this estimator implies a sampling scheme where the samples Δx and Δy are completely uncorrelated. Thus, the convergence rate is exactly as indicated by equation 34). This can be demonstrated by simulating many Brownian paths and estimating the relative error $\mathbf{Var}\left[\hat{D}_n\right]/D$ for different sample sizes n. A plot of $\mathbf{Var}\left[\hat{D}_n\right]/D$ versus n (Figure A2b, blue dots) indeed shows the agreement between the theoretical and the numerical convergence rates.

On the contrary a scheme that gives rise to correlations between samples will produce estimates with relative error larger than the theoretically predicted one. The following estimator demonstrates this effect:

$$\hat{D}_n = \frac{1}{4 \cdot (n - k_{max} + 1) \cdot k \cdot \Delta t} \cdot \sum_{i=1}^{n-k_{max}+1} \left[\left(x_{(i-1)+k} - x_{(i-1)} \right)^2 + \left(y_{(i-1)+k} - y_{(i-1)} \right)^2 \right] \quad (40)$$

For this estimator correlations exist between a finite number of samples of Δx and Δy, as discussed in the previous section. Thus convergence is hindered as shown by the plot with the red triangles (Figure A2b). Notice, though, that asymptotically the relative error still drops with the inverse square root of the sample size. However, the multiplier C in the relation $C/\sqrt{n}$ is greater than 1.

PART IV: EFFECT OF PIXELIZATION IN ESTIMATING THE DIFFUSION COEFFICIENT

In the previous section we were considered with the ideal case of Brownian paths that are specified with infinite precision; thus, the position of the particle is known exactly at the discrete timepoints. Here we will investigate a non-ideal case that pertains to the situation where a particle is photographed by a camera, and the time – position data are used to estimate the diffusion coefficient. We will assume that the particle is smaller than a pixel and thus only one pixel is "lit" at any time point. Therefore, the position of the particle will be an integer multiple of the pixel size.

We will refer to the pixelization mapping as the mapping of the real line to a set of discrete equidistant points. Physically this means that every point in say the x coordinate will be mapped to the center of some pixel. Thus, the pixelization mapping can be written as:

$$\mathrm{px}(z) = L_{px} \cdot \mathrm{floor}\left(\frac{z}{L_{px}} + \frac{1}{2}\right) \tag{41}$$

where L_{px} is the pixel size. A plot of the px(·) function is shown in Figure A3a. Notice that the points of the real line that correspond to the centers of the pixels are mapped to themselves. In panel (b) of the same figure, a "pixelized" 2D Brownian trajectory is shown.

We are interested in investigating how the pixelization will affect the estimation of the diffusion coefficient. Thus, let us consider a hypothetical particle that diffuses in 1D. Suppose that we monitor the particle and take independent samples of Δx using a very small Δt. If no pixelization effect exists, then the Δx values will be to the order of $\sqrt{D \cdot \Delta t}$ and we will estimate the correct diffusion coefficient. However, if pixelization is there, the majority of the Δx values will be zero and when the particle jumps from one pixel to another, the corresponding Δx value will be equal to the pixel size L_{px}. Numerical experiments indicate that these large Δx samples result in overestimations of the diffusion coefficient as shown in panel (c). It needs to be investigated analytically why this biasing is not balanced by the majority of zero Δx samples.

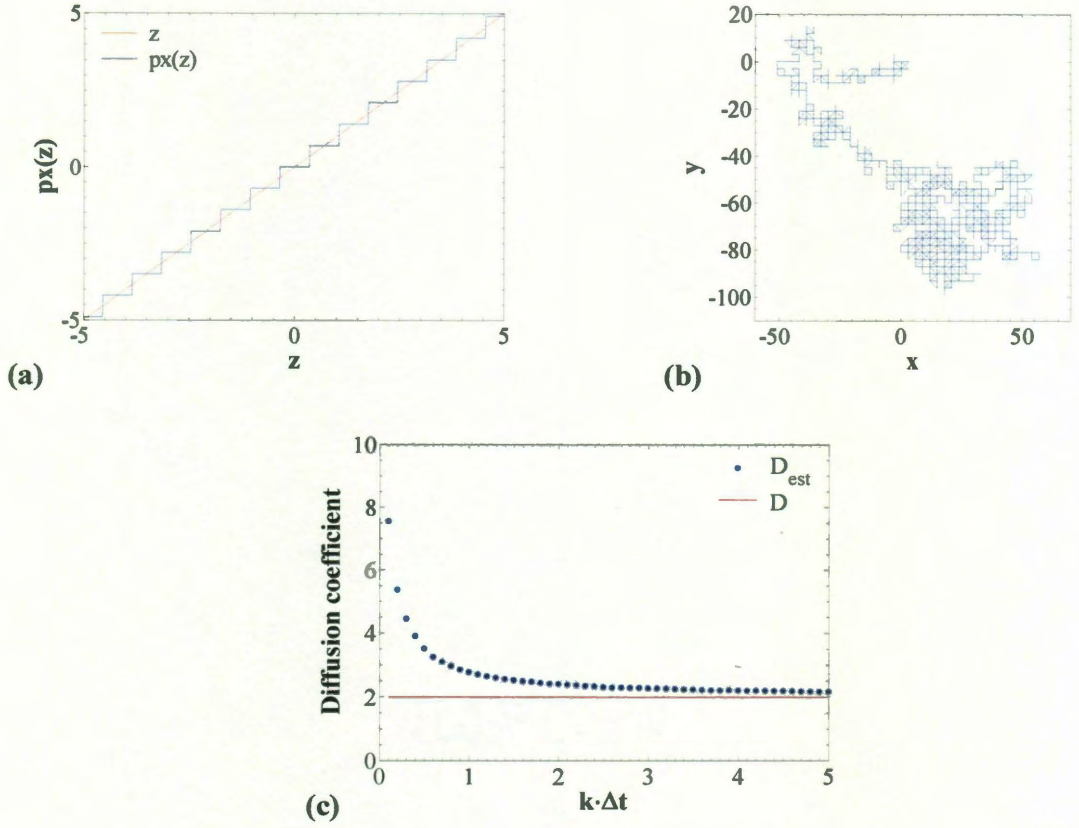

Figure A3: Panel (a): Graph of the pixelization function (equation 41)). Panel (b): The trajectory of Figure A1b after the pixelization function has been applied to both the x and y coordinate data of the particle. Panel (c): Estimated diffusion coefficient for the case of pixelization, as a function of the time interval used for sampling ($k \cdot \Delta t$). Significantly biased estimates are produced for small $k \cdot \Delta t$.

APPENDIX B – In collaboration with Dr.Michail Stamatakis

Biasing Effect of Gaussian Errors on the Estimation of the Diffusion Coefficient

We assume that the error in measuring the x-position of a diffusing particle follows Gaussian distribution with zero mean and standard deviation $\sigma_{\varepsilon,x}$ and similarly for the y-position the standard deviation will be $\sigma_{\varepsilon,y}$. Thus, the measured x and y will be equal to the actual x_{act} and y_{act} plus the corresponding normally distributed errors:

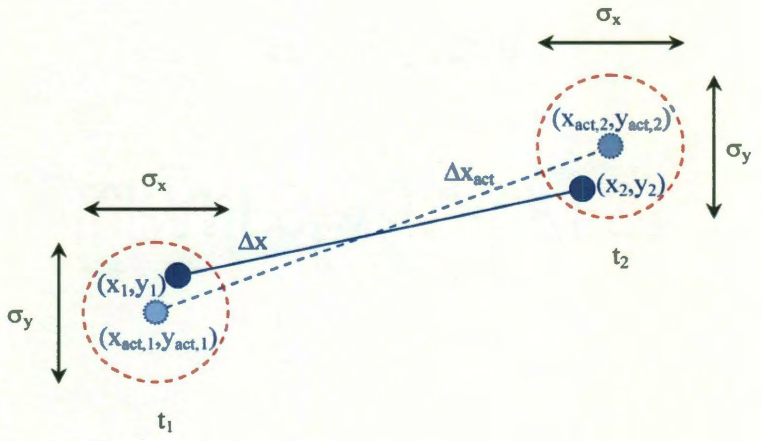

Figure B4: Errors in measuring the position of a particle

$$\begin{aligned} x &= x_{act} + \varepsilon_x \\ y &= y_{act} + \varepsilon_y \end{aligned} \tag{1}$$

$$\begin{aligned} \varepsilon_x &\sim \mathcal{N}\left(0, \sigma_{\varepsilon,x}\right) \\ \varepsilon_y &\sim \mathcal{N}\left(0, \sigma_{\varepsilon,y}\right) \end{aligned} \tag{2}$$

Now since in the estimation of the diffusion coefficient we are calculating the increments Δx and Δy, we are interested in finding their distributions. Thus:

$$\Delta x = \left(x_{act,2} + \varepsilon_{x,2}\right) - \left(x_{act,1} + \varepsilon_{x,1}\right) = \Delta x_{act} + \varepsilon_{\Delta x}$$
$$\Delta y = \left(y_{act,2} + \varepsilon_{y,2}\right) - \left(y_{act,1} + \varepsilon_{y,1}\right) = \Delta y_{act} + \varepsilon_{\Delta y} \quad (3)$$

Now, we make use of a theorem for Gaussian random variables to find the distribution of ($\varepsilon_{x,2}$ – $\varepsilon_{x,1}$) and ($\varepsilon_{y,2}$ – $\varepsilon_{y,1}$). The theorem says that the sum (difference) of two independent Gaussian random variables will be a Gaussian random variable with mean equal to the sum (difference) of the two means, and variance equal to the sum of the two variances. Since the variance is the square of the standard deviation:

$$\varepsilon_{\Delta x} = \left(\varepsilon_{x,2} - \varepsilon_{x,1}\right) \sim \mathcal{N}\left(0, \sqrt{2} \cdot \sigma_{\varepsilon,x}\right)$$
$$\varepsilon_{\Delta y} = \left(\varepsilon_{y,2} - \varepsilon_{y,1}\right) \sim \mathcal{N}\left(0, \sqrt{2} \cdot \sigma_{\varepsilon,y}\right) \quad (4)$$

From the theory of Brownian motion we also know that:

$$\Delta x_{act} \sim \mathcal{N}\left(0, \sqrt{2 \cdot D_x \cdot \Delta t}\right)$$
$$\Delta y_{act} \sim \mathcal{N}\left(0, \sqrt{2 \cdot D_y \cdot \Delta t}\right) \quad (5)$$

Now that we have clarified the above, let us try to calculate the bias in estimating diffusion coefficient D of the particle when these errors exist. The bias will be the difference between the expectation of the estimated D minus the true D:

$$\begin{aligned}\left\langle D_{est}\right\rangle - D_{act} &= \frac{1}{4 \cdot \Delta t} \cdot \left\langle \frac{1}{n} \cdot \sum_{i=1}^{n} \left(\Delta x_{act,i} + \varepsilon_{\Delta x,i}\right)^2 + \frac{1}{n} \cdot \sum_{i=1}^{n} \left(\Delta y_{act,i} + \varepsilon_{\Delta y,i}\right)^2 \right\rangle - D_{act} = \\ &= \frac{1}{4 \cdot \Delta t} \cdot \left\langle \frac{1}{n} \cdot \sum_{i=1}^{n} \left(2 \cdot \varepsilon_{\Delta x,i} \cdot \Delta x_{act,i} + \varepsilon_{\Delta x,i}^2\right) + \frac{1}{n} \cdot \sum_{i=1}^{n} \left(2 \cdot \varepsilon_{\Delta y,i} \cdot \Delta y_{act,i} + \varepsilon_{\Delta y,i}^2\right) \right\rangle + \\ &\cancel{\frac{1}{4 \cdot \Delta t} \cdot \left\langle \frac{1}{n} \cdot \sum_{i=1}^{n} \Delta x_{act,i}^{\,2} + \frac{1}{n} \cdot \sum_{i=1}^{n} \Delta y_{act,i}^{\,2} \right\rangle - D_{act}}\end{aligned} \quad (6)$$

where in the last step we have made use of the fact that the following expression:

$$\frac{1}{4\cdot\Delta t}\cdot\left(\frac{1}{n}\cdot\sum_{i=1}^{n}\Delta x_{act,i}{}^{2}+\frac{1}{n}\cdot\sum_{i=1}^{n}\Delta y_{act,i}{}^{2}\right) \tag{7}$$

is an unbiased estimator of the true diffusion coefficient D_{act} and therefore its expectation will be equal to D_{act}. Hence:

$$\langle D_{est}\rangle - D_{act} = \frac{1}{4\cdot\Delta t}\cdot\left\langle\frac{1}{n}\cdot\sum_{i=1}^{n}\left(2\cdot\varepsilon_{\Delta x,i}\cdot\Delta x_{act,i}+\varepsilon_{\Delta x,i}^{2}\right)+\frac{1}{n}\cdot\sum_{i=1}^{n}\left(2\cdot\varepsilon_{\Delta y,i}\cdot\Delta y_{act,i}+\varepsilon_{\Delta y,i}^{2}\right)\right\rangle \tag{8}$$

Let us work with the terms pertaining to x, the treatment of the remaining terms is the same:

$$\left\langle\sum_{i=1}^{n}\left(2\cdot\varepsilon_{\Delta x,i}\cdot\Delta x_{act,i}+\varepsilon_{\Delta x,i}^{2}\right)\right\rangle = 2\cdot\sum_{i=1}^{n}\left\langle\varepsilon_{\Delta x,i}\cdot\Delta x_{act,i}\right\rangle+\sum_{i=1}^{n}\left\langle\varepsilon_{\Delta x,i}^{2}\right\rangle \tag{9}$$

In order to treat the first term of the right hand side of the above equation, we make use of another theorem for the product of Gaussian variables. If A and B are normally distributed random variables with zero mean and variances σ_A and σ_B then the probability density of their product U = A·B will be given as:

$$p_U(u) = \frac{K_0\left(\frac{|u|}{\sigma_A\cdot\sigma_B}\right)}{\pi\cdot\sigma_A\cdot\sigma_B} \tag{10}$$

where K_0 is a modified Bessel function of the second kind; K_0 is the solution of the following differential equation:

$$t^2 \cdot \frac{d^2y}{dt^2} + t \cdot \frac{dy}{dt} - t^2 \cdot y = 0 \tag{11}$$

The probability distribution (10) has zero mean, and thus equation (9) becomes:

$$\left\langle \sum_{i=1}^{n} \left(2 \cdot \varepsilon_{\Delta x,i} \cdot \Delta x_{act,i} + \varepsilon_{\Delta x,i}^2 \right) \right\rangle = \sum_{i=1}^{n} \left\langle \varepsilon_{\Delta x,i}^2 \right\rangle \tag{12}$$

Therefore, equation (8) becomes:

$$\left\langle D_{est} \right\rangle - D_{act} = \frac{1}{4 \cdot \Delta t} \cdot \left\langle \frac{1}{n} \cdot \sum_{i=1}^{n} \left\langle \varepsilon_{\Delta x,i}^2 \right\rangle + \frac{1}{n} \cdot \sum_{i=1}^{n} \left(\varepsilon_{\Delta y,i}^2 \right) \right\rangle = \frac{1}{4 \cdot \Delta t} \cdot \left[2 \cdot \sigma_{\varepsilon,x}^2 + 2 \cdot \sigma_{\varepsilon,y}^2 \right] \tag{13}$$

and if $\sigma_{\varepsilon,x} = \sigma_{\varepsilon,y} = \sigma_{\varepsilon}$:

$$\left\langle D_{est} \right\rangle - D_{act} = \frac{\sigma_{\varepsilon}^2}{\Delta t} \tag{14}$$

We have thus found that the relative bias in estimating the Diffusion Coefficient D, is:

$$\left\{ \text{Relative Bias D} \right\} = \frac{\left\langle D_{est} \right\rangle - D_{act}}{D_{act}} = \frac{\sigma_{\varepsilon}^2}{D \cdot \Delta t} \tag{15}$$

Therefore, the bias is a monotonically decreasing function of Δt and decreases with the inverse of D.

Now, suppose that we perform an experiment where the maximum bias we can tolerate is 5%. Which are the acceptable Δt values that we can use? These Δt values will have to satisfy the following inequality:

$$\Delta t \geq \frac{\sigma_\varepsilon^2}{D \cdot 0.05} \tag{16}$$

Evidently, if we decrease the Diffusion Coefficient by making the solvent more viscous, we undesirably increase the acceptable Δt that will give us a bias no greater 5%. Effectively, in this case, the particle displacement becomes insignificant or comparable to the random errors in determining the particle's position. That is why we will then need to increase the Δt.

APPENDIX C

Program to compute the diffusion coefficient from particle trajectory (coded in Matlab)

```
clf
clear all


name=input('Excel file name:','s');
inputfile= xlsread(name);
inputfilesize= size (inputfile)
nonum=0;

      m=1;
   for j=1:1:inputfilesize(1,1)

         if isnan(inputfile(j,1))

           nonum=nonum+1;
           if nonum==1
              position(m)= j-1;
           end

         elseif nonum > 0
              position(m+1)=j;
              nonum=0;
              m=m+2;
         end

     end


positionsize=size(position)
if(position(positionsize(1,2))~=inputfilesize(1,1))
   position(positionsize(1,2)+1)= inputfilesize(1,1);
end
%removing singled out rows without any preceding and suceeding values


for i=2:1:positionsize(1,2)-2
   if(position(i)==position(i+1))
      index=position(i);
      inputfile(index,1)=nan;
      inputfile(index,2)=nan;
   end
end
inputfile;
position;
%added added added added added added
% calculating size again to avoid duplicity
inputfilesize;
inputfilesize= size (inputfile);
nonum=0;
```

```
      m=1;
   for j=1:1:inputfilesize(1,1)

         if isnan(inputfile(j,1))

           nonum=nonum+1;
           if nonum==1
              position2(m)= j-1;
           end

        elseif nonum > 0
             position2(m+1)=j;
             nonum=0;
             m=m+2;
        end

     end

position2;
position2size=size(position2);
%added added added added added

% eliminating last row if its penultimate value is a nan

if isnan(inputfile(inputfilesize(1,1)-1,1))
   inputfilesize(1,1)= position2(position2size(1,2)-1);
end

%checking for nan positions again
     m=1;
   for j=1:1:inputfilesize(1,1)

         if isnan(inputfile(j,1))

           nonum=nonum+1;
           if nonum==1
              pos(m)= j-1;
           end

        elseif nonum > 0
             pos(m+1)=j;
             nonum=0;
             m=m+2;
        end

     end



sizepos=size(pos);
pos(sizepos(1,2)+1)= inputfilesize(1,1);
sizepos=size(pos);
pos
```

```
c=1;
for j=2:2:sizepos(1,2)-1
    index=1;
    for i=c:1:c-1+pos(j+1)-pos(j)
        dif(i,1)=inputfile(pos(j)+index,1)-inputfile(pos(j)+index-1,1);
      dif(i,2)=inputfile(pos(j)+index,2)-inputfile(pos(j)+index-1,2);
      index=index+1;
   end
   c=i+1;
   j;

end
dif;
%copying rows upto first nan position
for i=1:1:pos(1,1)
final(i,1)=inputfile(i,1);
final(i,2)=inputfile(i,2);
end
%computing total number of lost rows
lostrows=0;
for i=2:2:sizepos(1,2)-1
   lostrows= lostrows+ pos(i)-pos(i-1);
end;
%adding differences to be appended to the row value before first nan
sizedif=size(dif);
for j=1:1:2
    for i=1:1:sizedif(1,1)
        sumdif(i,j)=0;
        for k=1:1:i
            sumdif(i,j)=sumdif(i,j)+dif(k,j);
        end
    end
end
%computing the final matrix that is combined
for j=1:1:2
   k=1;
   for i=pos(1,1)+1:1:inputfilesize(1,1)-lostrows
        final(i,j)=inputfile(pos(1,1),j)+sumdif(k,j);
        k=k+1;
    end
end
b=size(final);
delt = 0.033;
interval1=input('Interval Multiple:');
%picking out interval values
%interval=2;
for interval=1:1:interval1
    x=[];
for i=1:1:b(1,2)
    for j=1:1:b(1,1)
        if mod(j-1,interval)==0
        x(j,i)= final(j,i);
        end
    end
end
```

```
d = size(x);

for i=3:1:4
    for j=1:1:(d(1,1)-1)/interval
        if(i==3)
        x(j,i)= (x(interval*(j-1)+1,1) - x(j*interval+1,1))^2;
          else
        x(j,i)= (x(interval*(j-1)+1,2) - x(j*interval+1,2))^2;
          end
    end
end


e = sum(x,1);
diff_coeff = (e(1,3)+e(1,4))/(4*interval*delt)/((d(1,1)-1)/interval) *
240^2 * 10^(-18);

diameter = 2*1.38*10^(-23)*295*7/(22*6*0.995*10^-3)/diff_coeff;
f(interval)= diameter;
g(interval)=diff_coeff;
subplot (2,1,1)
plot(interval,f(interval),'b.')
hold on
subplot (2,1,2)
plot(interval, g(interval),'r.')

hold on


%c=0;
variance1 = var(f)
variance2 = var (f, 1)
Mean = mean(f)
minimum = min(f)
diffusioncoeff = g(interval)

end
```